Alma Mater Studiorum – Università di Bologna

School of Science
Department of Physics and Astronomy
Master Degree Programme in Astrophysics and Cosmology

From ground to space: high-energy atmospheric and astrophysics transient phenomena through a ground-based detector and a 8U CubeSat

Graduation Thesis

Presented by:
Ludovica Zappalà

Supervisor:
Prof. Leonardo Testi
Co-supervisor:
Dr. Enrico Virgilli
Dr. Paolo Calabretto

Academic year 2024-2025

Will someone find out what the word is that makes the world go round?

Abstract

High-energy transient phenomena, ranging from Terrestrial Gamma-Ray Flashes and gamma-ray glows in the Earth's atmosphere to cosmological events such as Gamma-Ray Bursts, are of remarkable interest due to their high-energy emission and extremely short duration. Despite their very different origins, these phenomena share key observational features: they produce impulsive gamma-ray emissions and require fast and sensitive detectors, robust trigger logic, and versatile analysis tools. This Thesis addresses these challenges through a combined ground-to-space approach. On the ground, two complementary detector systems, Gamma-Flash at Mt. Cimone (Sestola, Modena) and PIZ-Gamma at Mt. Piz Boè (Canazei, Trento), were developed, optimized, and operated to detect atmospheric gamma-ray transients in real conditions. Their characterization, calibration, and the creation of a data-analysis pipeline carried out in this work, enabled the identification of high-energy events. The strong dependence of detection efficiency on altitude, environment, and instrumental configurations is investigated in this work. Building on this experience, the Thesis also proposes a mission concept for an 8U CubeSat equipped with a wide-field 4π gamma-ray detector capable of observing both atmospheric and astrophysical transients. It shows how technologies developed for ground-based detectors can be translated into a compact orbital instrument, effectively using ground-based results to guide the design of a space-borne platform for the joint study of TGFs, GRBs, and other high-energy transient events.

Contents

List of Figures

List of Tables

Introduction

High-energy transient phenomena represent some of the most extreme and fascinating events occurring in nature. They arise in a broad range of environments, from violent thunderstorms in the atmosphere to distant cataclysms of dying stars, and require dedicated instrumentation and analysis techniques to be detected and interpreted. Despite their very different origins, atmospheric and astrophysical transients share a number of observational analogies: they are short-lived, energetic, and often unpredictable. As a consequence, their detection relies on sensitive, fast-response instruments capable of operating in challenging environments, whether that be at ground level under rapidly changing meteorological conditions or in space, where the detector must be robust, autonomous, and optimized for high-rate photon streams. This Thesis investigates high-energy transient phenomena from two complementary perspectives:

- A ground-based experimental approach, centered on the Gamma-Flash and PIZ-Gamma detectors, the former developed under the support from the Italian Space Agency and led by INAF, the latter proposed and led by Fondazione Bruno Kessler (FBK) with the goal to observe atmospheric gamma-ray events such as Terrestrial Gamma-ray Flashes (TGFs) and gamma-ray glows;
- A space-based perspective, in which a mission concept for an 8U CubeSat equipped with a 4π gamma-ray detector is proposed for the joint detection of transient events of both atmospheric and astrophysical origin, namely TGFs and Gamma-Ray Bursts (GRBs).

In Chap. 1, a detailed physical framework for the transient phenomena of interest is provided. Chap. 1 focuses on high-energy events generated in the Earth's atmosphere, primarily those associated with thunderstorm activity. TGFs and gamma-ray glows, despite being discovered only a few decades ago, have rapidly become an important field of research for both atmospheric physics and high-energy astrophysics. Their short duration, high photon energies, and strong connection to lightning processes require fast detectors with precise timing capabilities. Chap. 2 extends the context to high-energy astrophysics, introducing the fundamental physics of GRBs, their prompt and afterglow emissions, spectral and temporal properties, and their classification into short and long bursts. By presenting these two different phenomena, the Thesis highlights the conceptual and instrumental continuity linking atmospheric and cosmic high-energy

transients. Both classes of phenomena, although being associated with very different physical environments, produce impulsive gamma-ray signals whose detection requires similar techniques, enabling a unified data-analysis approach.

The central part of the Thesis, Chap. 3, is devoted to the Gamma-Flash and PIZ-Gamma ground-based experiments. These projects share the same scientific objective: detect and study high-energy transient phenomena associated with thunderstorms. The Gamma-Flash experiment, installed at Mt. Cimone (Sestola - 2165 m a.s.l.), consists of two families of detectors (type I and type II), each equipped with dedicated electronic readout boards and optimized acquisition schemes. The PIZ-Gamma experiment, located at the Piz Boè refuge (Canazei, Trento - 2873 a.s.l.) employs similar detectors but organized in a slightly different configuration. In this chapter, all the stages of experimental activity are reported: the characterization of the detectors, the various tests performed to optimize acquisition windows, thresholds, high voltage settings, decimation factors, and saturation levels; and the development of trigger algorithms capable of identifying rapid increases in the count rate.

A key part of Chap. 3 is the design and implementation of a data-analysis code, written specifically to process the raw outputs of Gamma-Flash and PIZ-Gamma. Even if it was used for gamma-ray glows detection, it can be used both for atmospheric and astrophysical transients. The code accomplishes several essential different tasks: it processes waveform-based acquisitions from Red Pitaya digitizer boards (type I detectors) as well as acquisitions from FBK readout boards (type II detectors), and extracts information such as peak amplitudes, timestamps, and environmental parameters. Finally, it constructs light curves and energy spectra with configurable binning. Thanks to its modular architecture, the code can be applied not only to TGFs and gamma-ray glows, but also to astrophysical events such as GRBs, since both phenomena require the identification of sharp temporal variations in gamma-ray fluxes. In this sense, the code constitutes a general-purpose transient-detection pipeline.

In Chap. 3, examples of transient events successfully detected by the instruments at Mt. Cimone and Piz Boè are also shown. These detections confirm that the experimental setups are fully operational and capable of capturing real atmospheric events, validating the trigger mechanisms and the data-analysis routines developed during the project. In particular, the comparison between the Gamma-Flash and PIZ-Gamma results highlights the importance of site altitude and open field of view: the PIZ-Gamma detectors, being placed at over 2800 m a.s.l. and in an unobstructed location, show a larger number of events in a shorter period, demonstrating the strong effect of atmospheric attenuation and field-of-view constraints.

Chap. 4 of the Thesis is dedicated to extending the work performed on the ground-based detectors to a space mission concept. Based on the experience gained from the Gamma-Flash and PIZ-Gamma projects, the thesis proposes the implementation of an 8U CubeSat, designed as a wide-field 4π detector for gamma-ray transients detections. The idea behind this design is to maximize the observable sky fraction and to reduce the complexity of pointing requirements, making the satellite capable of detecting events

from any direction. Such a configuration is particularly suitable for GRBs, whose detection requires a wide field of view but also for TGFs. The proposed CubeSat therefore could serve as a dual-purpose mission:

- The detection of GRBs, contributing to multi-messenger observations and providing complementary data to existing missions;
- the detection of TGFs from orbit, enabling the study of electron acceleration and discharge mechanisms inside thunderstorms.

For the instrument concept, effective area and localization capability were evaluated, starting the exploration of the main parameters of the experiment, such as the number of detectors in overall CubeSat and their size. This system was studied through simulations performed with MEGAlib (Medium-Energy Gamma-ray Astronomy Library). Moreover, some future perspectives of this work are also reported.

Finally, the conclusions are drawn, presenting the results obtained from this Thesis and outlining future prospects for this work, considering how the proposed space-based experiment offers interesting and promising potential for future research.

Chapter 1

High-energy atmospheric transient phenomena

In this chapter, different atmospheric transient phenomena are reported. In particular, mostly high-energy short-lived events, such as Terrestrial Gamma ray Flashes (TGFs) and Gamma-ray glows, are described. They may be connected to some Transient Luminous Events (TLEs) optical emissions related to thunderstorms, and because of this, this kind of phenomena are briefly presented too. Specifically, TGFs and Gamma-ray glows main characteristics and detections are reported, respectively, in Sec. 1.1 and Sec. 1.2. Ultimately, a general overview of some TLEs is outlined in Sec. 1.3.

1.1 Terrestrial Gamma Ray Flashes

In this section, TGFs are described and strictly related events are reported. In particular, the TGF phenomenon description that is actually largely accepted is presented in Subsec. 1.1.1. Afterwards, two events closely connected to TGFs are reported: Terrestrial Electron Beams (TEB) and TGF afterglows, respectively, in Subsec. 1.1.2 and Subsec. 1.1.3. Ultimately, TGF detection history is outlined with main detections and instruments in Subsec. 1.1.4.

1.1.1 Phenomenon description

TGFs are really complex phenomena, their production involves several processes, including runaway electron production mechanism, thermal runaway electron production, relativistic runaway electron avalanches, bremsstrahlung emissions, and X-ray and gamma-ray propagation. These processes and the consequent TGF production are described in this section with reference to J. R. e. a. Dwyer (2012), considering the TGF formation procedure that is actually largely accepted and that combines elements from both theory and observations.

The starting process for TGF formation is related to electrons that are accelerated through a runaway process. Indeed, these accelerated electrons are called runaway electrons. For an electron to run away, its initial kinetic energy must be above a certain threshold, which decreases rapidly with increasing electric field. Such energetic seed electron may be provided from an external source with respect to the thundercloud, such as cosmic rays. In this scenario, cosmic rays arrive in the form of extensive air showers. Sometimes they are composed of millions of energetic particles propagating down through atmosphere at once and at thunderclouds altitudes. Most of these charged particles are electrons with high energies (order of MeV). In addition to external sources of seed electrons, lightning leaders may provide the energetic seed electrons internally in the thundercloud. In particular, if in a small region the electric field exceeds the critical field E_c for which low-energy thermal electrons runs away, then runaway electrons can be accelerated out of the low-energy population, via thermal runaway mechanism. At leader tips, high enough fields can exist to produce thermal runaway. The thermal runaway process alone cannot account for the large fluxes associated with TGFs and also the average energy for this process is too low (e. g. few keV). At this point, either the seed electrons come from cosmic rays or from lightning leaders, they can undergo the following processes described, in order to obtain in the end the large fluxes and the high energies that are expected for a TGF.

In 1925, C. T. R. Wilson discovered and described the runaway electron mechanism in which fast electrons may obtain large energies from static fields present in air (Wilson 1925). In particular, when for an electron the rate of energy gain from an electric field exceeds the rate of energy loss from interactions with air molecules, hence it continues to gain energy and increases in speed. This type of runaway electrons are produced in electric fields greater than the so-called break-even field:

$$E_b = 2.18 \cdot 10^5 \ V/m \cdot n \tag{1.1}$$

which corresponds to the rate at which minimum ionizing electrons lose energy, where n is the density of air with respect to that at sea level. In 1992, Gurevich, Milikh and Roussel-Dupré showed that when Møller scattering (electron-electron elastic scattering) is included, the runaway electrons described by Wilson undergo avalanche multiplication, resulting in a large number of relativistic runaway electrons for each energetic seed electron injected into the high-field region. This avalanche mechanism is commonly referred to as the Relativistic Runaway Electron Avalanche (RREA) mechanism. In 2003, Dwyer (J. R. Dwyer 2003) estimated the runaway electron avalanche electric field threshold, whose value is:

$$E_{th} = 2.84 \cdot 10^5 \ V/m \cdot n \tag{1.2}$$

where n is the density previously defined. This electric field threshold is slightly larger than the break-even field described above. When runaway electrons travel exactly along the electric field lines, the break-even field E_b would be the threshold

for runaway electrons propagation and avalanche multiplication. Considering elastic scattering of the electrons with atomic nuclei (Coulomb scattering) and the atomic electrons (Møller scattering), deviations in the electron trajectories are caused. Therefore, about 30% larger electric field than the break-even field is required in order for the electrons to run away and avalanche multiply, so the related electric field value is E_{th} just described. This value is comparable to the maximum electric field strength measured inside thunderclouds. Therefore, these processes described can explain the connection between lightning initiation and runaway electron production, so runaway electron avalanches may be common inside thunderclouds. At this stage, runaway electrons interact with air. Although there are several mechanisms to generate high-energy radiation, the single most important mechanism is bremsstrahlung interaction of electrons with air atoms. In this way, the gamma-rays are produced with energies up to tens of MeV. This is the TGF, its duration is of the order of few tens, up to a few hundred microseconds. Moreover, it has a non-thermal spectrum characterized by a decreasing continuum, as it is due to bremsstrahlung emission. Thus, a TGF is the result of the developing lightning discharge, and the processes just described lead to its formation.

Some other general concepts related to these events are outlined in the following. There are two kinds of TGF: upward and downward TGF, when gamma-rays, electrons, or both are emitted, respectively, upward or downward with respect to the thundercloud. In the first case, they are detected by satellite in space and it is estimated that this TGFs rate is of hundreds of TGFs per day. While, in the second case, they are detected by instruments from ground and they are much rarer than the ones detected by satellite in space. Furthermore, because of the relativistic electrons produced during these events and the related radio emission, TGFs are also typically associated with Very Low Frequency (VLF), Low Frequency (LF), High Frequency (HF) and Very High Frequency (VHF) radio emissions that are associated with the production mechanism of the TGF itself. VLF or LF signals are observed in connection with TGF from ground, while for space observations HF and VHF parts of the spectrum are considered and they are used, in general, to connect the TGF with the corresponding lightning. Furthermore, TGFs are also related to optical emissions associated with lightning activity, such as some of the ones described in Sec. 1.3. In particular, TGFs occur at the onset of these optical emissions. Thus, in conclusion, the high-energy detection connected directly to the TGF itself, used together with the radio and the optical emissions can help to assess TGF location and study its production mechanism, in order to have a full picture of the phenomenon.

1.1.2 Terrestrial Electron Beams

The TEB is an event that is closely linked to TGFs. The mechanism that generates this kind of event starts with gamma-rays that compose a TGF. TGF gamma-rays propagate up through the atmosphere and interact with air atoms, predominantly

via Compton scattering and pair-production. Below a certain altitude most of these secondary particles are quickly absorbed by atmosphere. At about 40 km altitude, there is still enough atmosphere for the TGF gamma-rays to interact with air, producing secondary Compton electrons and pair-produced electron and positrons, but not so much atmosphere that these secondary particles are absorbed before they can escape to space. Thus, at these altitudes, a fraction of them can escape the atmosphere and propagate into the inner magnetosphere along the local geomagnetic field lines. This is a TEB, it can be detected in low-Earth orbit, either near the TGF location or thousand kilometers away. TEBs contain some of the most energetic particles accelerated in the near-Earth environment. These events are rare and their duration is of the order of millisecond. Their spectral distribution is similar to that of TGFs, but softer, with a large number of electrons at lower energies. Furthermore, the presence of the 511 keV annihilation line in the energy spectra confirms the presence of positrons. The TEB production mechanism, described above, was proposed in J. R. e. a. Dwyer (2008) and models were used to explain this event. Moreover, this paper shows also that gamma-ray flashes and resulting energetic electron beams similar to TEBs can also occur in Saturn's atmosphere, where thunderstorms and lightning activity are present. The first clear TEB detection was made by ASIM in 2018. Afterwards, TEBs were observed different times also by Fermi GBM, which collected a significant quantity of data throughout the years.

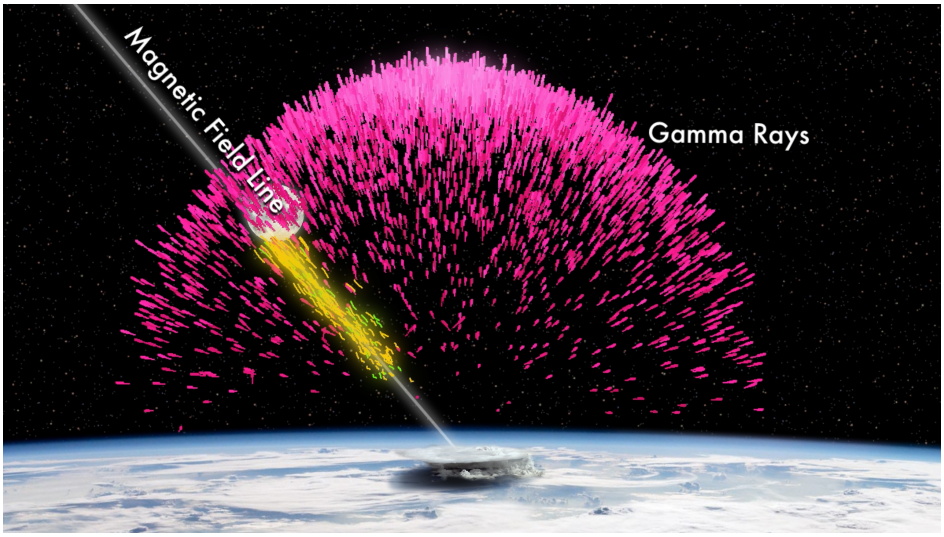

Figure 1.1: Sketch of a TEB. Gamma-rays are interacting with air, producing electrons and positrons, as described in Subsec. 1.1.2. These secondary particles propagate along Earth magnetic field lines, as represented. (Credit: NASA/Goddard Space Flight Center and J. Dwyer and Florida Institute of Technology 2011).

1.1.3 Afterglows

There may be another event that is strictly connected to TGFs, which is called TGF afterglow, as it could be caused by the capture of neutrons produced by TGF. In particular, gamma-rays related to TGF can interact with air atoms and photonuclear reactions can occur, thus producing neutrons. These neutrons slowly cool down through collisions with nuclei of air molecules. During thermalization they can be captured again by nuclei and sometimes there could be the release of a high-energy photon, which have energies of the order of tens of MeV. This event is called TGF afterglow, its duration is milliseconds to seconds long and it is caused by the thermalization time of the intermediate neutrons. In Rutjes (2017), a prediction of TGF afterglow was reported and its related characteristics were described, although this event was not well characterized yet. Afterwards, also in 2017, a TGF afterglow was detected. Specifically, as reported in Enoto (2017), two events were observed: a TGF with its typical duration shorter than a millisecond and a subsequent 40-60 millisecond-long gamma-ray glow.

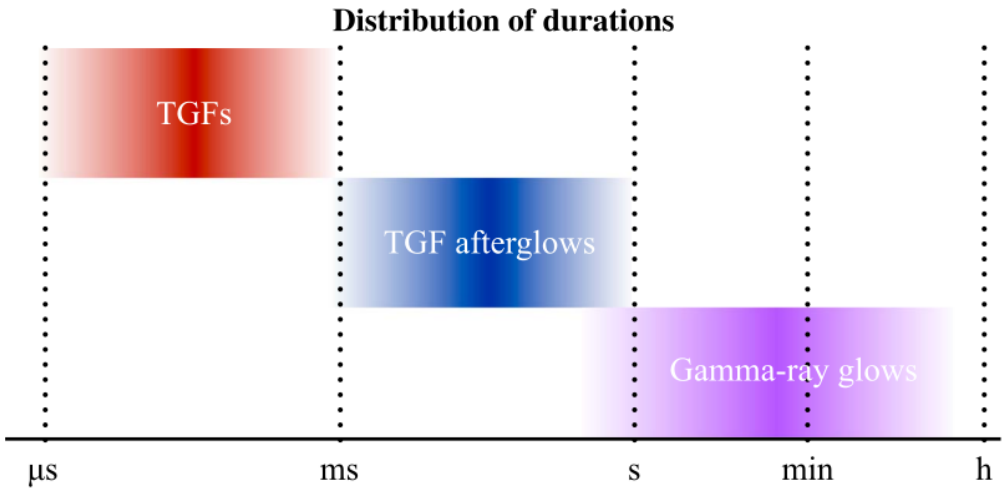

Figure 1.2: Sketch of the distribution of durations of some of the phenomena described. Specifically, TGFs, TGF afterglows, and gamma-ray glows durations. (From Rutjes 2017).

1.1.4 Detection history

TGFs were first discovered in data from the Burst and Transient Source Experiment (BATSE) aboard NASA's Compton Gamma-ray Observatory (CGRO), whose primary science target was cosmic gamma-ray bursts (GRBs). BATSE consisted of eight sets of scintillators, one set facing outward from each corner of the spacecraft,

for sensitivity to X-rays and gamma-rays from the whole sky, and it worked in a triggered mode. Since CGRO was in low-Earth orbit, the surface below was always visible to four detectors. Each of the eight identically configured detector modules contains two scintillation detectors: a Large Area Detector (LAD) with sheets of NaI, and a Spectroscopy Detector (SD) in the form of a cylinder of NaI. The literature on BATSE TGFs uses only the LAD data, but the SDs saw the TGFs as well.

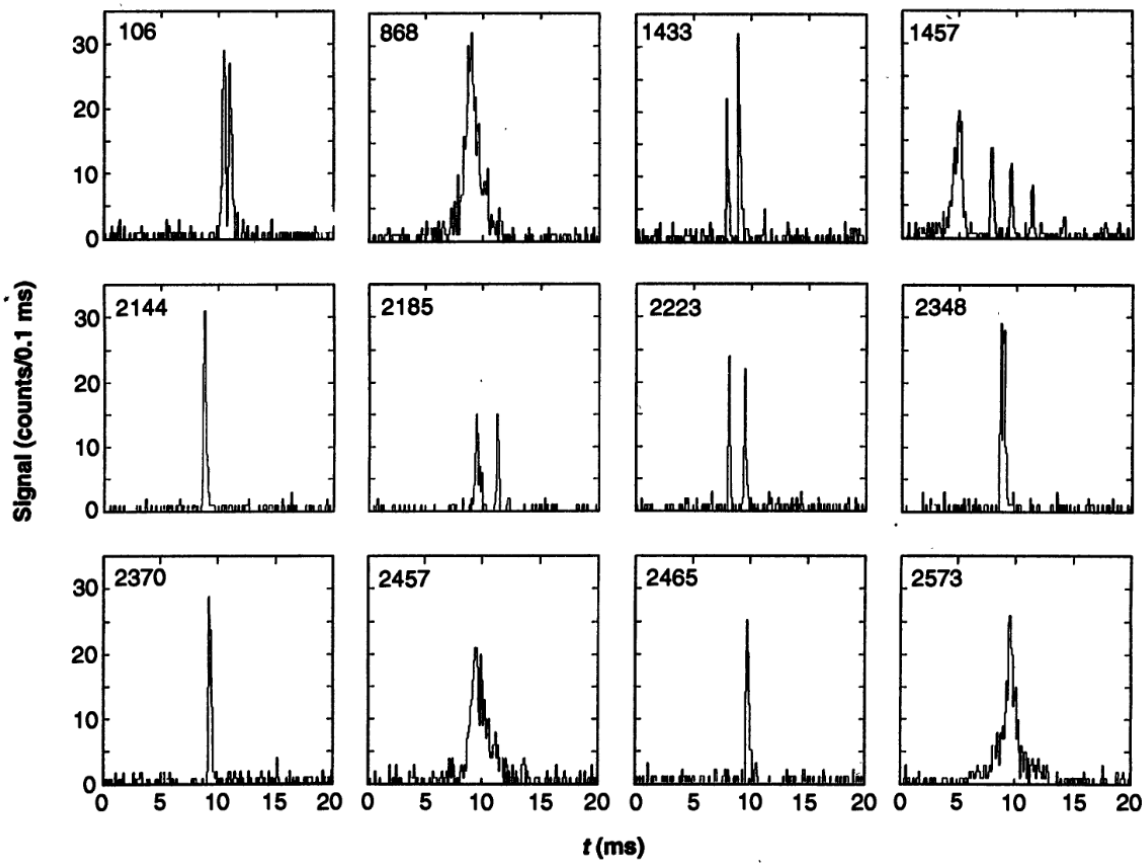

Figure 1.3: Light curves of the first TGFs detected. Specifically, 12 events detected by BATSE from 1991 to 1993, associated to TGFs, are represented. The duration of each of these events is of the order of hundreds of microseconds. (From Fishman 1994).

From TGF discovery paper (Fishman 1994) it was reported that the typical TGF duration is of the order of a millisecond, as opposed to GRB durations, which are typically a few seconds. Furthermore, it was noticed that the spectra of TGFs were much harder than those of GRBs, other cosmic sources, and solar flares. In Fishman (1994), satellite imagery was used to establish the TGF connection with thunderstorms,

and shortly afterwards in Inan (1996), was discovered that individual radio atmospheric signals, the signature of a lightning flash, were associated with TGFs.

For the first decade after their discovery, TGFs were generally assumed to originate from high-altitude runaway electron production. Later discoveries overturned this presumed association: in J. R. e. a. Dwyer (2004), a gamma-ray flash observed on the ground in Florida was reported in association with rocket-triggered lightning, and this event had an energy spectrum and duration similar to TGFs. Thus, TGFs are not only produced at high altitudes.

The second source of TGF data was the Reuven Ramaty High Energy Spectroscopic Imager (RHESSI) satellite, a NASA Small Explorer dedicated to the study of solar flares with an array of nine high-resolution germanium detectors. It was launched in 2002 and while the instrument is much smaller than BATSE, and consequently detects only a few tens of photons in each TGF, it has several advantages that make the RHESSI data complementary to BATSE. First, RHESSI returns to the ground data on every photon detected, without an onboard trigger, meaning that data can be searched with continuously refined algorithms on the ground for TGF events. This produced a detection rate for RHESSI TGFs about an order of magnitude higher than the average rate during BATSE's lifetime. Second, RHESSI produces high-energy spectra of TGFs that run from 30 keV to 17 MeV. However, RHESSI was not built with GPS synchronization for absolute timing. Millisecond uncertainties in its timing made the comparison of TGF timing with the timing of lightning throughout the mission more complicated. The large number of RHESSI TGFs allows detailed comparisons of the geographical distribution of TGFs with other meteorological phenomena. The time of occurrence, as well as the spatial distribution of TGFs, may provide important information to understand and study their cause and mechanism.

Furthermore, two more missions, each with its own unique capabilities, have collected TGF data in the past years: Fermi, a NASA spacecraft, and AGILE (Astro rivelatore Gamma a Immagini Leggero), an Italian mission. They are both gamma-ray telescopes for astrophysics in the MeV to GeV range. Fermi observes TGFs in its Gamma-ray Burst Monitor (GBM) instrument. GBM consists of 12 uncollimated NaI scintillators pointing in different directions and two large bismuth germanate (BGO) scintillators, the former primarily for photons up to 1 MeV and the latter operating up to 40 MeV. Like BATSE, GBM usually operates in a triggered mode and recently, it has been able to operate in a photon-by-photon mode similar to RHESSI's. Since its overall collecting area is much greater than RHESSI's, this represents the most sensitive data set ever taken for TGF detection. GBM provides the best spectral information available to date for each individual TGF, with the combination of large effective area, good time and energy resolution, and large energy range. Regarding AGILE, similarly to the Large Area Telescope (LAT) on Fermi, is a tracking detector that determines the direction of incoming high-energy gamma photons, and collects the remaining energy in a "mini-calorimeter" (MCAL) made of CsI crystals at the bottom. AGILE primarily detects TGFs in MCAL.

Thereafter, an airborne detector made the first detection of a TGF from an altitude comparable to its production altitude. As reported in Smith (2011), the Airborne Detector for Energetic Lightning Emissions (ADELE), flying at 14 km aboard the Gulfstream V jet, saw a TGF at the same time as a lightning flash in an active cell 10 km away over the Georgia coast in the south-eastern United States.

Afterwards, for the first time, instruments designed specifically to study TGFs and related phenomena from orbit were in flight or in preparation. The first such instrument to be launched was the gamma-ray spectrometer onboard the RISING microsatellite in January 2009. Molniya-Gamma, a Russian experiment on the International Space Station (ISS), was installed in February 2011, with gamma-ray detectors covering the range 0.3–1 MeV and 16 ms time resolution. Other missions include the European ASIM experiment for ISS (Neubert 2009), and the US nanosatellite Firefly and its sister instrument, called Firestation, for ISS. While varying significantly in scope, specialization, and capabilities, what all these missions have in common is additional instrumentation to simultaneously study optical emission from lightning and transient luminous events along with high-energy radiation. In particular, as reported in Neubert (2020), a TGF and an associated elve, which is a TLE described in Sec. 1.3, were observed by ASIM. The TGF occurred at the onset of a lightning current pulse that generated the elve.

In recent years, some TGFs have been detected from the ground, thus some of these detections are reported. In Wada (2019), is stated that on 9 January 2018 two types of high-energy events have been detected from thunderstorms: one is TGF and the other is gamma-ray glow, whose characteristics are described in Sec. 1.2. Four detectors were used and each one of them was made of $Bi_4Ge_3O_{12}$ scintillation crystal coupled with two photomultiplier tubes (PMTs), and worked in a 0.4 - 20 MeV energy range. Especially, two of this four detectors were responsible for the TGF detections and they were placed at Kanazawa Izumigaoka High School and at Kanazawa University High School. A couple of years later, in Hisadomi (2021), another TGF detection from ground was reported. On 12 January 2020, in the same location and with the same instruments described in Wada (2019), four gamma-ray enhancements were detected in the light curve. The first pair was simultaneously observed and were abruptly terminated by a lightning discharge. The remaining two enhancements were also nearly simultaneously observed 3 min later, and one of them was also terminated by another lightning discharge. At the last termination, a downward terrestrial gamma-ray flash was observed. Both pairs were associated with thundercloud cells.

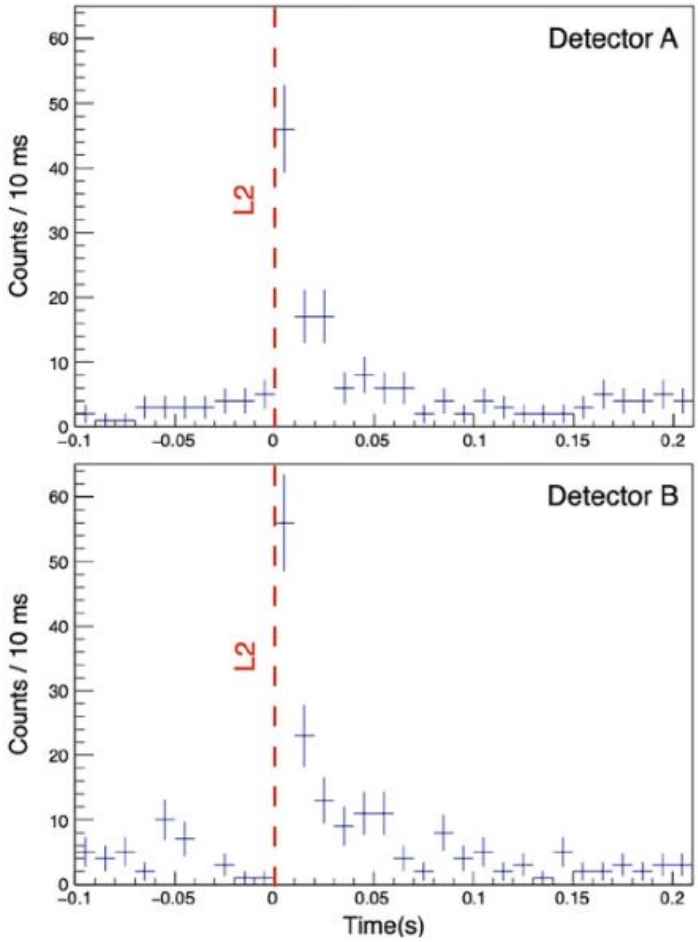

Figure 1.4: Light curves of a downward TGF recently detected from ground. It is observed by two detectors (A and B) in the 3-20 MeV energy band and it is coincident with a lightning discharge (L2). (From Hisadomi 2021).

Overall, the TGFs connection with thunderstorms in general and, more specifically, to some form of lightning process has been confirmed by many studies since their discovery. But the precise relationship between TGFs and lightning, and what kind of lightning processes are involved, remain not completely understood. Primary challenges are identifying the distribution functions of TGFs in luminosity, altitude, and beaming angles. One difficulty lies in the ability of all these quantities at once to affect the spectral hardness and fluence of a given TGF in ways that are hard to disentangle. Furthermore, instrumental triggering thresholds, dead-time and saturation effects of the instruments used for the observations complicate the process of the detections.

1.2 Gamma-ray glows

Gamma-ray glows, that are also called Terrestrial Ground Enhancements, have a production mechanism that is the same as the one described in the previous section for the TGFs. Electrons are accelerated to a relativistic energy due to the presence of an electric field inside a thundercloud, after that, by colliding with other atoms, they emit bremsstrahlung photons. The energy of these gamma-ray glows typically extends up to tens of MeV and their observed duration is of the order of seconds, which is the typical maximum duration for a lightning flash. Usually, lightning is observed to terminate the gamma-ray glows. Thus, they share similar production mechanism with TGFs, but they present different durations and relation with lightnings. In 2007, gamma-ray glows were first detected. Specifically, in Tsuchiya (2011), successful detections of two long-duration gamma-ray emissions extending up to 10 MeV were reported. Furthermore, some years later, in J. R. e. a. Dwyer (2012), the specific connection between X-ray or gamma-ray glows and lightnings was assessed: lightning generally terminates, rather than causes, these glows. Gamma-ray glows have been observed several times over the years and they are largely detected from space, from ground and by air-planes.

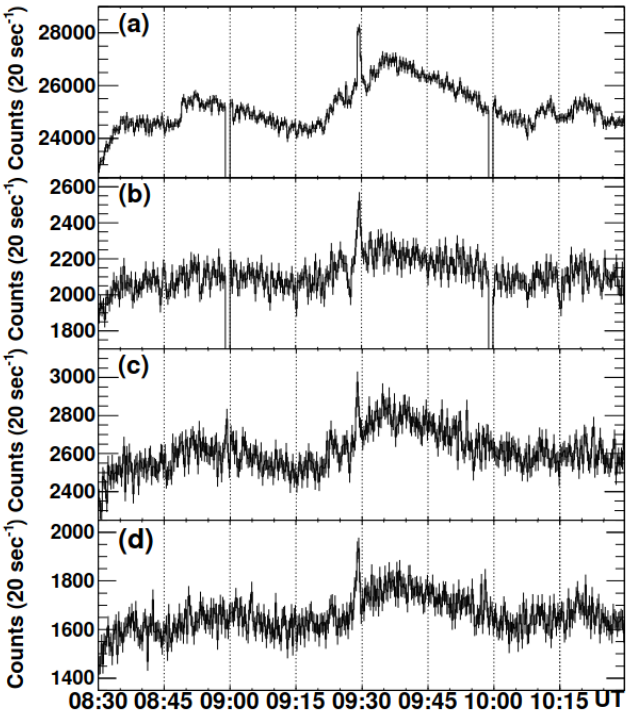

Figure 1.5: Light curves of one of the first gamma-ray glows detected, related to 4 inorganic scintillators. In particular, one gamma-ray glow, detected in 2008 by Gamma-Ray Observation of Winter Thunderclouds (GROWTH) experiment, is represented. Its duration is of some seconds. (From Tsuchiya 2011).

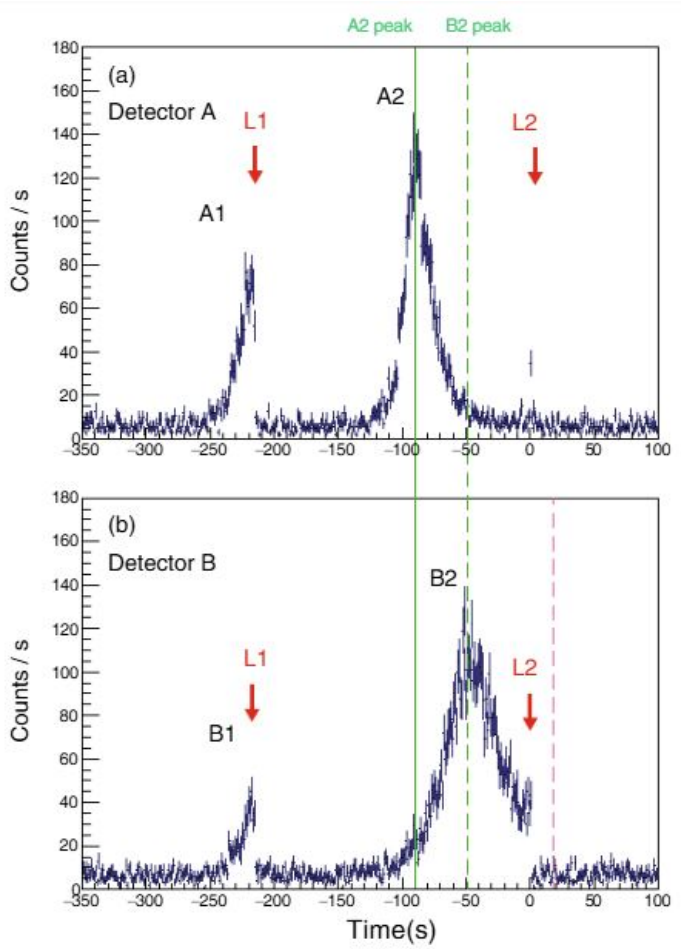

Figure 1.6: Light curves of gamma-ray glows recently detected from ground. They are observed by two detectors (A and B) in the 3-20 MeV energy band and each of them terminate with a lightning discharge (L1 and L2). (From Hisadomi 2021).

1.3 Transient Luminous Events

The TGFs connection with thunderstorms and to some specific lightning process has been confirmed and studied throughout the years, as previously stated. Therefore, a general description of the lightning formation and the main characteristics of some peculiar thunderstorm-related phenomena are reported in this section (Rakov, V. A. and Uman, M. A. 2003). The process that leads to the lightning formation and the related events starts with a thundercloud. Collisions between particles inside a thundercloud cause charge separation: lighter particles tend to acquire positive charge and rise to the top of the cloud, while heavier particles acquire negative charge and go

toward the bottom of the cloud. The charge separation leads to the creation of a strong electric field. Furthermore, the negative charges at the bottom of the thundercloud induce a positive charge on the ground below the cloud. At this stage, channels of ionized electrically conductive air form, which are called leaders. Thus, initiating the discharge process and the lightning. Moreover, several other thunderstorm-related phenomena, which take place in clear air above the thunderclouds, can occur. In particular, three general types of transient optical phenomena, referred to as TLEs, have been observed throughout the years: elves, red sprites and jets, the latter two are usually associated to TGFs. The elves in the lower ionosphere, at an altitude of 90 km. They accompany many lightning flashes and are manifested from the point above them as circles of light expanding radially across the bottom of the ionosphere. Usually, they last just for 1 millisecond. Red sprites, instead, take place in the mesosphere and are most luminous between 40 and 90 km heights. They often exhibit a diversity of forms and features, and frequently have faint blue tendrils extending downward to altitudes as low as 20 km. Typically, the duration of the red sprites is some milliseconds. Ultimately, jets manifest in the mesosphere, as for the red sprites. There are different kinds of jets, such as blue starters, blue jets and gigantic jets. Blue starters and blue jets propagate upward from the top of the thundercloud, in the form of blue cone-shaped structures. Starters propagate for less than 10 km, while jets up to 20 km. Gigantic jets instead, reach higher altitudes, terminating at 90 km. Generally, jets duration is some hundreds of milliseconds.

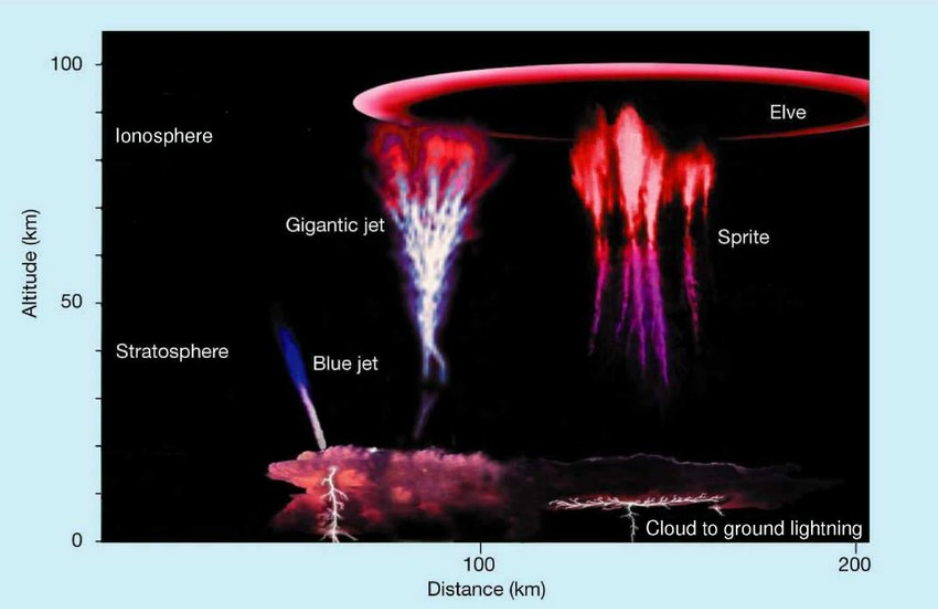

Figure 1.7: Sketch of some of the TLEs described in Sec. 1.3. Specifically, a elve, red sprites, a blue jet and a gigantic jet can be visualized. (From Pasko 2003).

Chapter 2

High-energy astrophysical transient phenomena

Some astrophysical transient phenomena are reported in this chapter. Especially, high-energy events, such as Gamma-Ray Bursts (GRBs) are analyzed in Sec. 2.1 considering several aspects. Their production mechanisms, characteristics and different emission phases are reported. Moreover, their detection history with related instruments used is outlined too.

2.1 Gamma Ray Bursts

This section analyzes GRBs considering various aspects, based on the treatment provided by Bambi, C. and Santangelo, A. (2024). Specifically, GRB phenomenon description is reported in Subsec. 2.1.1, considering progenitors and the leading production mechanisms. Afterwards, their primary emission phase, called prompt emission, is described in Subsec. 2.1.2. GRBs afterglows are presented, instead, in Subsec. 2.1.3. Ultimately, their detection history is outlined in Subsec. 2.1.4.

2.1.1 Phenomenon description

Considering a relativistic jet with a Lorentz factor Γ as the one that originates the GRB emission, the size of the GRBs emission region can be constrained at the scale of

$$R_{GRB} = 2\Gamma c\delta t \sim 6 \cdot 10^{12}\Gamma_{2.5}^2\delta t_{-3}\ cm \tag{2.1}$$

where δt is the variability timescale of the GRB light curves and the conventional notation $Q_x = Q/10^x$ is used in cgs units. Eq. 2.1 indicates that the GRBs progenitors may only be on the order of stellar systems. Regarding the typical GRBs fluence $F \sim 10^{-7} - 10^{-4}$ erg cm^{-2} and their cosmological distances, the isotropically equivalent energy release of the GRBs can be considered as

$$E_{iso} = \frac{4\pi d_L^2 F}{1+z} \sim \frac{10^{50-53}}{1+z}\ erg \tag{2.2}$$

where $d_L \sim 10^{28}$ cm is the typical luminosity distance and z is the redshift. Considering a stellar system, such a huge energy release can only be supplied by gravitational energy from catastrophic contraction of the system from a large size to a few tens of kilometers. This kind of contracting system could only be a collapsing massive star or a merging compact binary, which corresponds, respectively, to the long and the short GRBs that can be observed. Thus, considering the processes described, the central engine of GRBs should be a compact object, such as Black Holes (BH) or Neutron Starts (NS), formed by stellar collapses or compact binary mergers. Specifically, most long GRBs reside in the brightest core regions of irregular star-forming galaxies, where the specific star formation rate is the highest. This fact appears to support the massive star collapse origin of long GRBs. In particular, Wolf-Rayet stars, whose initial mass can be higher than 20 $M_\odot$ and that can evolve as type Ib/c SNe, are the perfect candidate for this kind of process. This evolved massive star loses its outer hydrogen envelope because of strong stellar winds. Its core collapses rapidly under gravity and a BH with a hot dense disk forms. For short GRBs, the majority of them resides in elliptical or early-type galaxies. This indicates that short GRBs are not likely associated with the deaths of massive stars, but are more consistent with compact binary mergers. Specifically, this binary system can be composed of Neutron Stars (NS-NS) or a Neutron Star and a Black Hole (NS-BH). Their orbit shrinks and, eventually, the two compact objects spiral together and merge violently. In this case, a BH surrounded by a hot dense disk can form too.

How such compact objects launch relativistic jets and extract the released gravitational energy is not completely understood. The hypercritical accretion onto the central engine during its formation may be a promising mechanism to explain this. Under these circumstances, the typical accretion rate is $\dot{M} \sim (0.1-1)\ M_\odot\ s^{-1}$ and it can be high enough to satisfy GRB luminosities:

$$L_{GRB} = \xi \dot{M} c^2 \sim 2 \cdot 10^{51}\ \xi_{-3}\ \left(\frac{\dot{M}}{1 M_\odot s^{-1}}\right) \tag{2.3}$$

where ξ is the radiation efficiency of the accretion. Considering the released gravitational energy, about half of it is initially stored as internal energy of the accretion disk. This leads the disk to be so hot that a great abundance of neutrinos/antineutrinos are produced. They can easily take away the internal energy because they can escape from transparent disk freely. Furthermore, gravitational energy can also be converted into rotational energy of the central engine and of the disk. At this stage, neutrinos and antineutrinos produced can annihilate above the disk to produce photons and electron-positron pairs, which are highly coupled to each other to form a fireball. This collection of particles can expand drastically due to the high radiation pressure, and

its dynamical evolution can be described by relativistic hydrodynamics. Then, the relativistic jet should first penetrate the thick progenitor medium, before producing the GRB emission. In the case of the stellar collapse scenario for long GRB, the medium is the stellar envelope, while regarding compact binary merger scenario for short GRB, the medium is the merger ejecta. The collision between the jet and the progenitor medium can lead to a forward shock sweeping up the medium and a reverse shock accumulating the jet material. There is a region between these two shocks, where the material is very hot and flows quickly and laterally to form a cocoon surrounding the jet. This region is called jet head and its velocity is determined by balancing the ram pressure of the forward-shocked medium and the reverse-shocked medium jet. The high pressure of the cocoon can drive a collimation shock into the jet material toward the jet axis. Thus, the jet can be gradually collimated and its material can be pushed and accelerated. Furthermore, the collimation is also due to the magnetic field. Afterward, when the jet breaks out from the progenitor medium, the GRB prompt emission can be produced. The typical GRB prompt emission spectrum is non-thermal. Thus, the prompt emission is likely produced by the dissipation of the kinetic energy. GRB jet may be considered not as a continuous fluid, but as a series of intermittent shells of different velocities. Therefore, kinetic energy due to speed difference can be easily dissipated when shells collide with each other. Furthermore, shocks can also effectively amplify the primordial magnetic field in the shell.

After the internal dissipation, a photosphere emission probably appears and is usually weak. Moreover, synchrotron radiation is produced and, accompanying it, the inverse Compton scattering occurs too. Relativistic electrons scatter off the synchrotron photons and this would lead to high-energy emission above hundreds of GeV, thus having the synchrotron self-Compton process. Nevertheless, these high-energy photons are further subjected to severe absorption via two-photon annihilation into electron-positron pairs. The absorption can happen inside the jet or far away from it. The high-energy photons that escape from the emitting region can interact with cosmic infrared background photons, producing electron-positron pairs. These secondary pairs can upscatter the cosmic microwave background, generating secondary gamma-ray photons, which lag behind the primary high-energy emission. Furthermore, the secondary pairs can be deflected by the intergalactic magnetic field, thus, the delayed high-energy emission deviates from the direction of the primary emission, forming a diffuse high-energy halo surrounding the GRB.

Thereafter, all the jet material would eventually behave as a single expanding ejecta, which moves into the circum-burst medium (CBM). Usually, CBM can be the interstellar medium (ISM) or a wind environment produced by progenitor star. Ejecta and CBM can interact and may drive a forward shock sweeping up the CBM and a reverse shock crossing the ejecta. The external reverse shock can only last a limited period, due to the very small thickness of GRB ejecta. This causes an optical flash, after which the flux decays. After the external reverse shock crosses the GRB ejecta, the external forward shock still exists and moves. It has a significantly longer duration than the

reverse shock and it is responsible for the afterglows in the other bands. The observed GRB afterglows show a large variety and complexity in their light curves. Thus, in addition to the ones described, some other factors can be present that can generate extra emission components.

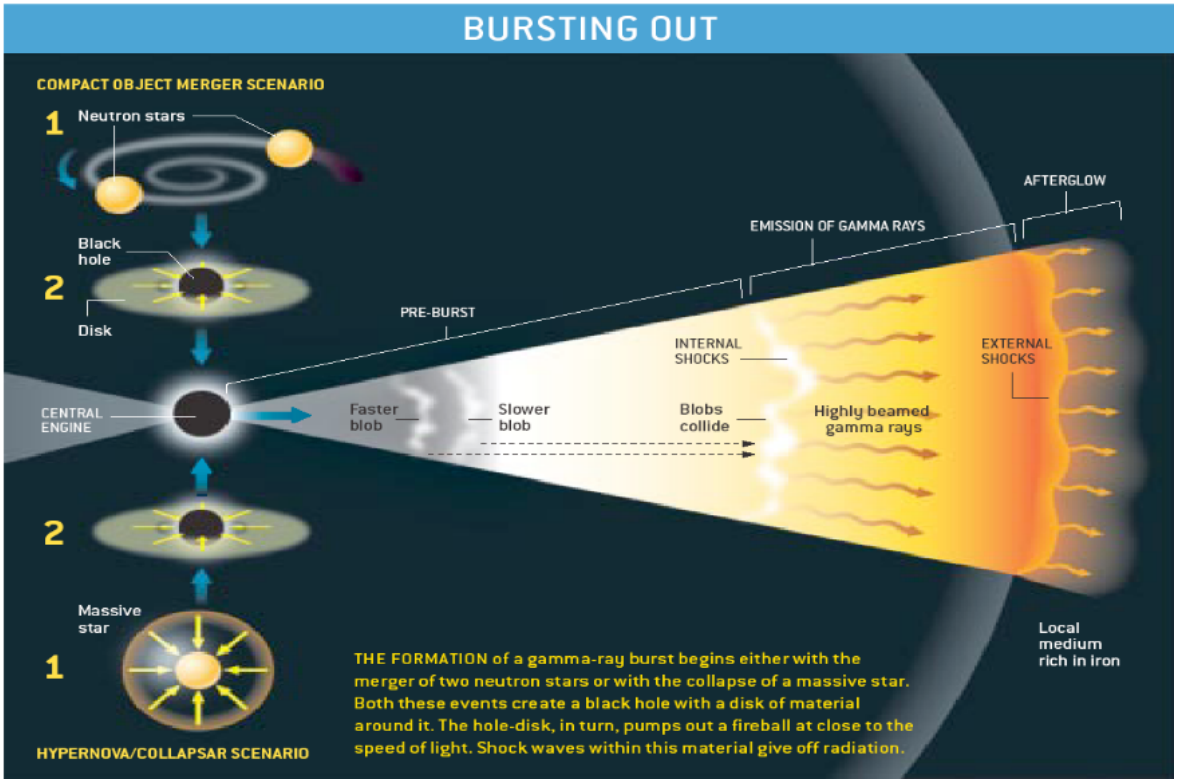

Figure 2.1: A general GRBs production scheme, including the two possible progenitors scenarios, the internal shocks that lead to the prompt emission and the external shocks that produce the afterglows emission. These scheme shows all the main steps of the GRBs production, which are outlined in Subsec. 2.1.1. (From D'Avanzo Paolo (INAF-OAB) n.d.).

2.1.2 Prompt emission

The GRB prompt emission, whose production mechanisms are outlined in Subsec. 2.1.1, is represented by various, complex and variable shaped pulses. It is typically composed of several consecutive episodes separated by quiet periods in between. Generally, its duration goes from some seconds up to hundreds of seconds and its typical energy range is between X-ray and gamma-ray bands. The temporal properties of the prompt emission can vary on a burst-by-burst basis. Thus, GRB prompt emission light curves shapes can vary from a single smooth pulse to extremely complex forms

with many irregular pulses with different durations, amplitudes and structures. Furthermore, prompt emission light curves may be decomposed as the superposition of an underlying slow component and a faster component, and they can vary with energies. Specifically, the latter contributes the most in high energies, whereas the slow component is more significant in softer energy bands. The GRB spectrum is typically non-thermal.

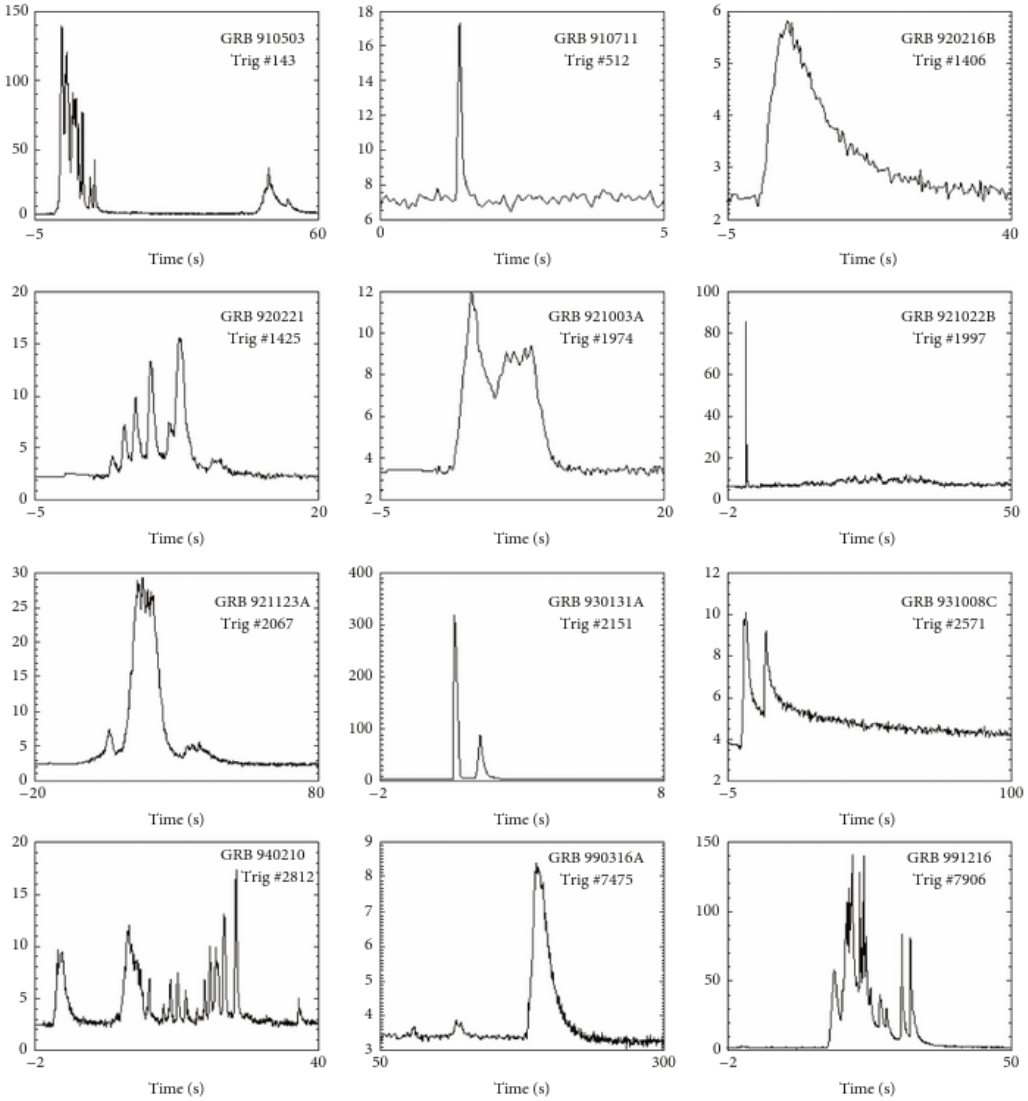

Figure 2.2: Light curves of 12 GRBs detected by BATSE. Both short and long duration GRBs are present in this sample. A large amount of patterns are shown, including events with smooth behaviour and single peaks and events with highly variable, erratic behaviour with many peaks. (From Pe'er 2015).

2.1.3 Afterglows

The GRB afterglows, whose production mechanisms are described in Subsec. 2.1.1, occur after the prompt emission and are observed in different energy bands, with durations even up to days or months. Five components may be present in the X-ray afterglow light curve, which are illustrated in Fig. 2.3: a distinct rapid decay, a shallow decay, a normal decay, a post jet break and the X-ray flares. The rapidly decaying component behaves as the "tail" of the prompt emission, then, the shallow decay is usually adjacent to the steep decay phase and is followed by a normal decay. However, sometimes the normal decay directly follows the steep component. A post jet break with a steeper decay comes after the normal decay, while, at last, there are the X-ray flares. The optical afterglow is more complex than the X-ray afterglow, but a large portion of GRBs have no detectable optical afterglow. This is mainly due to the heavy dust extinction within the GRB host galaxies. Furthermore, in some optical afterglows of long GRBs, a bump feature can appear about a week after the GRB trigger. This feature is usually interpreted as the signature of an associated supernova. However, in the case of short GRBs, an optical/IR transient fainter than a supernova is predicted. It is commonly referred to as kilonova. Ultimately, concerning radio and high-energy afterglows, they exhibit relatively simple behaviors. The radio afterglow typically reaches a peak after 3-6 days. Usually, at high energies there is a dramatic drop in the number of photons, making afterglows detection at higher energies more difficult than at low energies.

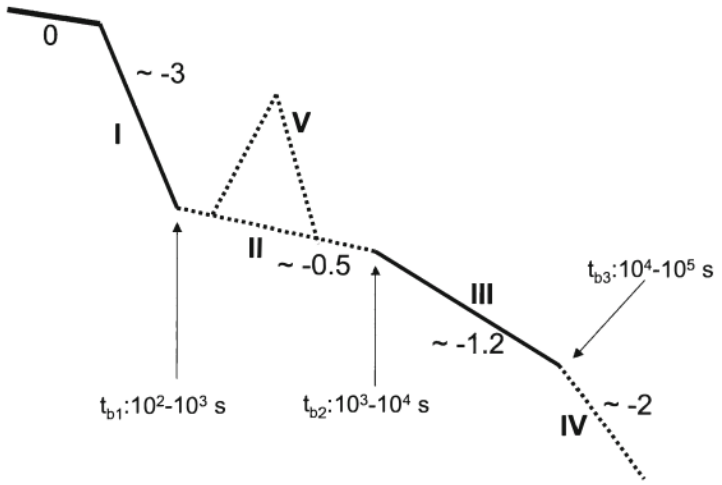

Figure 2.3: An illustration of X-ray afterglow light curve. After the prompt emission (0), the afterglow can occur. The five afterglow components depicted are the ones described in Subsec. 2.1.3, and they are reported in the same order. I and III components are the most common, whereas the other three are observed only in a fraction of bursts. Slopes and temporal indices are also represented for the different segments. (From Zhang 2006).

2.1.4 Detection history

In Subsec. 1.1.4, it has been reported that TGFs were first discovered by BATSE on board CGRO, whose primary target was GRBs. In turn, GRBs were first discovered by a spacecraft intended to detect gamma-ray flashes from below, as an indication of atmospheric nuclear tests. In particular, GRBs were first discovered in 1967 by the Vela satellites and they were reported as astronomical phenomena in 1973. In Klebesadel (1973), observations were made by detectors on the four Vela spacecraft (Vela 5A, Vela 5B, Vela 6A and Vela 6B), which were arranged almost equally spaced in a circular orbit. Six CsI scintillation counters were distributed on each spacecraft, in order to achieve a nearly isotropic sensitivity. Vela 5 and Vela 6 spacecraft worked, respectively, in 0.2-1.0 MeV and 0.3-1.5 MeV. Sixteen bursts were reported and their time durations ranged from less than a second to about 30 s. They were assessed as cosmic phenomena, but their specific origin and production mechanism were not understood yet.

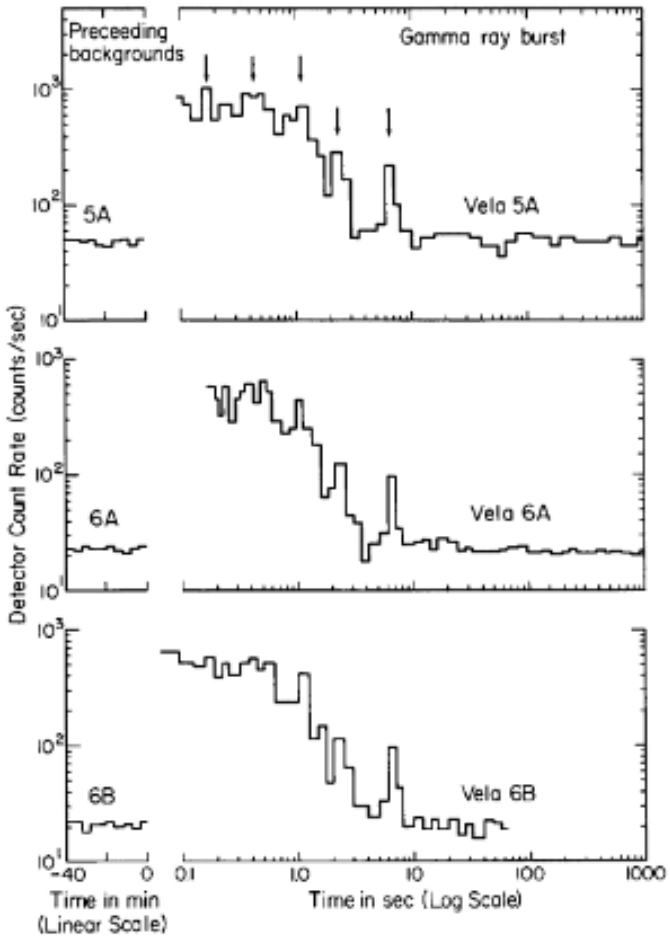

Figure 2.4: Light curves of one of the first GRBs detected, observed by three Vela spacecraft. Irregular pulses characterize its structure. (From Klebesadel 1973).

Afterwards, in 1992, BATSE revealed the isotropic distribution of GRBs in the sky. This indicated that they have an extra-galactic origin at cosmological distances rather than originating in our galaxy. Moreover, a year later, in Kouveliotou (1993) GRBs were classified into two categories: the long-duration soft-sperctrum class and the short-duration hard-spectrum class. The separation line between long and short GRBs is still not fully clear, but it is conventionally set at about 2 s.

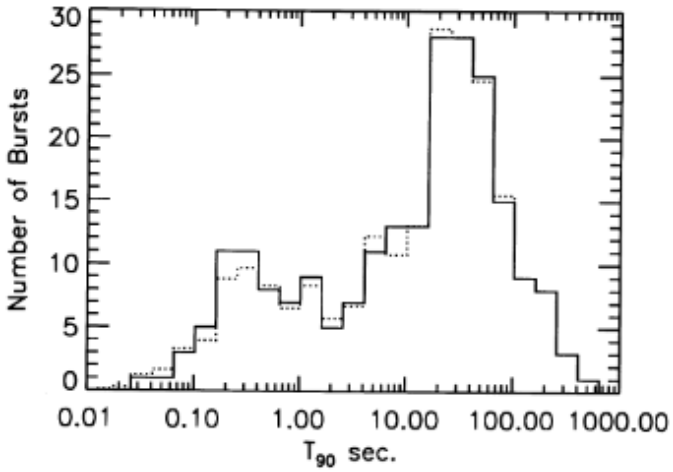

Figure 2.5: T_{90} distribution of 222 GRBs. T_{90} is defined as the time in which the cumulative counts increase from 5% to 95% above background (90% of total GRB counts). The distribution shows a dip around 2 s, representing the division between short and long GRBs. (From Kouveliotou 1993).

In 1996, the Italian/Dutch Beppo-SAX satellite was launched and it worked in the energy range from 0.1 keV up to 300 keV. In 1997, Beppo-SAX observed an X-ray counterpart of GRB970228 and the X-ray emissions exceed the sensitivity of the detector for about 1 week. Thanks to X-ray observations, the accuracy of GRB localization was significantly enhanced. This made it possible to monitor the transient counterparts also in the optical and in the radio bands. These long-lasting multi-wavelength transient counterparts of GRBs are now well known as afterglow emission, while the sub-MeV gamma-ray emission is called prompt emission. Furthermore, in 1997, the spectroscopic redshift of the possible optical counterpart of GRB970508 was measured by Metzger (1997). Thus, the redshift of the GRB can be obtained from absorption or emission lines and it confirmed the extra-galactic origin of the GRBs.

The cosmological origin of GRBs indicates that they are the most explosive phenomena in the universe after the Big Bang. Furthermore, the rapid variability of the GRB prompt emission gives a stringent constraint on the size of the emission source. Thus, the GRB should be produced by a relativistic jet originated from a catastrophic event of a stellar system. A first GRB production scenario was presented in Eichler

(1989). Specifically, the merger of compact binaries, such as neutron star collision, was considered to originate neutrino bursts and gamma-ray bursts, the latter should comprise a subclass of short GRBs observed. Afterwards, another production mechanism was described in Woosley (1993). In this case, the collapse of a special category of massive stars was considered to originate longer complex GRBs observed. The first production scenario was confirmed only after a long time, in 2017, when a GRB was confidently associated to a gravitational wave. The other production mechanism was proved by the discovery of supernova emission emerging from optical afterglow of some nearby GRBs.

The launch of the Swift satellite in 2004 marked a major step forward in GRB observations, providing a large number of data that allowed related detailed studies (Gehrels and Swift Team 2005).

In 2008, Fermi was launched. Thus, due to the combination of data obtained from the GBM and the LAT in the 10 keV - 100 GeV energy range, several GRBs observations have been collected throughout the years. This has allowed further studies regarding GRBs production mechanisms and related effects and events.

At this stage, it becomes of crucial importance in the GRB research field to fully understand how the stellar catastrophic events of the two scenarios reported can generate a relativistic jet and how such a jet produces the GRB prompt and afterglow emission. Furthermore, since GRBs are the most distant detectable objects due to their luminosity, it is also widely discussed whether and how they can be used as tools to probe the universe. For instance, they may allow the study of conditions in the early universe and they can also enable the tracing of star formation rate over cosmic time.

Chapter 3

Gamma-Flash and PIZ-Gamma projects

In this chapter, a project devoted to the investigation of high-energy atmospheric transient events is presented. It is called **Gamma-Flash** and is an Italian program, whose aim is the study of high-energy thunderstorm-related transient phenomena with a primary focus on TGFs and gamma-ray glows. The project is funded by the Italian Space Agency (ASI) and led by the National Institute for Astrophysics (INAF) in collaboration with several other institutions and Universities, such as the Institute for Atmospheric Science and Climate (CNR-ISAC), the "Tor Vergata" University of Rome, the Interdepartmental Centre for Nanosciences & Nanotechnologies & Instrumentation (NAST) of Rome, the University of Padua and the Inter-University Consortium for Space Physics (CIFS). Furthermore, a spin-off project of the Gamma-Flash experiment, which was proposed and realized by Fondazione Bruno Kessler (Trento) in collaboration with INAF/OAS Bologna, is also presented. This project is called **PIZ-Gamma** since it shares the same objective of Gamma-Flash and is located at the Piz Boè mountain refuge (Canazei, TN). Gamma-Flash and PIZ-Gamma share the same aim as stated, but use different acquisition systems. These two projects are described in this chapter considering several aspects. In particular, the gamma-ray detection process related to the instruments used is described in Sec. 3.1. An overview regarding the projects experimental sites is reported in Sec. 3.2. The latest installed setups are described in Sec. 3.3. The limitations of these instruments and the optimization processes carried out are analyzed in Sec. 3.4. Moreover, the experimental methodologies and the data analysis are addressed in Sec. 3.5. Ultimately, the first results obtained within the two interconnected experiments are presented in Sec. 3.6.

3.1 Detection principle

In this section, an overview of the general gamma-ray detection process related to the instruments used for the experiments is outlined. Both projects employ gamma-

ray detectors, as they share the same scientific goals. The main architecture of these detectors is similar: in both experiments a scintillation crystal made of Cesium Iodine doped with Tallium CsI(Tl) or Sodium Iodine Tallium-doped NaI(Tl) is coupled with a system to read the scintillation light. In the Gamma-Flash experiment the readout mechanism is a PhotoMultiplier Tube (PMT), whereas for the PIZ-Gamma experiment the readout mechanism is performed through the Silicon PhotoMultiplier (SiPM) technology. Each system also includes dedicated acquisition boards, which differ between the two setups.

The detection principle of gamma-ray for these two type of detectors is the same and is direct: a photon interacts and ionizes matter, thus obtaining an electric charge proportional to the photon energy. In particular, photons interact with a scintillation crystal, which is a material that converts an energy deposit (from a photon or a charged particle) in optical/UV photons. Scintillators can be organic or inorganic and they are usually doped, since through the excitement of additional activator energy levels and their related transitions, the optical photons are produced. Furthermore, the amount of light generated by the scintillator is proportional to the deposited energy. In an "ideal" detector, the incoming photon deposits all its energy inside the detector, but for a real detector there are several effects that take place and affect its response. These effects are related to the interaction of photons with matter. In particular, these photons come directly from the source and interact with the scintillation crystal, depositing their energy, or escaping the detector. In addition, the detector response can be affected also by photons interaction with surrounding materials.

High-energy photons from the source interact with the scintillation crystal primarily through photoelectric effect, Compton scattering, and pair production. Among these, the photoelectric effect is the dominant process at low energies. In the photoelectric effect, a photon is completely absorbed by an atom in the crystal, transferring all its energy to an inner-shell electron, which is subsequently ejected. The resulting vacancy is filled by electrons from higher shells, producing characteristic X-rays or Auger electrons that rapidly deposit their energy within the crystal. Consequently, the entire photon energy is converted into scintillation light, giving rise to the photopeak in the measured spectrum, which is an essential feature for accurate energy determination. The photopeak for a scintillation detector has a Gaussian profile and its width depends on the type of scintillator. Regarding Compton scattering, it involves only partial energy transfer: the photon interacts with a loosely bound electron, and the scattered photon may escape the detector. This process generates a continuum in the spectrum that extends up to the Compton edge, corresponding to the maximum possible energy transferred to an electron. At higher photon energies, pair production becomes significant. When the photon energy exceeds 1.022 MeV, an electron–positron pair can be created in the vicinity of an atomic nucleus. The positron eventually annihilates with an electron, producing two 511 keV photons. If one or both of these photons escape the detector, single or double escape peaks appear in the spectrum, respectively. The detector response can also be affected by interactions in surrounding materials. Pho-

tons scattered by the environment and re-entering the detector produce a backscatter peak. Fluorescence from surrounding elements, instead, gives rise to additional characteristic X-ray lines. Moreover, the 511 keV annihilation peak associated with pair production is often visible, reflecting secondary interactions beyond the crystal itself. All the described features in the spectrum detected with a scintillator based detector, are described in Fig. 3.1.

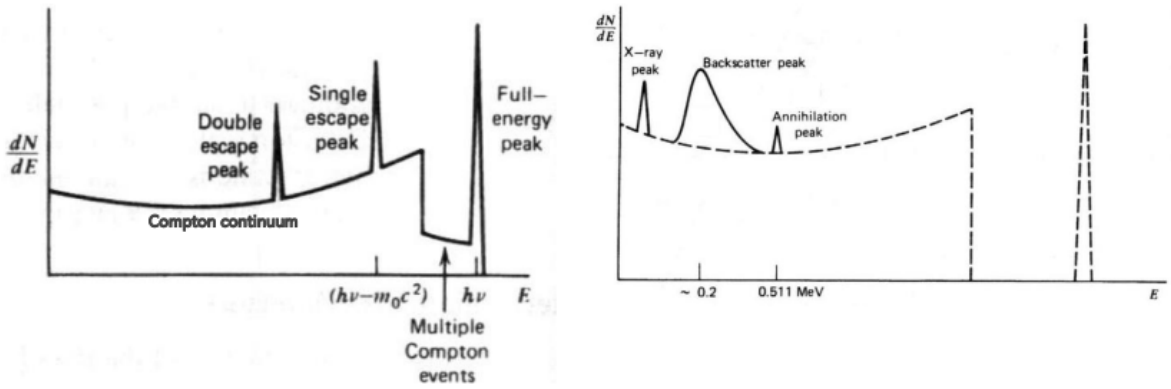

Figure 3.1: *Left image*: Features of gamma spectrum due to photons coming directly from the source interacting with matter. Specifically, effects described in this section related to photoelectric effect, Compton scattering and pair production are depicted. *Right image*: features of gamma spectrum due to photons coming from surrounding materials interacting with matter. In particular, effects described in this section related to Compton scattering, pair production and fluorescence are represented.

After the high-energy photons have interacted with the scintillation crystal in the ways just described, the optical photons produced need to be collected. Thus, the scintillator can be coupled with a PMT (for Gamma-Flash) or with a SiPM (for PIZ-Gamma) for this purpose.

A PMT is a highly sensitive photon detector that operates on the principle of converting incident optical photons into an amplified electrical signal through a sequence of photoemission and secondary electron multiplication stages. When scintillation light impinges on the photocathode, photons interact with the photosensitive material via the photoelectric effect, releasing photoelectrons whose number is proportional to the incident photon flux and the quantum efficiency of the photocathode.

A high voltage, typically of the order of several hundred to a few thousand volts (900 V in the case of the PMTs used in Gamma-Flash), is applied between the photocathode and the anode. A series of dynodes lies between these two electrodes and each dynode is maintained at an increasingly positive potential with respect to that of the preceding stage. The electric field thus established accelerates the photoelectrons toward the first

dynode, where each impinging electron liberates several secondary electrons through impact-induced emission. These newly generated electrons are in turn accelerated toward the next dynode, repeating the process of secondary emission and producing an electron avalanche that exponentially amplifies the original signal.

After multiple amplification stages, which are typically between 8 and 14 dynodes, the resulting electron cloud reaches the anode, where it is collected to produce a measurable current pulse. The total amplification or gain of a PMT generally ranges from 10^6 - 10^7, depending on the applied voltage and the number of dynodes. The resulting signal is then processed by the readout electronics or data acquisition system.

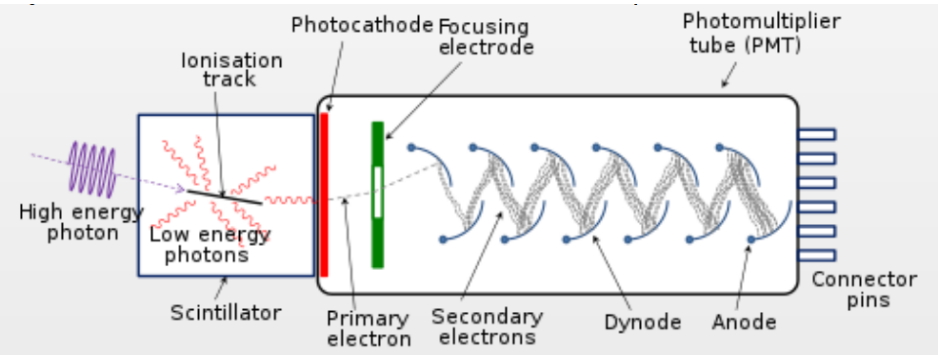

Figure 3.2: Sketch of a scintillator coupled with a PMT, along with the gamma ray detection process scheme.

Concerning the SiPM, it also converts photons into electrons, but the process is different with respect to PMTs. The SiPM is an array of Single-Photon Avalanche Diodes (SPADs). The bias applied, whose typical value is usually $\sim$ 20-30 V, is above the breakdown voltage (voltage at which the electric field is high enough to trigger avalanche multiplication process). Thus, even a single photon hitting one pixel (SPAD) of SiPM generates several electrons. At this stage, there is an internal charge multiplication and an avalanche effect is obtained from a single photon. SiPMs present a more compact structure with respect to the PMTs, thus, they can be used also when there is little space available. Furthermore, they can work with a lower voltage and have a higher quantum efficiency with respect to the PMTs. Nevertheless, there are also some disadvantages related to the use of SiPMs: sometimes SPADs can generate signal even without photons hitting the detector (due to thermal excitation), so dark current can be present, and the SiPM ability to amplify the signal is temperature dependent. However, after the avalanche effect, the final analog signal is proportional to the number of pixels (SPADs) fired. This signal can be detected and acquired by the acquisition board.

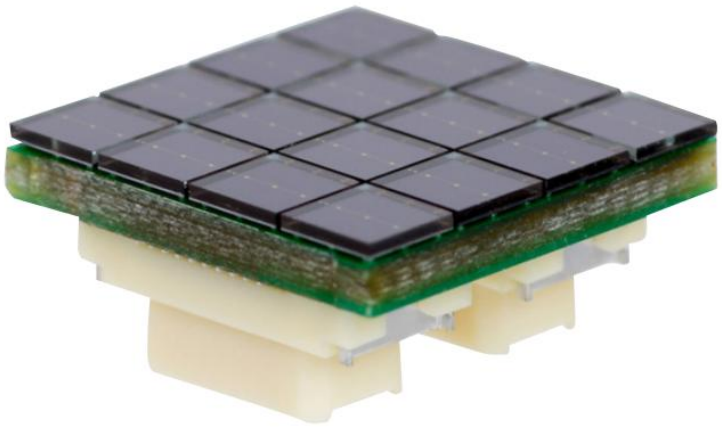

Figure 3.3: Representation of a 4×4 pixels SiPM.

3.2 Experimental sites

This section describes the general characteristics of the Gamma-Flash and PIZ-Gamma experimental sites, comparing their shared features and distinctive attributes that make them suitable for observing atmospheric gamma-ray transient phenomena. When investigating these kind of phenomena from ground, various difficulties are always present. Among these issues, one is linked to the high-energy emission due to the decay chain of radon washed out by rain. In particular, the radioactive decay products of ^{222}Rn, such as ^{214}Bi, during rains are brought down to the ground, causing a temporary increase in the gamma-ray counts. The only way to cope with this issue is performing an analysis of the observed data. There are mainly two aspects that should be considered: the different durations of the high-energy thunderstorm-related transient phenomena and the radon washout event, and also their respective spectra, which have specific features that can be distinguished. Specifically, high-energy radiation enhancements last from minutes to hours in the case of radon washout. TGFs and gamma-ray glows durations range from tens to hundreds of microseconds and from seconds up to several minutes, respectively. Regarding the spectra of the two events, radon washout ones present some specific emission lines, such as the ones related to ^{214}Bi. TGFs ones, instead, are smoother with a characteristic high-energy component above ~ 3 MeV, similarly to what observed also for gamma-ray glows. Therefore, these two characteristics related to the durations and the spectra of these events allow to distinguish gamma-ray enhancements caused by TGFs or gamma-ray glows from radon washout ones, solving this issue. Another difficulty always present when investigating this kind of phenomena from ground is related to the absorbing column of air between ground and the high-field regions of storms (at several km altitude). This issue can

be partially solved by the choice of experimental sites locations. They should be located at high altitudes, where the atmosphere is thinner. This reduces the atmospheric extinction of radiation and enhances the visibility of these phenomena. Indeed, from the ground TGFs and related events are mostly detected on mountain peaks. For this reason, both the Gamma-Flash and PIZ-Gamma projects are based at high-altitude sites, described, respectively, in the following Subsec. 3.2.1 and Subsec. 3.2.2.

3.2.1 Gamma-Flash experiment location

The Gamma-Flash project had an original setup that was placed at Osservatorio Climatico "Ottavio Vittori" located in Sestola (Modena) and in an aircraft. These two experiments had the objective of observing gamma-ray atmospheric transients both from the ground and from high altitude (9000-13000 m). For this reason, two similar detection systems were realized in the laboratories of INAF / OAS Bologna, one of the two with the specific properties to be installed on an aircraft. In particular, this aircraft system was powered with 24 volt batteries independent of the aircraft to avoid interference with flight. After the planned flights, the aircraft system was adapted for ground installation and brought to the Osservatorio Climatico "Ottavio Vittori" in order to increase the detection area of the ground installation.

The latest configuration of the experiment is set up at Osservatorio Climatico "Ottavio Vittori", which is located in Emilia-Romagna on the top of Mt. Cimone at an altitude of 2165 m a.s.l. From this specific site, it is possible to have a free line of sight observing a significant portion of the northern Italian territory, and also this geographical region is interested by frequent lightning activity and associated detection of TLEs [Ursi (2022)]. Therefore, because of this characteristic just reported and also due to the altitude of the site, this location was chosen. It is suitable for the investigation of high-energy emission thunderstorm-related transient phenomena. In particular, the setup, whose instruments and details are discussed in Subsec. 3.3.1, was installed on the external terrace of this observatory, which is shown in Fig. 3.4. It is placed inside a fiberglass naval dome of 126 cm diameter, preventing it from weather-related problems, such as wind, rain, and snow. In addition, the 3 mm thick fiberglass cover ensures a negligible absorption of the photons at energies above a few hundreds of keV, which are the main target of this experiment.

Figure 3.4: *Left*: View of the "Ottavio Vittori" CNR/ISAC laboratory. *Right*: terrace where the naval dome with the Gamma-Flash instrumentation is installed.

3.2.2 PIZ-Gamma experiment location

The PIZ-Gamma setup was installed near the Piz Boè refuge (2871 m a.s.l) on one of the highest peaks of the Dolomites, in Trentino-Alto Adige. In particular, a significant portion of the northern Italian territory can be observed from this site and, similarly to Mt. Cimone, it is also usually affected by frequent thunderstorms, especially during the summer season. Furthermore, the altitude of this site along with the characteristic just stated make this location suitable for the aim of the project, which is the same of the Gamma-Flash one. In particular, the setup consists of two gamma-ray detectors, whose instruments and characteristics are discussed in further details in Subsec. 3.3.2. Each detector is enclosed into a sealed watertight box. The two boxes are placed outside the Piz Boè refuge.

Figure 3.5: Location of the Piz-Gamma experiment

3.3 Setups instruments description

The latest and current setups of Gamma-Flash and PIZ-Gamma projects are described in this section. The general structure of the gamma-ray detectors used for these projects is the same, as stated in Sec. 3.1, but their distinct components present various differences. Therefore, specific descriptions of the different setups are addressed in Subsec. 3.3.1 and Subsec. 3.3.2, respectively, for Gamma-Flash and PIZ-Gamma.

3.3.1 Gamma-Flash current setup

The latest and current setup of the Gamma-Flash project is at Osservatorio Climatico "Ottavio Vittori". It consists of a weather station, a PC and eight gamma-ray detectors with the respective readout electronics. The weather station allows to monitor the temperature of the surrounding environment, that can affect measurements. Furthermore, in order to study and assess the correlation between lightnings and high-energy transient phenomena, data acquired by Lightning Network (LINET) can be used. The PC allows to store data from acquisitions and it is possible to access it remotely to acquire the collected data. The eight gamma-ray detectors are installed and used to detect both short-duration transient phenomena such as TGFs and longer duration transients such as gamma-ray glows. This setup is shown in Fig. 3.6.

Figure 3.6: Gamma Flash current setup installed at Osservatorio Climatico "Ottavio Vittori" on Mt. Cimone. Four gamma ray detectors are inside the grey metal box on the left. On one side of this box, there is also the PC. The other four gamma ray detectors with another configuration are the black ones on the right. The weather station is shown on the back of the setup.

Four gamma-ray detectors , made of NaI(Tl) coupled with PMTs, are placed inside an aluminum box that is installed in the fiberglass naval dome. The PMT is powered by a survoltor providing $\sim$ -700 volts. The acquisition of the readout signal is based on the RedPitaya STEMlab 125-14 board, which is connected to the PMT and ultimately to the PC. These instruments are referred to as type I configuration Gamma-Flash detectors.

The electrical pulse produced at the output of the PMT is a fast analog signal, typically a few nanoseconds wide, whose temporal development and amplitude is recorded through the RedPitaya STEMlab 125-14 Analog to Digital converter system. For this purpose, the readout electronics need to digitize the waveform with high frequency sampling. The PMT signal can be sampled at minimum every 8 ns, corresponding to a sampling rate of 125 MS/s. At each clock sample the value of the analog voltage is quantized into a digital number. The sampling should be small enough compared to the characteristic rise and decay times of the PMT pulse allows an accurate reconstruction of the original waveform. At the same time, the waveform should not be over-sampled, as this would produce unnecessarily large data volumes without significantly improving the signal description. From the digitized signal, it is possible to extract the relevant pulse parameters, such as peak amplitude, integrated charge and precise arrival time.

The major limitation of the RedPitaya STEMlab 125-14 board is that the buffer length is fixed, depending on the sampling rate. For instance with sampling rate of 125 MS/s the length of the buffer is 131072 μs. After this time, a fixed time of 3 ms is required to stop the acquisition, send the data to the computer, reset and prepare the system for the next acquisition. If a longer time window is requested, it is possible to change the so-called decimation factor (described in details in Subsec. 3.4.1).

In the end, each individual waveform is acquired in order to obtain scientific data, such as light curves and spectra. However, the acquisition boards have specific characteristics and limitations; for this reason, optimization processes were carried out and are described in Subsec. 3.4.1. The four detectors, which do not operate in coincidence, are completely independent of one another therefore, if a transient signal is detected simultaneously in all detectors, it can be considered a real external event rather than a spurious signal caused by the electronics. The detectors are named *gammaflash1a*, *gammaflash1b*, *gammaflash1c* and *gammaflash1d*.

Four further gamma-ray detectors have been installed with a different readout electronics, each of them equipped with a CsI (doped with Tl) inorganic scintillator crystal, coupled with a PMT. The PMT is wrapped in Mylar, which is an isolating material, and the detector is built so as to isolate it from external optical light not coming from the scintillator. The acquisition board, which was produced by Fondazione Bruno Kessler (FBK), is inside the detector box. It performs various tasks: it amplifies the voltage supplied by the PC, it powers the PMT ($\sim$ 1000 V) and it also receives and acquires the output signal. This board is connected to the PC via a USB cable. These other four instruments are referred to as type II configuration Gamma-Flash detectors.

Thus, scientific data such as light curves and spectra, can also be obtained in this

configuration. As in the previous case, the acquisition boards were optimized with different procedures, which are described in Subsec. 3.4.2. Four gamma-ray detectors were built using the structure described above. They are used to compare their results and to verify the presence of the same transient event in all the detectors. The detectors are named *gammaflash2a*, *gammaflash2b*, *gammaflash2c* and *gammaflash2d*.

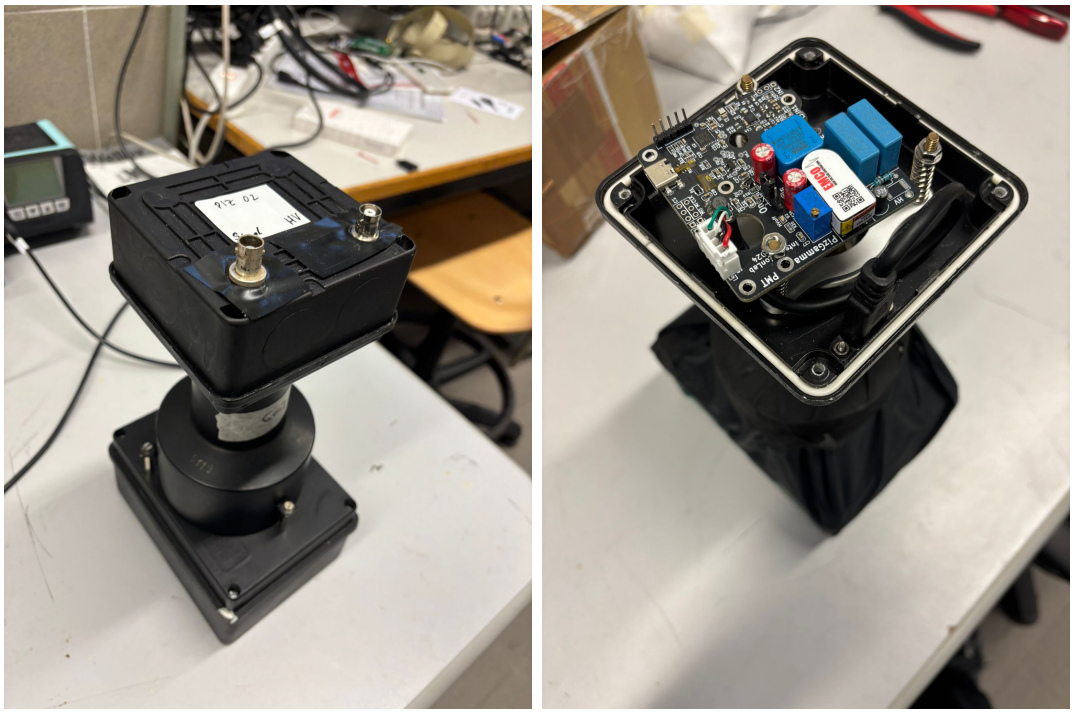

Figure 3.7: *Left image*: One of the four type II Gamma-Flash detectors shown from the outside. *Right image*: One of the four type II Gamma-Flash detectors shown from the inside, the FBK acquisition board can be observed.

3.3.2 PIZ-Gamma current setup

The current setup of the PIZ-Gamma project is outside the Piz Boè refuge. It consists of two identical gamma-ray detectors. Each one of them is placed inside a small grey box, as it is shown in Fig. 3.8. They are used for the high-energy thunderstorm-related transient phenomena detections and they can observe both short-duration events such as TGFs and longer-duration ones such as gamma-ray glows. Each one of these detectors has a CsI (doped with Tl) inorganic scintillation crystal, which is wrapped to isolate it from external optical light not coming from the scintillator. Moreover, the scintillation crystal is coupled with SiPM in this case. Each SiPM consists of a 4×4 pixel array, for a total of 16 pixels. Each pixel has dimensions of 6×6 mm^2. The

acquisition board is produced by FBK also for this setup. It is powered by a battery with $\sim$ 5 V and it is connected to a hard disk that stores the data collected during the acquisitions. These data are analyzed in order to obtain, as usual, light curves and spectra. These detectors are called *pizgamma1* and *pizgamma2*.

Figure 3.8: *Top image*: The components of one PIZ-Gamma detectors described in Subsec. 3.3.2, specifically, the scintillator crystal, the SiPM and the acquisition board are shown. *Bottom image, from left to right*: One of the two gamma-ray detectors of the PIZ-Gamma setup, which is placed in a sealed box. The two PIZ-Gamma detectors installed outside the Piz Boè refuge.

3.4 Detectors optimization

Some of the instruments described in Sec. 3.3 were ready-to use, such as the weather station for Gamma-Flash and the two gamma-ray detectors for PIZ-Gamma. For the other instruments, some modifications needed to be applied. In particular, optimizations and tests were performed before using both the four Gamma-Flash type I configuration and the four type II configuration detectors. The related activities carried out are described, in Subsec. 3.4.1 for type I detectors and in Subsec. 3.4.2 for type II ones.

3.4.1 Gamma-Flash type I - configuration tests

Activities related to the optimization of the acquisition were performed for the Gamma-Flash detectors with the readout electronics based on the Red Pitaya STEMlab 125-14 described in Subsec. 3.3.1.

A typical waveform acquired from a triggered photon event is shown in Fig. 3.9.

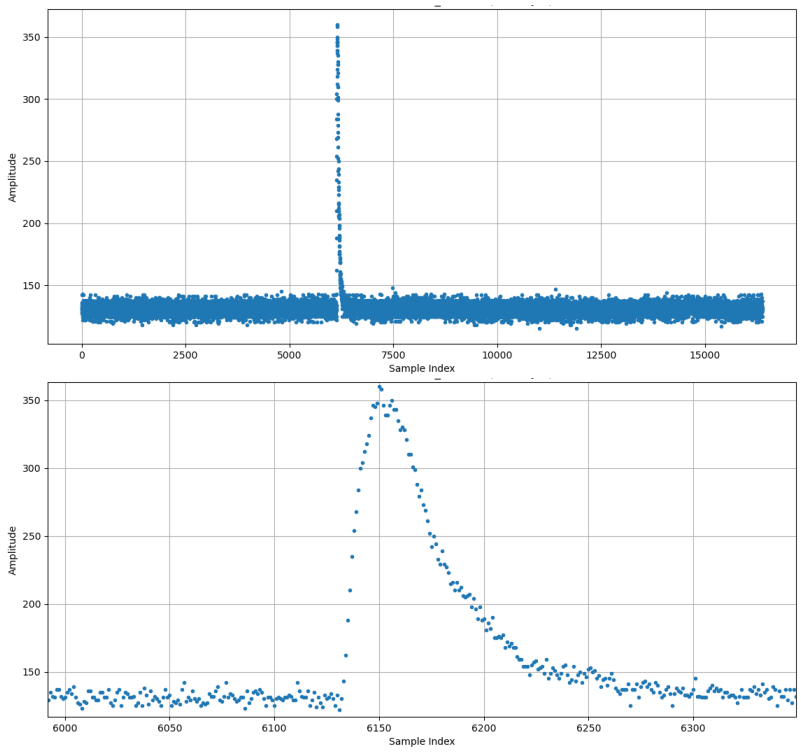

Figure 3.9: *Top image*: A typical waveform acquired by a Red Pitaya STEMlab 125-14. *Bottom image*: A zoom-in of the top image, in which the fast rise and the exponential decay of the waveform can be observed. The signal is positive since it was inverted.

The peak rising above the constant baseline level, as well as its characteristic shape, can be clearly observed. The lower panel shows a zoomed-in view of the same waveform. It is evident that the signal exhibits a fast rise followed by an exponential decay. The event is recorded with a sampling rate of 125 MS/s. This particular waveform is sampled with more than 100 points across the peak, which is sufficient to accurately characterize its shape. Such a high sampling density allows for a precise determination of the waveform profile with estimation of the integral under the curve, the peak amplitude (related to the energy of the original gamma-ray photon), and the index of the maximum, the latter being related to the time of arrival of the photon.

The acquisition of a single event is strongly influenced by how the input signal is digitized. The Red Pitaya boards use a 14-bit analog-to-digital converter (ADC), which can represent $2^{14} = 16384$ discrete digital levels. These levels span the voltage range from -1V to $+1$V: values from 0 to 8191 correspond to the interval 0–1V, while values from 8192 to 16383 map the interval -1–0V. Since the signals acquired by the detector are negative (falling within the -1–0V range), an appropriate trigger threshold must be set in order to correctly filter events. This threshold is controlled by the parameter *trigThresh*, which defines the digital value corresponding to the minimum detectable voltage. Therefore, it is related to the minimum energy threshold of the detector. By assigning a specific value to *trigThresh*, one selects a corresponding voltage and the related energy. This parameter can be configured independently for each acquisition board. In our setup, it was set to the same energy for all detectors to ensure consistent and comparable spectra. A value of 15700 was chosen, corresponding to a voltage of $-83,\mathrm{mV}$ and an energy of 1 MeV. All events with energies below this threshold are excluded.

The Red Pitaya acquisition system allows the adjustment of the effective sampling rate through a parameter known as *decimation*. This parameter scales down the original sampling frequency by an integer factor, reducing the number of samples acquired per unit time. As a result, both the temporal resolution and the total duration of the acquisition window are modified. For the boards used in this work, the relevant fixed parameters are the following:

- the buffer size is 16384 samples;
- the original sampling rate is $125 \cdot 10^6$ samples per second (125 MS/s).

When a decimation factor D is applied, the sampling rate becomes:

$$f_{\text{sample}} = \frac{125 \cdot 10^6}{D} \tag{3.1}$$

and the time interval between consecutive samples increases accordingly:

$$\Delta t = \frac{D}{125 \cdot 10^6} \tag{3.2}$$

The buffer always stores 16384 samples so the duration of the acquisition window is:

$$T_{\text{window}} = 16384 \cdot \Delta t \tag{3.3}$$

Larger decimation factors produce longer acquisition windows but with reduced temporal resolution, while smaller factors preserve fine time sampling at the expense of a shorter observable time span. The corresponding values of f_{sample}, Δt, and T_{window} for selected decimation factors are reported in Tab. 3.1. In Fig. 3.10 is shown the effect of choosing different decimation factors on the same waveform.

Decimation Factor	**Effective Sampling Rate**	**Time Intervals Between Samples**	**Acquisition Window Duration**
1	125 MS/s	8 ns	131 μs
2	62.5 MS/s	16 ns	262 μs
4	31.25 MS/s	32 ns	524 μs
8	15.625 MS/s	64 ns	1049 μs

Table 3.1: Comparison between effective sampling rates, time intervals between consecutive samples and acquisition window durations of four specific decimation factors.

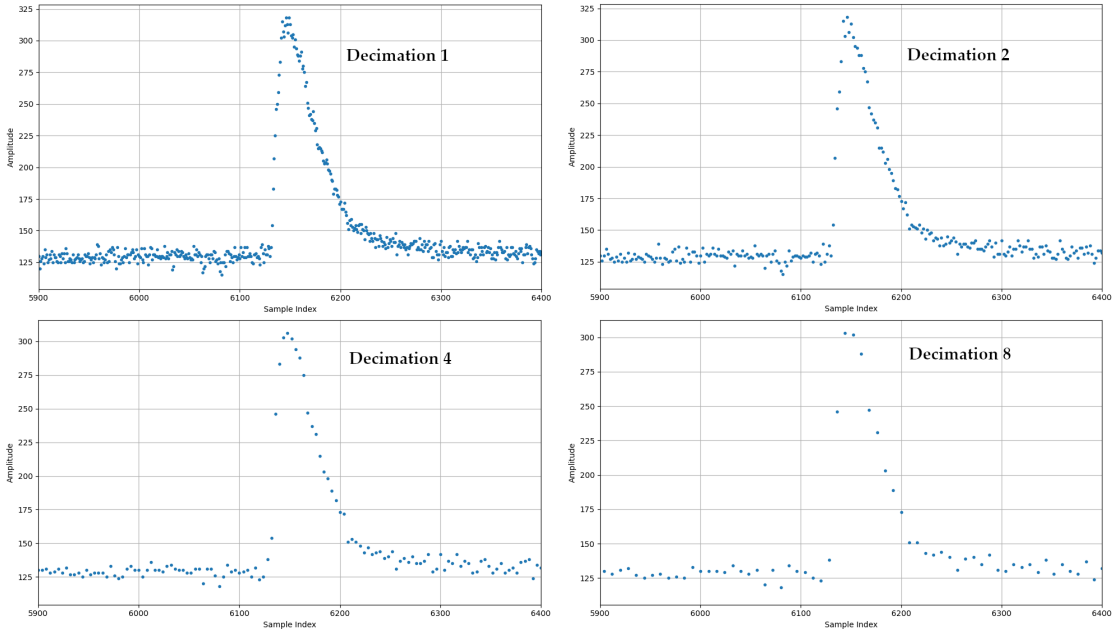

Figure 3.10: Decimation factors 1, 2, 4 and 8 applied to the same waveform.

The role of the decimation factor is important together with the dead time which is constant (3 ms) at the end of each acquisition window. We made simulations with a Python code in order to evaluate the fraction of lost photons (and equivalently the number of detected photons) with respect to the generated photons, due to the combination of the decimation and the dead time. The first step is the production of photons generated following a Poisson distribution. Whenever a photon interacts with the detector, it triggers the opening of the acquisition window, whose duration time depends on the decimation used. As other photons arrives on the detector with Poissonian distribution, they can be detected if they arrive within this time window. Each acquisition window is followed by a dead time with a fixed duration of 3 ms. All the photons that fall into the detector within this dead time, will be ignored and therefore will be lost. After this period, subsequent photons can trigger again the opening of the acquisition window.

In the simulations, the rate was set from 10 to 10^5 photons/s consecutively in step of 10 photons/s. Each simulation was done by generating 50000 photons; therefore, each simulation had a variable duration according to the photon rate. The same simulation was performed for the four different decimation factors: 1, 2, 4 and 8. According to the previous definitions, a decimation factor 1 corresponds to no reduction of the original sampling rate. For decimation factors 2, 4 and 8, the sampling rate is reduced by 1/2, 1/4 and 1/8, respectively. After choosing one of these four factors, the duration of the acquisition window is consequently fixed, as shown before by Eq. 3.3.

The results obtained from these simulations are shown in Fig. 3.11 for each decimation, in which the two curves represent the ratio between the detected number of photons with respect to the total number of generated photons, and the ratio between the lost photons (due to the dead time) with respect to the generated photons. The trends of both ratios are similar for the different decimation factors. At low photon rates, the ratio is close to 1, as the number of photons falling into the 3 ms dead time window is small compared with the number of photons effectively detected, while this ratio progressively decreases as the photon rate increases. Furthermore, by increasing the decimation factor, which results in a longer duration of the acquisition window, a higher number of photons is detected for the same photon rate. This is evident at higher rate: for example, at 10^5 photons/s the percentage of detected photons is 4, 9, 15 and 28% for decimation 1, 2, 4 and 8, respectively. On the other hand, the orange curve depicts the ratio of the lost photons with respect to the total number of generated photons. For decimation 1 at high count rate this value is close to 1, as the majority of the photons fall into the large dead time window. For decimation 8, the plateau of the curve at higher count rate is achieved at $\sim 70\%$ of the lost photons. In any case, for each decimation and for each rate, the sum of the the detected photon rate and lost photon rate is 1, as it should be.

These simulations confirm that a longer acquisition window enables the detection of a larger number of photons. Although higher decimation values would further extend the acquisition window, they also reduce the number of sampled points available to

reconstruct the waveform. Decimation factors 1, 2, 4 and 8 still provide sufficient sampling, moving to 16 would result in too few points to properly characterize the signal. In this sense, a decimation factor of 8 represents the upper limit beyond which waveform sampling would no longer be adequate. Therefore, decimation factor 8 can be a good trade-off. For this reason, and based on the simulation results, the decimation factor was decided to be set to 8.

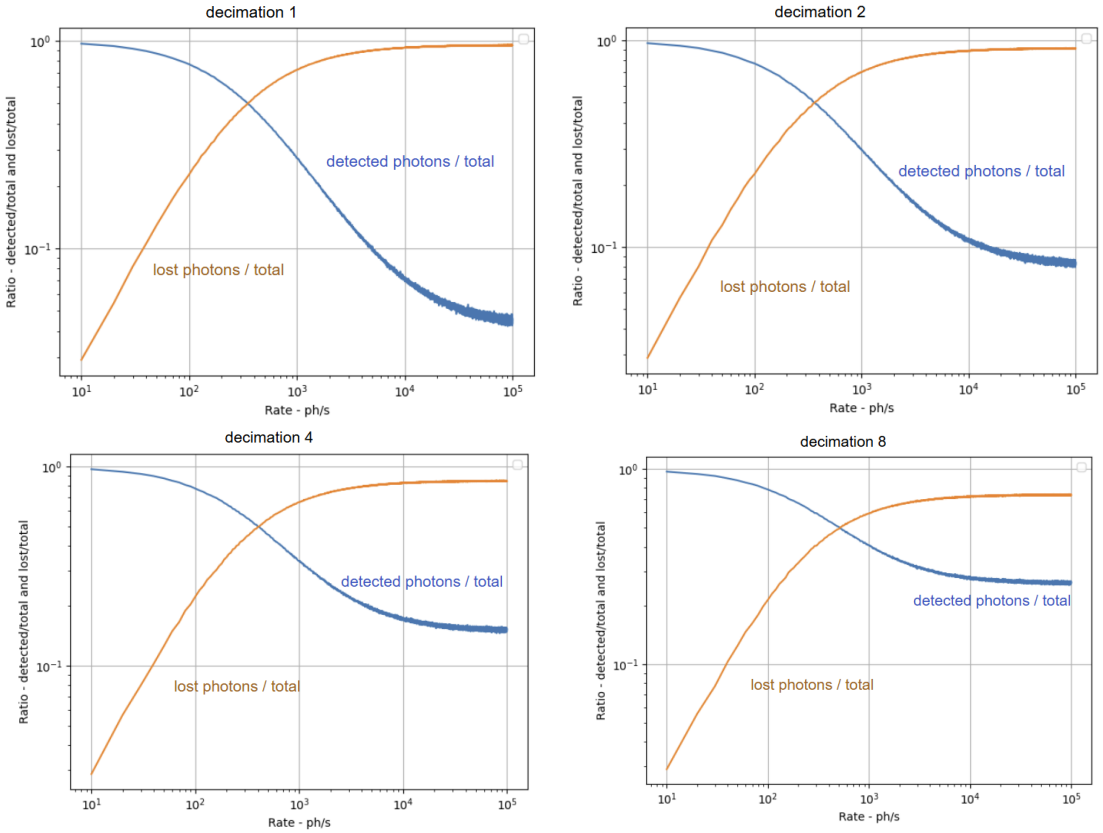

Figure 3.11: Outcomes of the first group of simulations for each of the four decimation factors chosen (1, 2, 4 and 8). An important aspect can be noticed: increasing the decimation factor and thus the duration of the acquisition window, the number of detected photons increases accordingly.

TGFs are extremely short transient events, with typical durations of ∼100 microseconds, and in several cases well below 1 millisecond. Consequently, the acquisition system must be capable of detecting consecutive photon arrivals separated by only a few microseconds, typically in the range of 1 – 10 μs, to properly sample the intrinsic temporal structure of these events.

On the other side, GRBs evolve over significantly longer timescales which varies from ∼0.1 seconds (short GRBs) to several tens of seconds (long GRBs). Thus, the

timing requirements for GRB detection are less stringent than for TGFs.

Therefore, a microsecond-level timing capability is beneficial for detailed temporal studies of both events. An evaluation of the capability of Gamma-Flash type I setup regarding the time separation between events was carried out through simulations. Indeed, the goal was to analyze the distribution of time intervals between two consecutive detected photons. The photon rate was fixed to 1000 photons/s, and each simulation covered a duration of 100 s, repeated for all four selected decimation factors (1, 2, 4, and 8). It is important to remember that each acquisition configuration includes a dead time of 3 ms following every open time window of 16384 samples, and this dead time is independent of the chosen decimation factor. This intrinsic dead time reduces the total number of detectable photons and, more critically, can limit the ability to capture physical events characterized by specific temporal signatures. The results obtained, whose exponential shape is due to the Poissonian statistics, are shown in Fig. 3.12 for the different decimation factors.

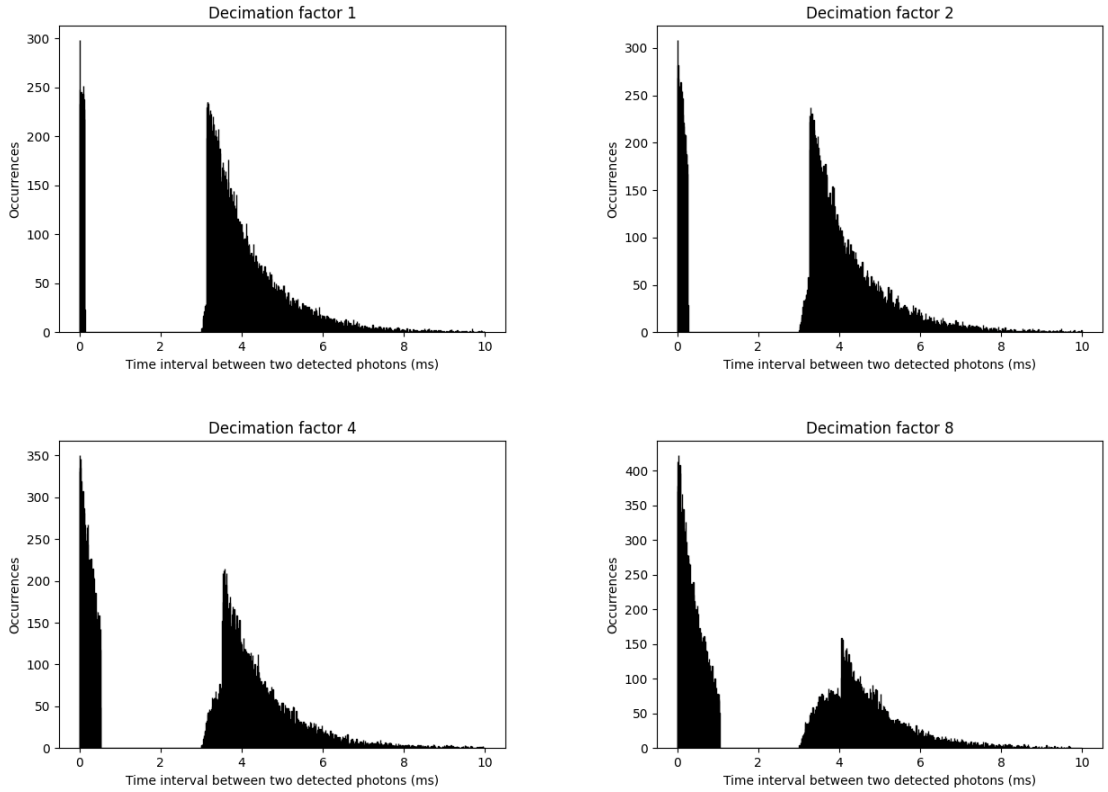

Figure 3.12: *Top images, from left to right*: Results of the second group of simulations for decimation factors 1 and 2. *Bottom image, from left to right*: outcomes of the second group of simulations for decimation factors 4 and 8. The same result previously obtained from the first group of simulations is confirmed. Furthermore, the gap in detection produced by system's dead time becomes shorter by increasing the decimation factor, leading to a smaller effective dead time.

In the four figures shown in Fig. 3.12, it is possible to observe comparable features. First, each plot shows a rising structure on the left side that becomes more pronounced as the decimation factor increases. This interval corresponds to the photons detected within the trigger window, which ranges from 131 μs for decimation 1 up to 1049 ms for decimation 8. A larger trigger window naturally results in a longer integration time and a higher number of collected photons.

On the other side, each figure shows a gap in detection, which is produced by the system's dead time after an acquisition cycle is completed. Notably, as the decimation factor increases, this gap becomes shorter, leading to an effective dead time that is shorter than the dead time duration for a single window. This effect is particularly evident for decimation 8, where the observed gap is less than 2 ms, compared to the nominal 3 ms.

The simulations showed that the best value for the decimation parameter is 8, so this value was chosen for all detectors. With decimation factor of 8, the system still uses 16384 sampling points, but the spacing between samples remains small enough to accurately reconstruct each event. At the same time, the longer acquisition window reduces the dead time and allows more photons to be detected. Thus, decimation factor of 8 provides the best balance between time resolution and event statistics.

After choosing this value, all the acquisition optimizations for the type-I Gamma-Flash detectors were completed. This also allowed the final file structure and acquisition scripts to be updated. The resulting improvements in data analysis are presented in Section Subsec. 3.5.1.

3.4.2 Gamma-Flash type II - configuration tests

In this section, the activities performed to configure the Gamma-Flash type II detectors, which were described in Subsec. 3.3.1, are reported. As a first step, it was essential to ensure that the detectors produced consistent and comparable results. In particular, their response to a given gamma-ray source should be similar, with spectral features appearing at approximately the same channel positions. To achieve this uniformity, an equalization process was carried out for all four detectors. This was done by adjusting the high voltage supplied to each photomultiplier tube (PMT), thereby modifying its gain and shifting the channel at which events of a given energy are recorded. For reference, we used the environmental emission line of ^{40}K, a naturally occurring radioactive isotope on Earth. This line has an energy of 1461 keV and appeared at approximately channel 380 in *gammaflash2a*. Therefore, it was established the goal of placing this feature around channel $\sim$ 400 for all detectors, given that precise spectroscopy is not required for our purposes. The other detectors (*gammaflash2b*, *gammaflash2c*, and *gammaflash2d*) already exhibited the ^{40}K line at channels 410, 410 and 425, respectively. Since these values are sufficiently close to the target region, no further voltage adjustments were applied. As a result, all detectors display consistent spectral features at comparable channel positions, fulfilling the equalization requirement.

Afterwards, calibration was performed for every detector, in order to find the relation between channels and energies. For this purpose, the formula considered is the following one:

$$\text{Energy} = A \cdot \text{Channel} + B \tag{3.4}$$

where A and B represent the slope and the intercept of the calibration line, which were obtained along with their related errors considering the ordinary linear regression formulas. Two sources were used to calibrate the spectra of the detectors: ^{137}Cs and ^{22}Na. The ^{137}Cs source has a photopeak at 661.7 keV. The ^{22}Na source presents two photopeaks, one at 511 keV and the other at 1275 keV. An acquisition of 120 s was carried out for each source with each detector. The channels obtained, which are related to specific lines with their known energies, are reported in Tab. 3.2 for *gammaflash2a*, *gammaflash2b*, *gammaflash2c* and *gammaflash2d*.

Detector *gammaflash2a*		
Element	**Energy**	**Channel**
^{22}Na	511 keV	125±5
^{137}Cs	661.7 keV	166±5
^{22}Na	1275 keV	330±5

Detector *gammaflash2b*		
Element	**Energy**	**Channel**
^{22}Na	511 keV	132±5
^{137}Cs	661.7 keV	193±5
^{22}Na	1275 keV	376±5

Detector *gammaflash2c*		
Element	**Energy**	**Channel**
^{22}Na	511 keV	135±5
^{137}Cs	661.7 keV	187±5
^{22}Na	1275 keV	384±5

Detector *gammaflash2d*		
Element	**Energy**	**Channel**
^{22}Na	511 keV	112±5
^{137}Cs	661.7 keV	180±5
^{22}Na	1275 keV	338±5

Table 3.2: *Top tables, from left to right*: Calibration sources and points (energies and channels) used for detectors *gammaflash2a* and *gammaflash2b*. *Bottom tables, from left to right*: calibration sources and points (energies and channels) used for detectors *gammaflash2c* and *gammaflash2d*.

The slopes and the intercepts obtained are: A=3.7±0.01 and B=43.7±2.4 for *gammaflash2a*, A=3.2±0.2 and B=72.4±45.0 for *gammaflash2b*, A=3.1±0.1 and B=90.9±9.5 for *gammaflash2c* and A=3.5±0.4 and B=87.4±88.5 for *gammaflash2d*. Therefore, these calibrations can be used to visualize the x-axis of the spectra in energies and not in channels, when needed.

Isotropy tests were carried out for one detector (*gammaflash2a*) to check its response in detecting events depending on their direction of arrival. For this purpose, a collimator with the ^{137}Cs source was used, considering three different configurations that are described below.

- In the *long side* configuration the collimator with the source was placed and centered in the direction parallel to the long side of the detector;
- in the *short side* configuration the collimator with the source was placed and centered in the direction parallel to the short side of the detector;
- in the *face-on* configuration the collimator with the source was placed and centered face-on with respect to the detector.

These three configurations are represented in Fig. 3.13. The acquisition time for every configuration was of 300 s and the related spectra obtained are reported in Fig. 3.14.

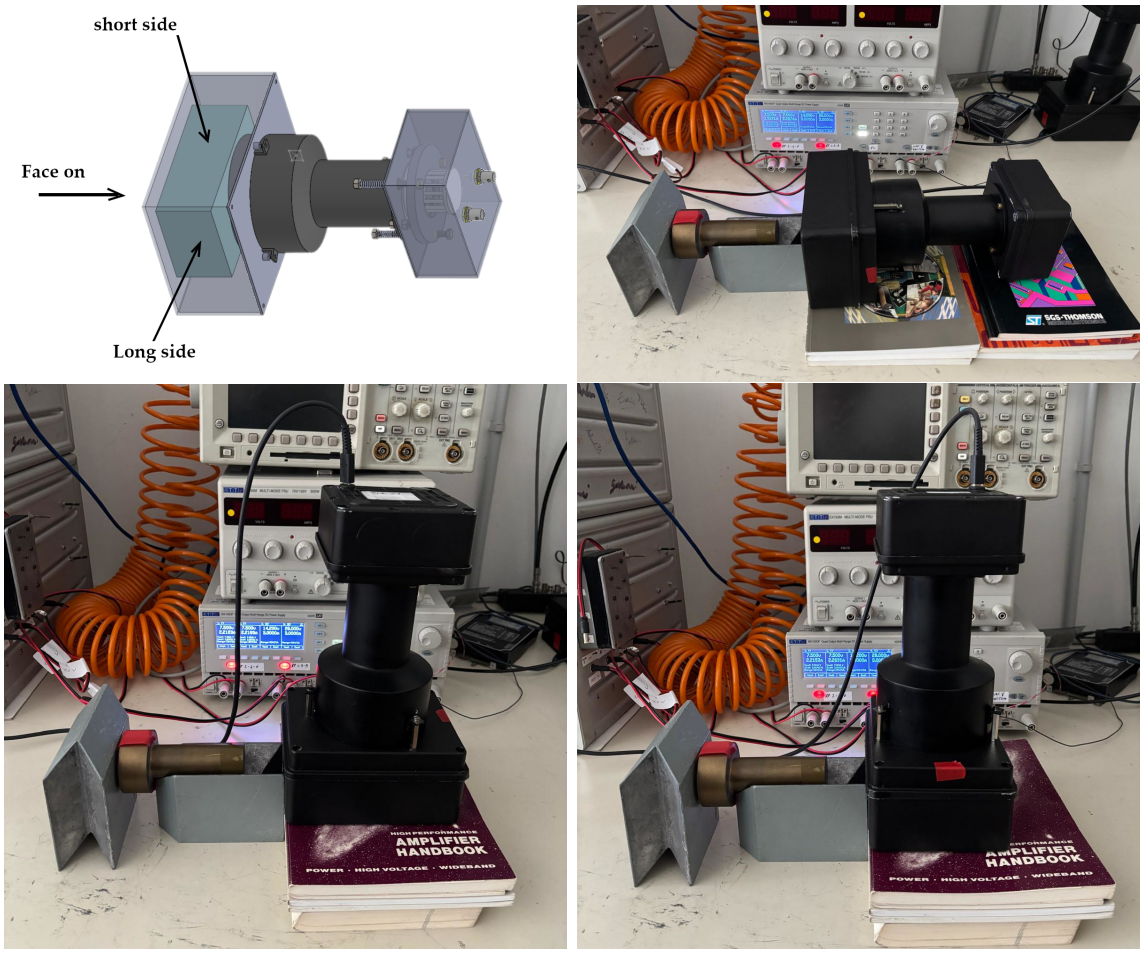

Figure 3.13: *Top images, from left to right:*: Sketch showing the three illumination configurations and *face-on* configuration. *Bottom images, from left to right*: *long side* configuration and *short side* configuration.

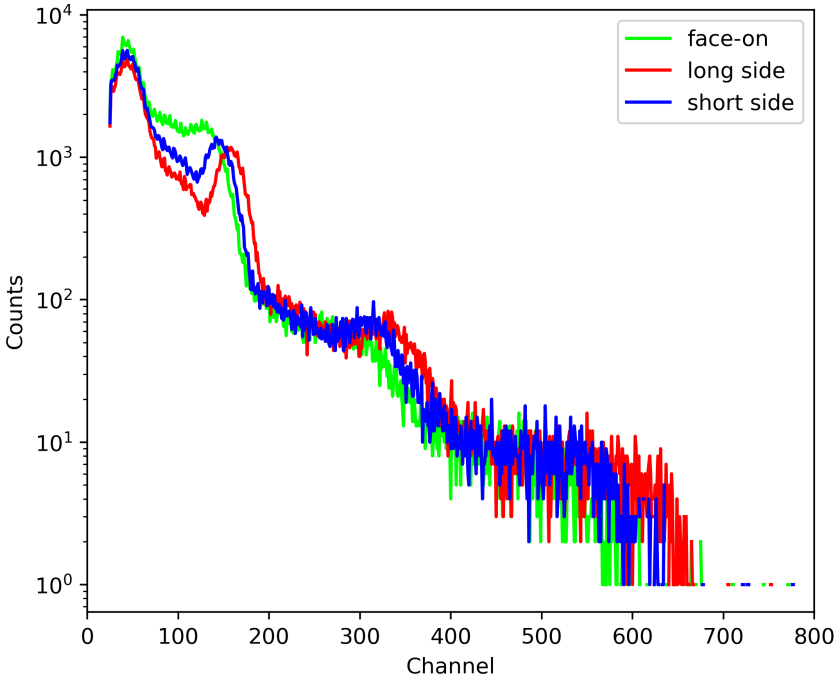

Figure 3.14: *face-on*, *long side* and *short side* configurations for *gammaflash2a* detector with ^{137}Cs source, each with 300 s acquisition.

From the spectra of *gammaflash2a* shown in Fig. 3.14, it is evident that the *face-on* configuration yields the highest count rate among the three orientations. This behavior is consistent with the shorter and more direct photon path toward the photomultiplier tube (PMT) in this configuration, which increases the probability of photon detection.

Between the remaining two geometries, the *short-side* configuration exhibits a higher number of counts than the *long-side* one. This can again be attributed to the reduced photon path length in the *short-side* configuration, which enhances the likelihood that photons reach the PMT before being absorbed or scattered. Additionally, a relative shift is observed among the spectra corresponding to the three configurations. This effect is unexpected, as a similar shift is also present for the ^{40}K environmental line, despite being part of the background. This indicates that the spectral position depends on which face of the scintillator is illuminated. Possible explanations include small non-uniformities in the scintillation crystal or slight irregularities in the coupling between the crystal and the PMT. Although, high-precision spectroscopy is not required for the purposes of this project; nonetheless, these results provide useful insight into potential systematic effects.

Afterwards, the focus was shifted to the optimization of the acquisition boards of

the detectors. Each detected event produces a signal in the detector whose shape is a fast rise (order of 50 ns) and an exponential decay (decay time of the order of 600 - 900 ns for the fast component and a slower decay of the order of 3.5 ms). An example of the shape of one detected photon by one of these detectors is shown in Fig. 3.15. From the signal we extract the main information related to the incident photon (energy, time of arrival). With this specific acquisition board, it is possible to tune two specific parameters: so called shaping time (τ) and the low energy threshold (E_{min}).

The tuning was performed with one board connected with one detector and the obtained optimized parameters were applied equivalently to the other detectors, as they are identical.

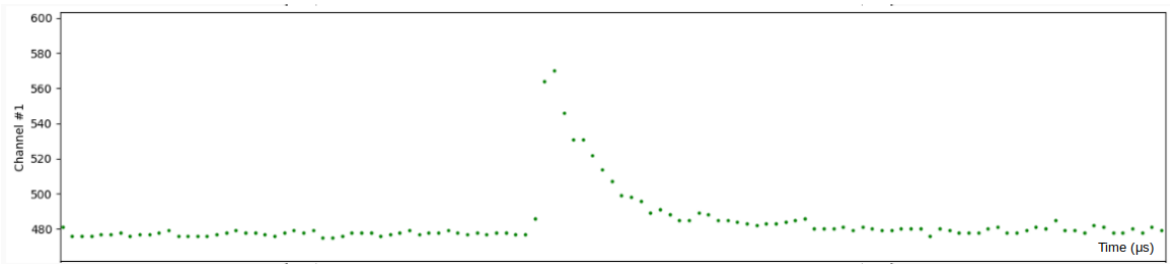

Figure 3.15: Example of an event detected by one of the four Gamma-Flash type II detectors.

The τ parameter represents the sum of the collection time to integrate all the optical photons produced by the scintillator when hit by a gamma-ray photon, plus the time required by the electronic board to process the signal. The optimal value for the τ parameter mainly depends on the scintillator type and on the system geometry. Our goal is to optimize this parameter in order to maximize the detected gamma-ray photons.

Several acquisition have been made by changing the τ parameter and obtaining the associated total detected photons. Two different configurations with ^{137}Cs as source were considered:

- in the *far configuration*: the collimator with the source was placed face-on at a distance of 42 cm with respect to the detector;
- in the *close configuration*: the collimator with the source was placed in contact to the detector.

For each of these two configurations, ten different τ values have been considered, modifying the variable from $\tau = 4$ to $\tau = 8$ in step of 0.5. For each τ value, an acquisition of 120 s was performed. The setups described are reported in Fig. 3.16. The plots with the results obtained are shown in Fig. 3.17.

Figure 3.16: *Left image*: *distant* configuration. *Right image*: *near* configuration.

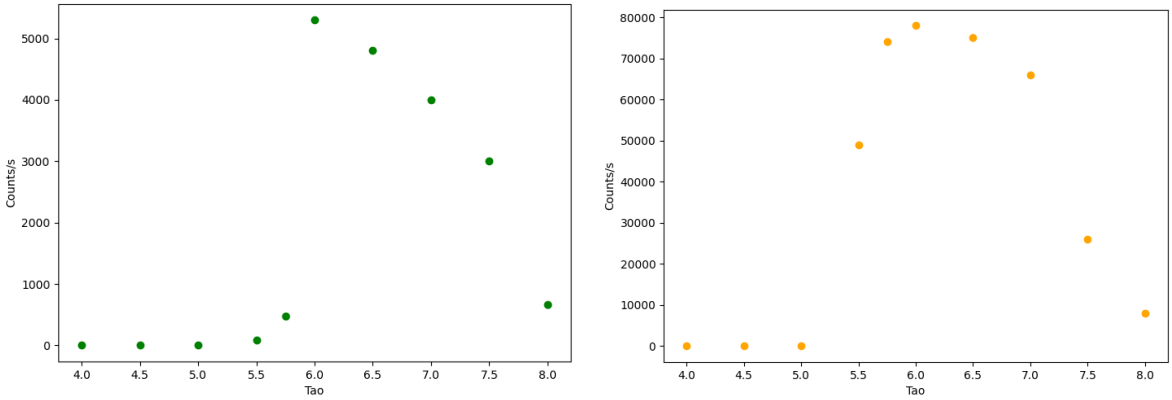

Figure 3.17: *Left image*: *distant* configuration with ^{137}Cs source, with 120 s acquisition for each τ value. *Right image*: *near* configuration with ^{137}Cs source, with 120 s acquisition for each τ value.

As a function of the shaping time, for τ a peculiar behavior can be observed in both far and close configuration. From almost zero photons detected at τ less than 5, the number of counts rapidly increases from 5.5 to 7.5, then the counts decreases again quickly to zero for $\tau > 8$. The two configurations exhibits similar behavior, even if in *distant* configuration the shape of the curve looks more asymmetric than that for *near* configuration. In the *distant* configuration, the count rate related to every acquisition is lower with respect to that of the *near* configuration. This is simply explained by the different position of the ^{137}Cs source in the *distant* setup: it is more distant with respect to the detector face than in the other configuration, thus its count rate is smaller. This behavior can be explained by considering the relationship between the scintillation decay time of the crystal and the shaping (integration) time of the electronics. If the shaping time is shorter than the scintillation time, the electronics integrate only a fraction of the scintillation light. As a result, each gamma-ray interaction produces a pulse with reduced amplitude, because fewer optical photons are effectively collected. When the shaping time is too short, some pulses may fall below the discriminator threshold, and those events are therefore not detected, even though they occurred in

the scintillator.

As the shaping time increases and becomes comparable to, or longer than, the scintillation decay time, the electronics collect most or all of the optical photons generated by a gamma-ray interaction. In this regime, the pulse amplitude is sufficient to exceed the threshold, and the detection efficiency reaches its maximum. However, if the shaping time becomes too long, the output pulses broaden significantly. In this condition, two or more gamma-ray events may occur within the same effective integration window. Their pulses then overlap, causing pile-up, which reduces the number of events that can be individually recognized. This leads to an apparent decrease in the measured count rate, even though the true interaction rate in the crystal remains unchanged. The maximum observed count rate occurs around a shaping time of approximately $\tau = 6$ in all configurations. For this reason, this value was adopted as the optimal shaping parameter for all four detectors.

The second parameter that was tuned was the one related to the lower energy threshold. It was set at 400 keV, as a trade off between keeping the threshold high enough to reduce background photons but, at the same time, to have the possibility to monitor the important 511 keV line. The link between TGFs and 511 keV comes from the fact that TGFs are energetic enough to produce electron–positron pairs in the atmosphere. The bremsstrahlung photons generated by the relativistic electrons in a TGF can reach MeV energies. If the energy exceeds 1.022 MeV, annihilation radiation at 511 keV can be observed. Because of this, TGFs can be indirectly associated with the 511 keV annihilation line, even though the TGFs themselves do not intrinsically emit radiation at exactly this energy. Therefore, the 511 keV feature is a signature of the extreme conditions created by TGFs.

The *peak_threshold* channel needed to be evaluated in order to set the associated energy threshold. In particular, the channel related to the energy of 400 keV was obtained with the calibration through known radioisotopes. Therefore, the calibration previously described was used to find the channel related to the energy value chosen. The calibration lines, along with the channel obtained are depicted in Fig. 3.18. Using these calibration lines, the channel related to the minimum energy value chosen of 400 keV was obtained, as previously stated. It was around channel 96 for all the four detectors. Thus, the parameters *peak_height_min* and *peak_threshold*, which needed to be fixed in the same way, were both set to 96. Therefore, this parameter value was applied to all the four detectors.

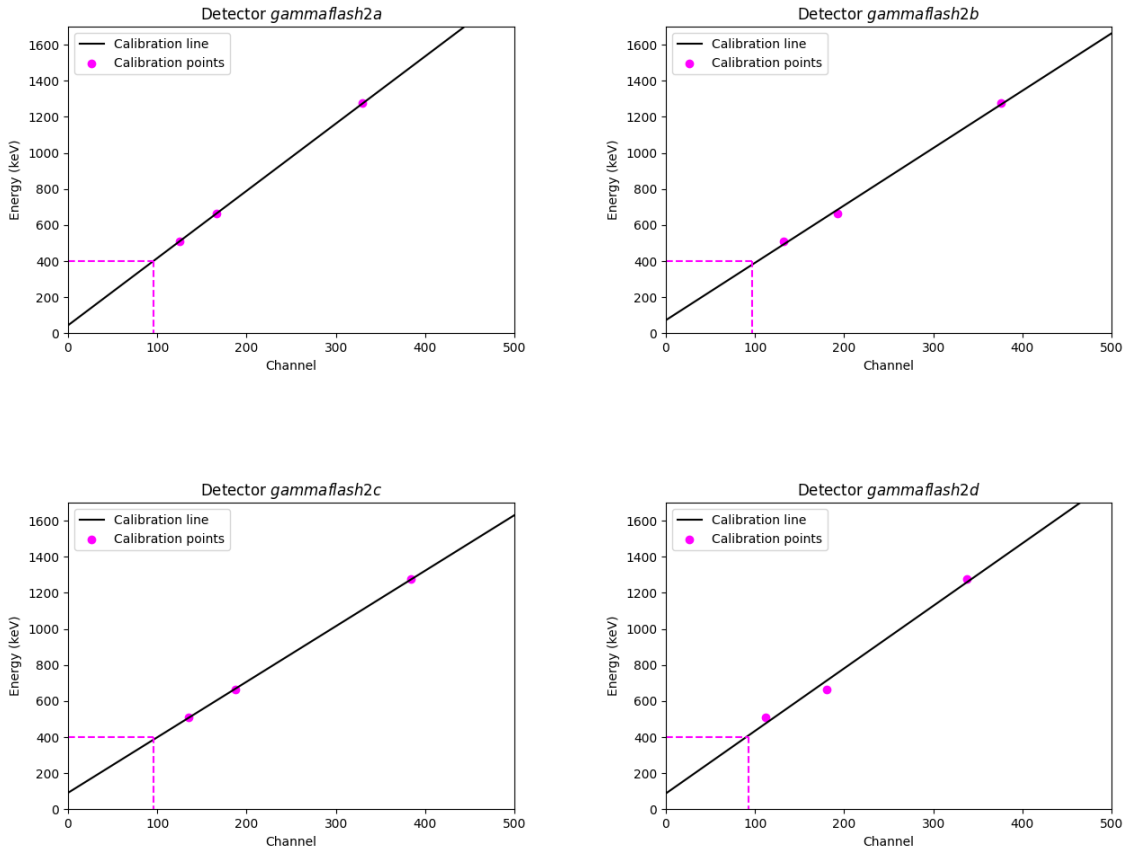

Figure 3.18: *Top images, from left to right*: Calibration lines obtained plotted along with points used for calibration for detectors *gammaflash2a* and *gammaflash2b*, which are listed in Tab. 3.2. *Bottom images, from left to right*: calibration lines obtained plotted along with points used for calibration for detectors *gammaflash2c* and *gammaflash2d*, which are listed in Tab. 3.2. In general, dashed magenta lines allow to visualize the channel related to the minimum energy threshold chosen (400 keV), which is around 96 for all the four detectors.

Thereafter, the detectors characterization was performed to investigate their saturation behavior. In particular, also in this case the test was carried out just for *gammaflash2a*, since the other three detectors are the same. A configuration that allowed to have the highest possible number of counts in the laboratory was set, in order to check for possible saturation. The *gammaflash2a* detector and two radioactive sources ^{137}Cs and ^{22}Na were used for this purpose. At the beginning, ^{137}Cs was the only source used and it was placed below the detector between two lead blocks as in Fig. 3.19.

In this case, no saturation was present, but by removing the lead blocks the saturation was reached, since the detector in this way can intercept a larger solid angle of (isotropic) source photon emission, and thus the count rate increases. Afterwards, starting again with the configuration as in Fig. 3.19, but this time considering also

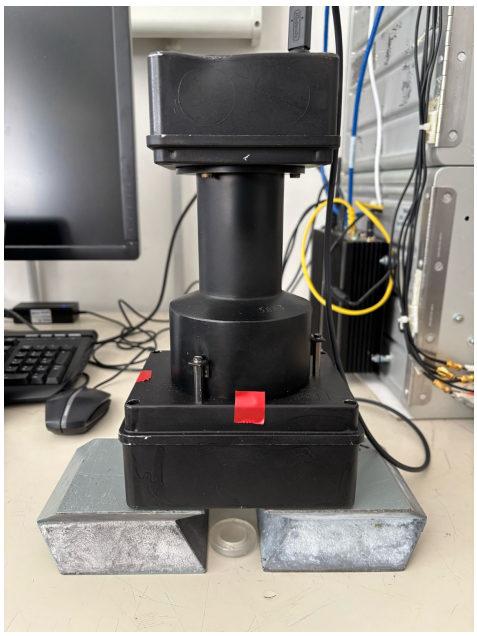

Figure 3.19: Initial configuration adopted for saturation test with one of the four Gamma-Flash detectors with new configuration and the ^{137}Cs source placed in between two lead blocks.

^{22}Na, other results were obtained. The ^{22}Na source was progressively moved near the ^{137}Cs source and the number of counts started to increase, until the moment the two sources were both below the detector and saturation was reached again. This happened around 80000 counts/s. At this stage, an estimation of the expected count rate for an average TGF detected from ground was made, in order to compare the expected counts/s with the saturation value obtained. However, TGFs detection from ground are not so many, therefore estimating this value is not an easy task. Several variables needs to taken into account, such as the distance and the height of the TGF origin, the kind of detector, its area and energy range. Thus, three papers related to TGFs detected from ground were selected to perform this estimation: Wada 2019, Hisadomi 2021 and Smith 2011. Considering some of the variables just mentioned that are present in these papers, an estimation of the expected count rate for an average TGF detected from ground by Gamma-Flash detectors was obtained. The results from the papers are reported in Tab. 3.3, and they were scaled for a detector with the same area of type II Gamma-Flash detectors (96 cm^2).

Hence, the derived value for the expected TGF count rate from ground was 10^4 counts/s. This is a high number, but is of the same order of magnitude of the saturation value previously reported (80000 counts/s). These results show that the detectors are able to handle the TGFs high count rates.

Paper	Detector	Area	Energies	TGF distances	Counts/s
Wada	$Bi_4Ge_3O_{12}$	200 cm^2	0.4-20 MeV	L=0.5 km H=500 m	40000
Hisadomi	$Bi_4Ge_3O_{12}$	200 cm^2	3-20 MeV	L=2 km H=1 km	5500
Smith	Plastic	322 cm^2	0.3-5 MeV	L=5 km H=14 km	200000

Table 3.3: Kind of detector, detector area, energy range of the acquisitions, TGF distances from detector (L=radial distance and H=height) and counts/s, taken from related papers.

3.5 Data analysis

All the activities described in Sec. 3.4 were carried out in order to optimize the acquisition process. After all the optimizations were applied, the final adjustments related to the definitive structure of the files and the acquisition scripts were implemented, in order to proceed with data collection and analysis. Each setup previously described relies on a different file format and structure. For this reason, the corresponding formats, along with the subsequent scripts and activities related to the data analysis part, are reported in this section for each setup. Specifically, the aspects related to the Gamma-Flash type I configuration setup are addressed in Subsec. 3.5.1, those regarding the Gamma-Flash type II configuration are in Subsec. 3.5.2 and the PIZ-Gamma setup is examined in Subsec. 3.5.3.

3.5.1 Gamma-Flash type I configuration: files and data analysis

In the case of the Gamma-Flash type I configuration, a number of final adjustments were implemented in the acquisition script associated with the Red Pitaya STEMlab 125–14 boards. For the four detectors (*gammaflash1a*, *gammaflash1b*, *gammaflash1c*, and *gammaflash1d*), the script was configured to allow the selection of any single detector, any combination of detectors, or all of them simultaneously, enabling concurrent acquisitions. The acquired data are stored in HDF5 files, each containing a fixed set of 1000 waveforms. Each waveform represents a single event and corresponds to one acquisition window, chosen as described in Subsec. 3.4.1. Each HDF5 file is then reprocessed by fitting the peak (or peaks) detected in each waveform to determine its maximum amplitude, which is directly related to the event energy, as discussed in Subsec. 3.4.1. This reprocessing is performed automatically by a Python script executed daily at midnight, using crontab on the computer. The script converts each HDF5 file into a text file containing the peak amplitude and the event timestamp, recorded with microsecond precision. As a result, a set of text files is produced, each providing the relevant single-event information for a corresponding detector.

These text files are then used for the data analysis. A dedicated, ready-to-use Python script allows the production of both light curves and spectra. Light curves

are displayed as event counts normalized over a selected time interval and plotted as a function of time, while spectra are shown as the number of counts as a function of the detector channels.

3.5.2 Gamma-Flash type II configuration: files and data analysis

In the case of the Gamma-Flash type II configuration, some modifications were applied to the acquisition script provided with the FBK boards, in order to make the output file structure as consistent as possible with the other setups. Considering that there are four Gamma-Flash detectors with the type II configuration, namely *gammaflash2a*, *gammaflash2b*, *gammaflash2c* and *gammaflash2d*, a Python script was structured in order to obtain acquisitions from one or more detectors, or simultaneous acquisitions from all of them. Generally, the acquisition was set in order to produce a new binary file every 24 hours (this can be set differently if needed) with the structure described below. The generated binary files contain in each row information about a single event registered by the detector: timestamp of the event, its peak amplitude and the ambient temperature around the board. The timestamp is registered with microsecond precision and it represents the time elapsed from the midnight of the day in which the acquisition was launched. The amplitude of the event is expressed in channels and related to the energy of the event by the Eq. 3.4 explained in Subsec. 3.4.2. The ambient temperature around the board is monitored since it can affects the measurements and it can also be compared with the temperature registered by the weather station inside the dome where the setup is placed to check for consistency. Furthermore, a triggering algorithm was implemented in the acquisition script. In particular, a reference background was set for each binary file by evaluating the average count rate of the events recorded in the first seconds of that file (the number of seconds can be set when launching the script). This background rate was compared with the number of counts in each bin of a given duration: when the count rate for a specific bin exceeds the background level by more than a specified number of sigma, this triggers an alert which is saved in the acquisition log file. Therefore, the acquisition script produces a binary file with a chosen duration for each detector and automatically scan them with the triggering algorithm to search and identify possible high-energy transient phenomena.

Two Python scripts were developed in order to analyze the event files obtained from the acquisitions. One allows to generate light curves and the other to the production of spectra. For the light curves, the time duration of each bin can be set and the counts per bin are plotted against time. The light curve can be integrated over the whole energy pass-band or, alternatively can be made by selecting a specific energy pass-band (energy-resolved light curve). Furthermore, it is possible to set the energy bins before plotting the counts per bin as a function of channels. It is also possible to select the time interval over which the spectrum is integrated, making it time-resolved. For the conversion of energies in channels and vice-versa the Eq. 3.4 was used with the

relations obtained for the detectors in Subsec. 3.4.2.

3.5.3 PIZ-Gamma: files and data analysis

For the PIZ-Gamma setup, the acquisition script was ready-to-use. It was set in order to have simultaneous acquisition related to both PIZ-Gamma detectors (*pizgamma1* and *pizgamma2*). Furthermore, each day of acquisition, a binary file was produced with information about time and amplitude for each event.

The files obtained were examined with the same two Python scripts used for the analysis of the Gamma-Flash type II configuration files, which are described in Subsec. 3.5.2. This was possible because both setups use FBK acquisition boards, therefore producing compatible data formats. Thus, light curves are shown considering counts per bin as a function of time: since the exact conversion between energies and channels for this setup is not known, we cannot obtain in this case energy-resolved light curves. On the other hand, spectra are plotted as counts against channels and are time-resolved.

3.6 First results

The results obtained from Mt. Cimone and Mt. Piz Boè data, which were obtained using the data analysis pipeline described in Sec. 3.5, are shown in the following. In particular, this section first provides a general overview of the monitoring results for the two sites, taking into account the different instruments in the setups and their related data. Afterwards, the detections of some specific high-energy atmospheric transient phenomena are presented.

3.6.1 Monitoring results

In general, when dealing with complex setups such as Gamma-Flash and PIZ-Gamma, it is fundamental to verify the correct functioning of each instrument and to identify potential failures or external factors that may affect acquisition and analysis. Among these external factors are some issues related to the specific experimental sites, described in Sec. 3.2, which can influence the measurements. One of the difficulties always presents when investigating high-energy atmospheric transient phenomena from ground is related to the absorbing column of air between ground and high-field regions of storms (at several km of altitude). This issue can be partially solved by the choice of the experimental site locations, as previously stated. The other problem related to the investigation of this kind of events is linked to the high-energy emissions due to the decay chain of radon washed out by rain. The latter was observed when analyzing Gamma-Flash and PIZ-Gamma data. Some of these results are shown in the following.

Radon washout was observed several times in Gamma-Flash data. In particular, we chose to focus in this section on a specific period of time between July 4th and July 7th 2025, which showed a high concentration of these events. The radon washout events within this time range were identified studying the light curve and the spectrum obtained. From the light curve, it was possible to identify six increments in the gamma-ray counts that were associated to radon washout events, always corresponding to rainfall periods. In chronological order, they lasted respectively 175, 200, 110, 140, 170 and 100 minutes: these durations cannot be associated with events such as TGFs or gamma-ray glows, further supporting the radon washout origin. These events are shown in the energy-integrated light curve in Fig. 3.20, derived from the *gammaflash2a* data. Considering the time-integrated spectrum of the same period, shown in Fig. 3.21 for the *gammaflash2a* detector, no features related to the radon washout events can be observed. Therefore, a further analysis was carried out. Both the light curve and the spectrum are reported just for the *gammaflash2a* detector, since data from other detectors showed the same results.

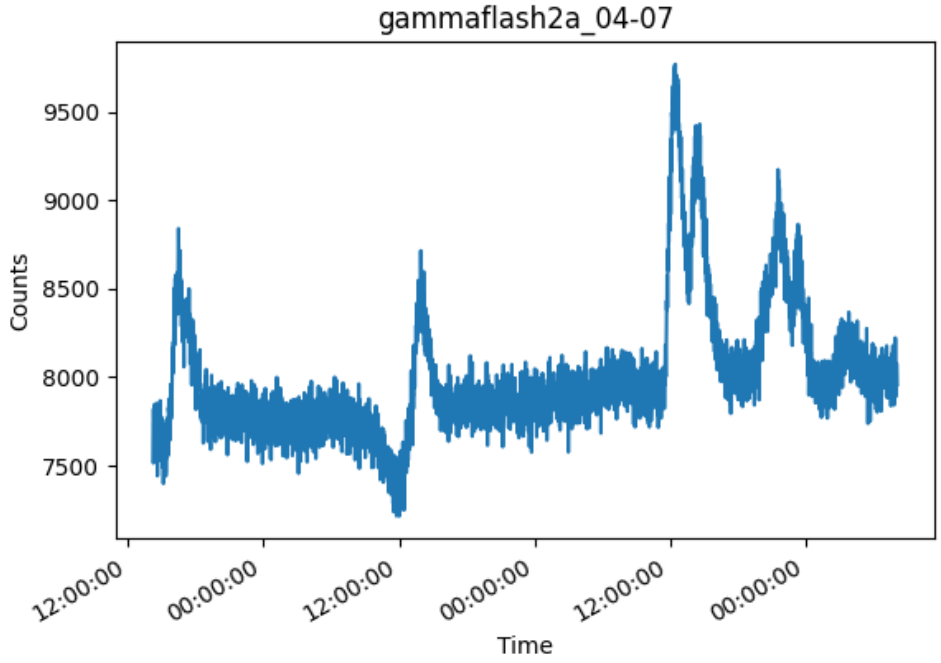

Figure 3.20: Energy-integrated light curve of *gammaflash2a* detector with temporal bins of 1 minute. The period considered extends from July 4th to July 7th, 2025. Six radon washout events can be identified due to the sharp increase in counts and their durations of the order of hours.

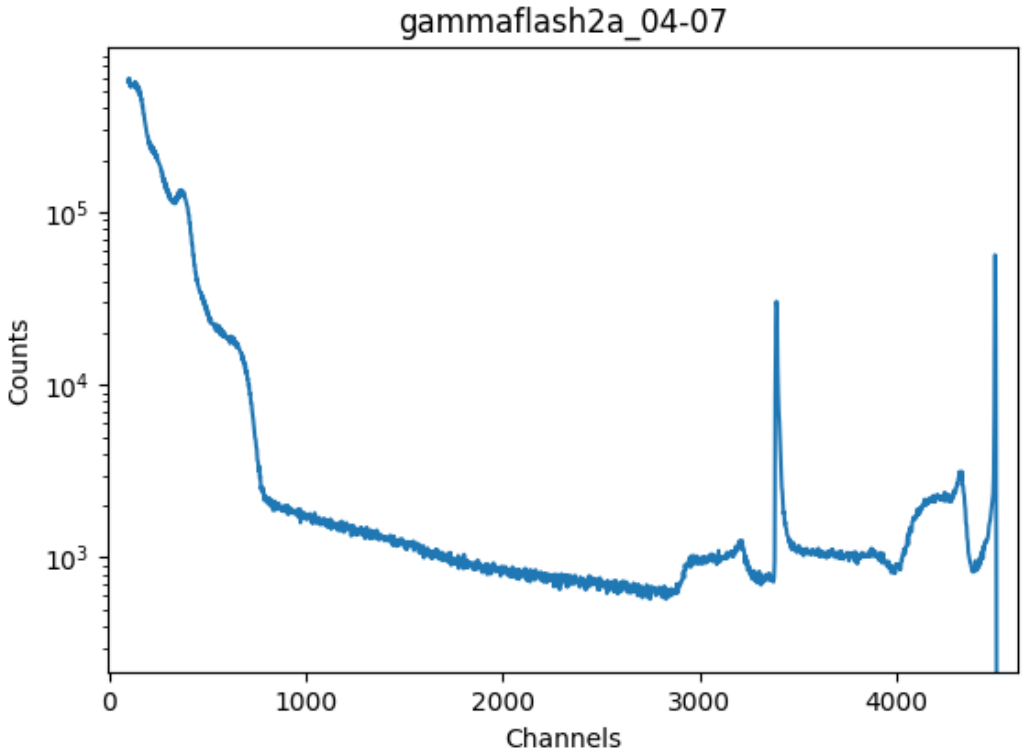

Figure 3.21: Time-integrated spectrum of *gammaflash2a* detector,integrated over the same period considered in the light curve (July 4th–7th, 2025). Specifically, counts are plotted as a function of channels. No radon washout features can be observed in this plot. Moreover, the features above channel 3000 are related to some spurious effects due to the electronics in the detector, because they can not be associated to any specific event and are observed in all the detectors.

To further analyze the time-integrated spectrum, the difference between the counts recorded during 100 minutes of radon-washout activity and those recorded during 100 minutes of background was computed for each of the six events, obtaining six new spectra. This comparison allows to enhance the spectral lines specific to the radon-washout spectrum, which are absent in the background. Only one of them is shown in Fig. 3.22, since the other five showed the same features. By examining this spectrum, three characteristic emission lines can be observed: they all originate from ^{214}Bi, a well-known daughter nucleus in the decay chain of radon. These lines, corresponding to the energies of 609 keV, 1420 keV and 1760 keV, are also highlighted in the spectrum in Fig. 3.22. Therefore, after analyzing both the light curves and the spectra of these six events, it was possible to classify them as radon-washout events, based on their durations and on the characteristic features observed in the spectra.

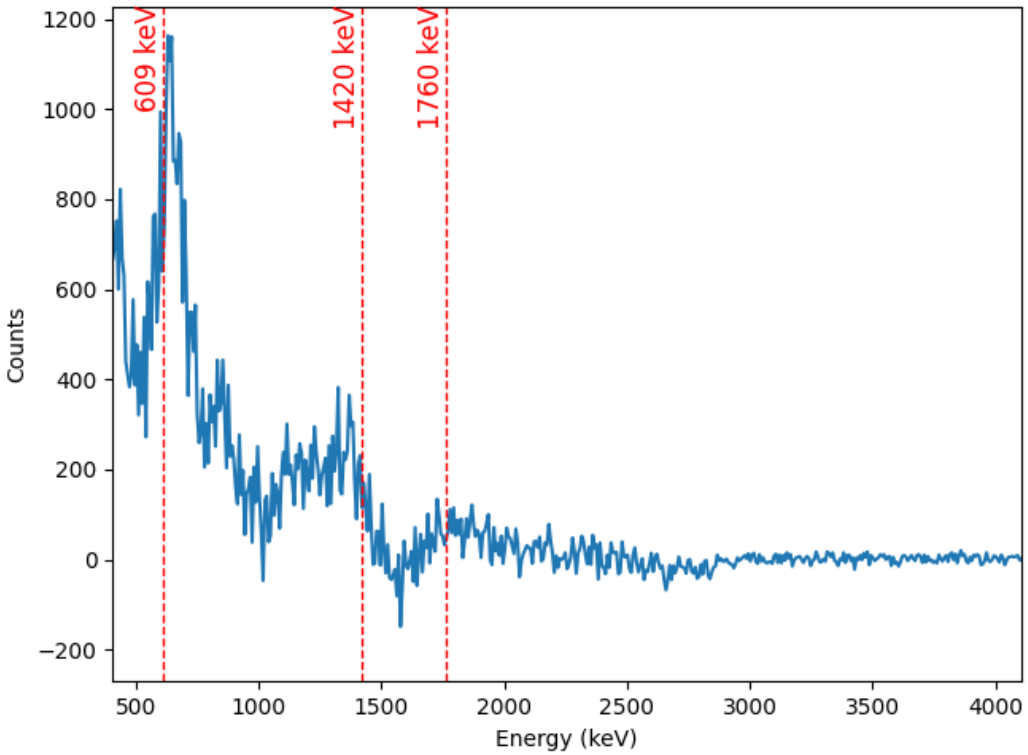

Figure 3.22: Energy-calibrated spectrum obtained considering the difference between the counts of 100 minutes of the sixth radon washout event in Fig. 3.20 and the ones related to 100 minutes of background. The red dashed lines represent the three ^{214}Bi lines along with their related known energies.

The setup temperature during the days of these events was also monitored. In particular, the temperature data collected by the Gamma-Flash type II detectors and those acquired by the weather station were checked and compared: they are shown, respectively, in Fig. 3.23 and in Fig. 3.24 as a function of time. Temperature values in the two cases show some differences. This is due to the fact that the measurements for the Gamma-Flash type II detectors are performed by a sensor directly integrated in the FBK board and refer to the temperature inside the detector housing, whereas the weather station is placed inside the dome but at some distance from the setup. Therefore, the detector temperatures are expected to be higher than those recorded by the weather station, as can indeed be observed in the plots. However, in both cases the overall time evolution of the temperature is the same and follows the normal day-night

cycle, with no specific or unexpected features.

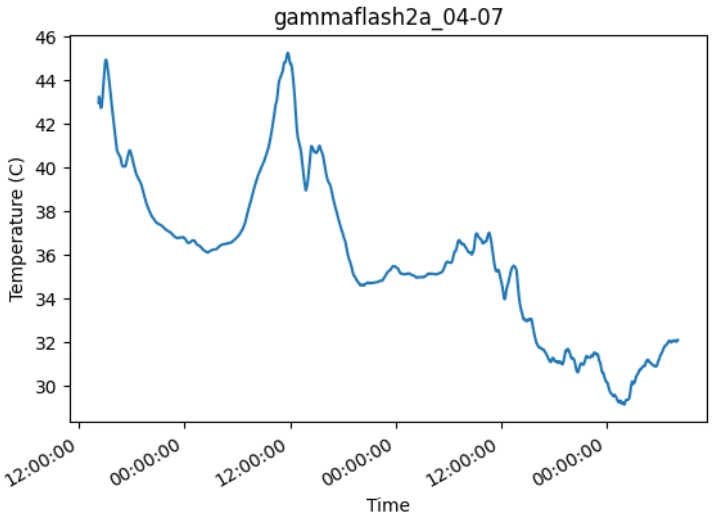

Figure 3.23: *gammaflash2a* plot of temperature as a function of time. From July 4th to July 7th 2025, the typical day-night cycle can be observed, with peaks occurring around midday.

Figure 3.24: Weather station plot of temperature as a function of time. From July 4th to July 7th 2025, the typical day-night cycle can be observed, with peaks occurring around midday.

Along with the six radon-washout events just discussed, several other similar events were also detected by the Gamma-Flash setup; however, only one additional case, which occurred on August 20th and lasted a couple of hours, is reported here. This event, which was not further analyzed, is reported in order to show the simultaneous and

consistent response of multiple high-energy Gamma-Flash detectors. Thus, only the light curves are shown, for four of the eight Gamma-Flash high-energy detectors, in Fig. 3.25. As expected, all the detectors recorded the same event.

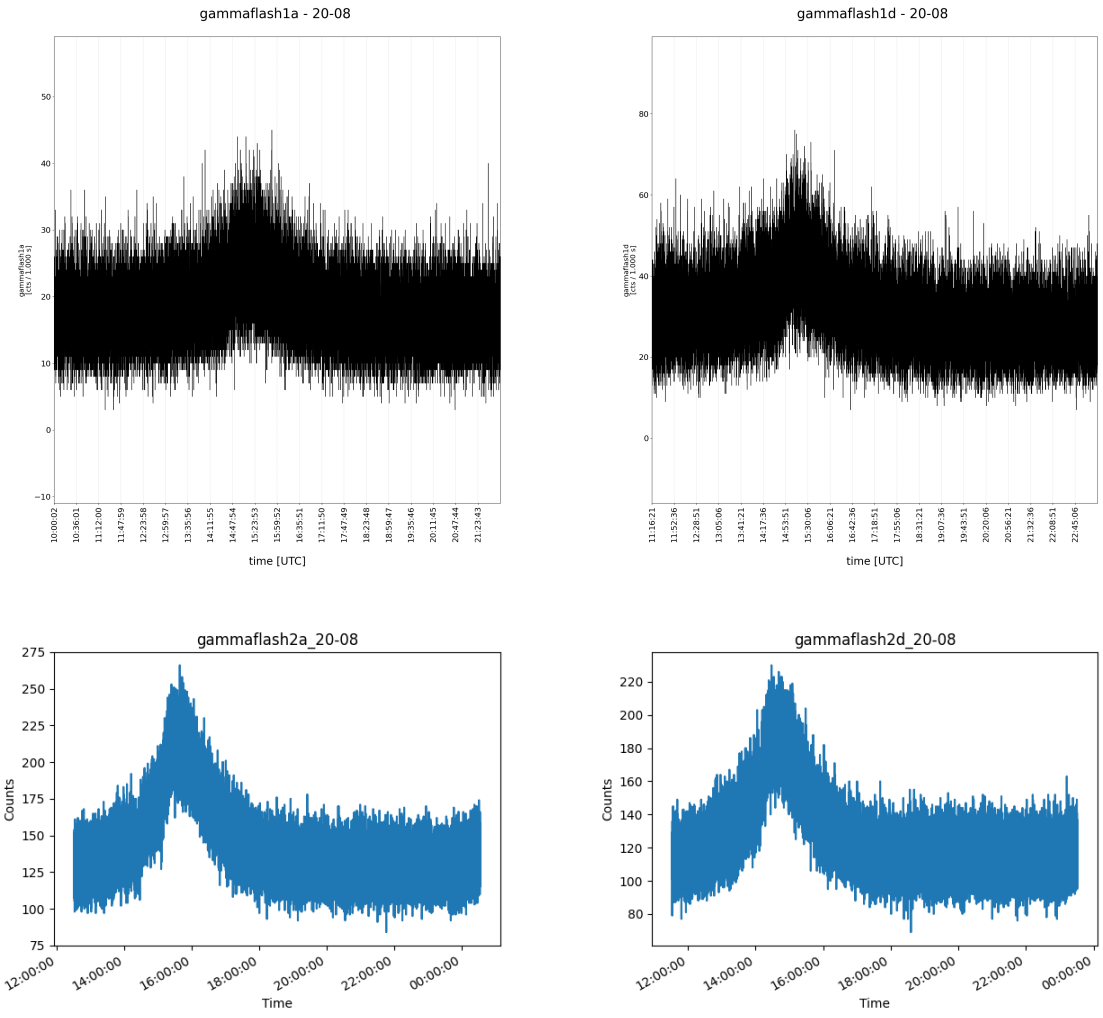

Figure 3.25: *Top images, from left to right*: *gammaflash1a* and *gammaflash1d* energy-integrated light curve. *Bottom images, from left to right*: *gammaflash2a* and *gammaflash2d* energy-integrated light curve. They are all referred to the August 20th 2025 radon washout event and have 1s temporal bin.

Regarding the PIZ-Gamma setup, it consists of only two high-energy detectors, as previously stated. Therefore, the corresponding light curves are shown in order to illustrate the monitoring performed at the Piz Boè site. In particular, two radon-washout events both lasting a couple of hours and occurring on August 29, 2025 appear in the

light curves of both detectors. The related plots are shown in Fig. 3.26: the events, which were not further analyzed, are included just to demonstrate that simultaneous acquisition worked correctly.

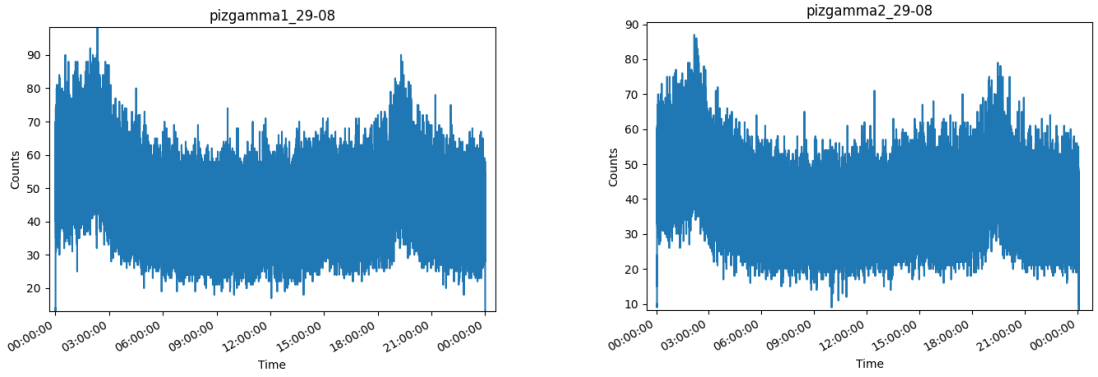

Figure 3.26: *Left image*: *pizgamma1* energy-integrated light curve. *Right image*: *pizgamma2* energy integrated light curve. They are both referred to August 29th 2025 and have 1 s temporal bin. Two radon washout events can be observed.

Thus, a general monitoring of the various setups was presented considering many aspects. In particular, a more in-depth analysis of some radon-washout events that happened during rainfall periods was carried out in order to show their main characteristics. Moreover, the functioning of the weather station was also checked by comparing its temperatures with the ones obtained with the *gammaflash2a* detector. Ultimately, the simultaneous acquisition of the different high-energy detectors was also monitored.

3.6.2 High-energy atmospheric transient phenomena results

After the monitoring of Gamma-Flash and PIZ-Gamma setups previously reported, high-energy atmospheric transient phenomena detected from both Mt. Cimone and Piz Boè sites are presented.

Regarding Mt. Cimone site, one gamma-ray glow was detected in the past by the Gamma-Flash setup in the original configuration and is presented in the following. Specifically, it was detected on April 24th 2023 during a thunderstorm and was studied in Calabretto (2025) by examining its light curve and spectrum, in order to assess its duration and spectral features. Its light curve is shown in Fig. 3.27 for the *gammaflash1a* detector: a gamma-ray glow lasting around one minute and a half is clearly revealed at around 12:13 UTC. Regarding its spectrum, is represented in Fig. 3.28: a substantial component above 2.6 MeV not compatible with the background is shown, confirming the origin of the phenomenon.

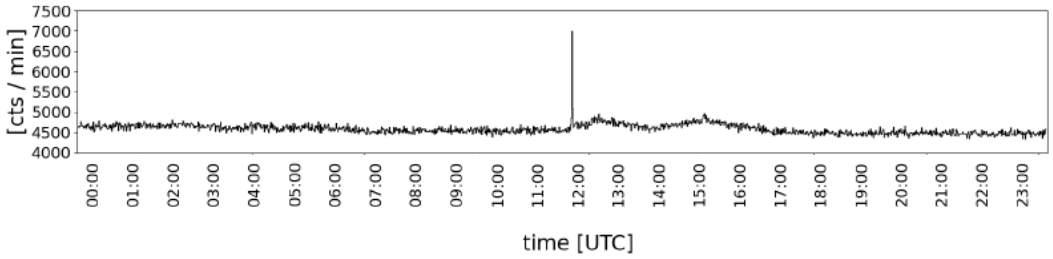

Figure 3.27: Energy-integrated light curve of April 24th 2023 for the *gammaflash1a* detector, with temporal bins of 1 minute. The gamma-ray glow occurring at 12:13 UTC is clearly observed in the data as an excess in counts.

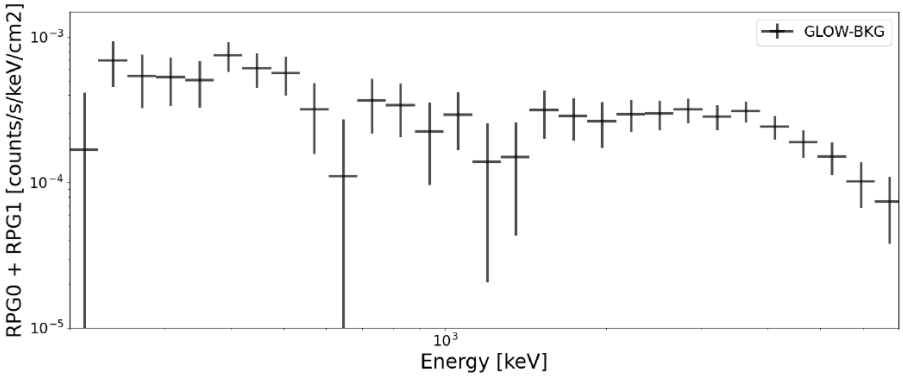

Figure 3.28: Time-integrated spectrum considering the sum of *gammaflash1a* and *gammaflash2a* counts of April 24th 2023. Specifically, a component above 2.6 MeV not compatible with the background can be observed.

Regarding PIZ-Gamma setup, three different gamma-ray glows were detected and are presented in the following. In particular, the first one was detected on July 31st 2025 during a thunderstorm and it was identified through the analysis of the light curve and the spectrum. Starting with the light curve, the full-day acquisition for *pizgamma1* is shown in Fig. 3.29: the corresponding light curve for the second detector is identical and therefore not reported. The plot shows two radon-washout events that lasted a couple of hours and a gamma-ray glow of less than two minutes, which occurred during the second radon-washout episode. The gamma-ray glow alone is shown more clearly in Fig. 3.30, again for *pizgamma1*.

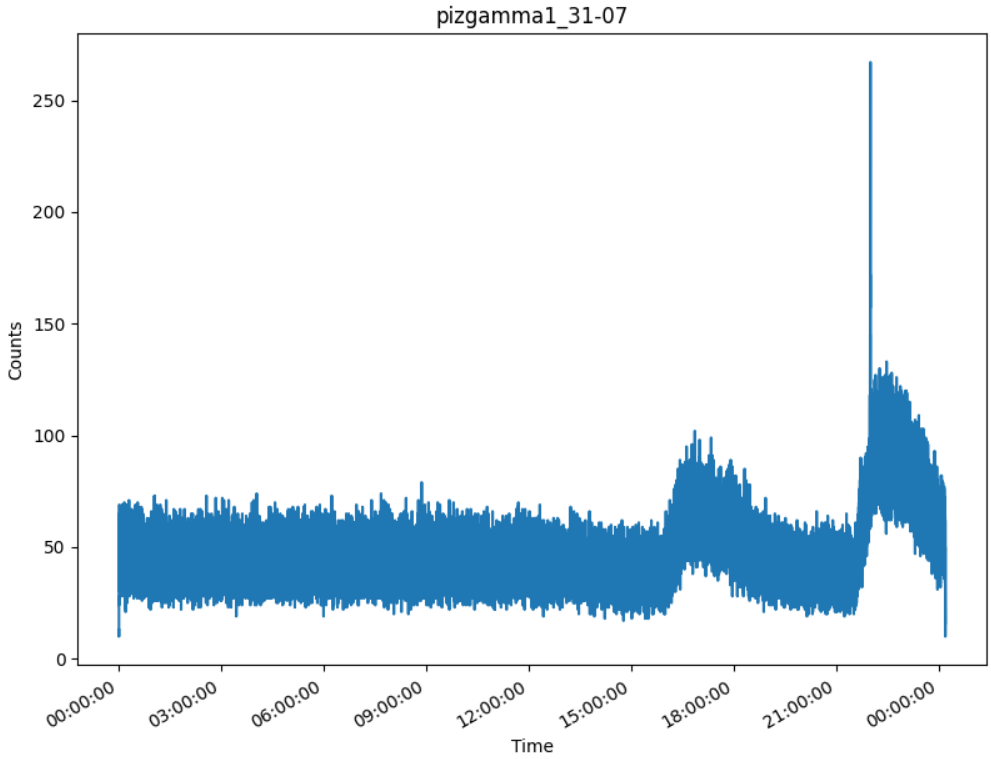

Figure 3.29: Energy-integrated light curve of *pizgamma1* detector with temporal bins of 1s, showing the full-day acquisition of July 31st 2025. Two radon-washout events and a gamma-ray glow can be identified because of their duration, respectively, of a couple of hours and less than two minutes.

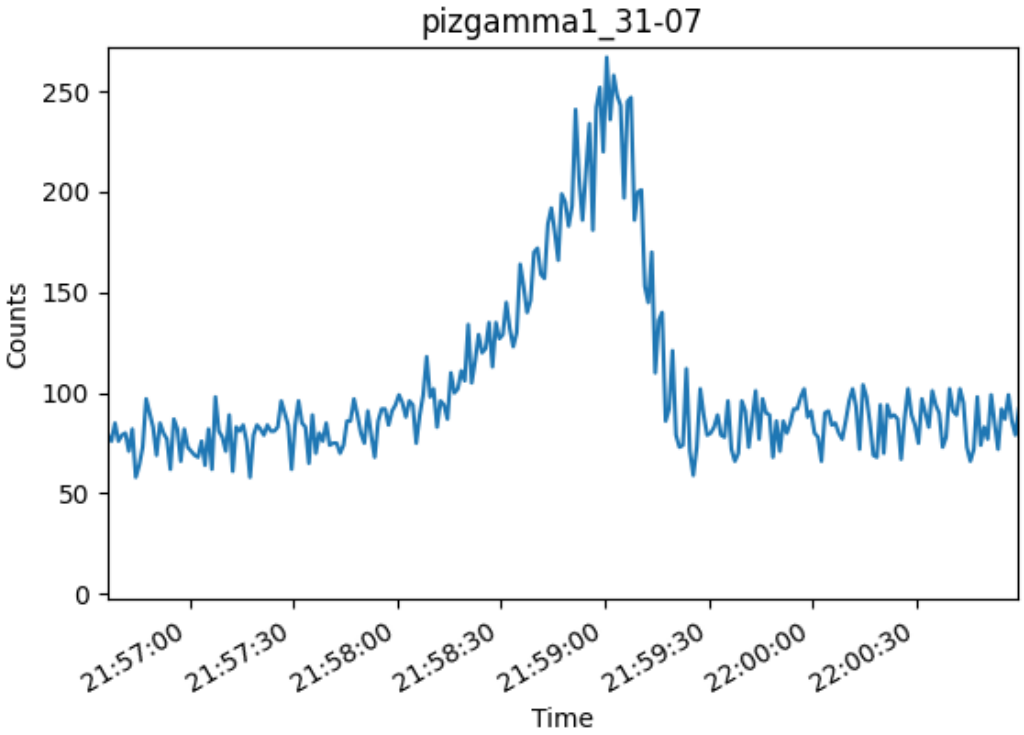

Figure 3.30: Zoom-in of the energy-integrated light curve of *pizgamma1* detector in Fig. 3.29, in order to highlight the duration of the gamma-ray glow, which is about a minute and a half.

At this stage, the spectrum was also examined. In particular, Fig. 3.31 shows a time-resolved spectrum for the three-hour interval corresponding to the second radon-washout event and the associated gamma-ray glow. At the time of the glow, a clear excess of events appear in some specific channels. This excess starts to be visible at energies above 5-10 MeV, clearly indicating the high-energy nature of the phenomenon.

Furthermore, the script responsible for trigger detection worked correctly, since it revealed for *pizgamma1* an increase in the number of counts with respect to the background at times: 21:58:45, 21:58:55 and 21:59:05, which are the times with the highest number of counts observed in Fig. 3.30. This result was obtained considering as reference background the first 20 s of data in the file, a temporal bin of 10 s and a threshold level of 5 sigma.

Therefore, this complete analysis just described was carried out for the first PIZ-Gamma gamma-ray glow detected, which was identified as such after the investigation of its light curve and spectrum. Regarding the other two gamma-ray glows detected on Piz Boè, they were both detected in the same day (August 28th 2025), in coincidence with a strong thunderstorm occurring in that area. The same kind of analysis performed

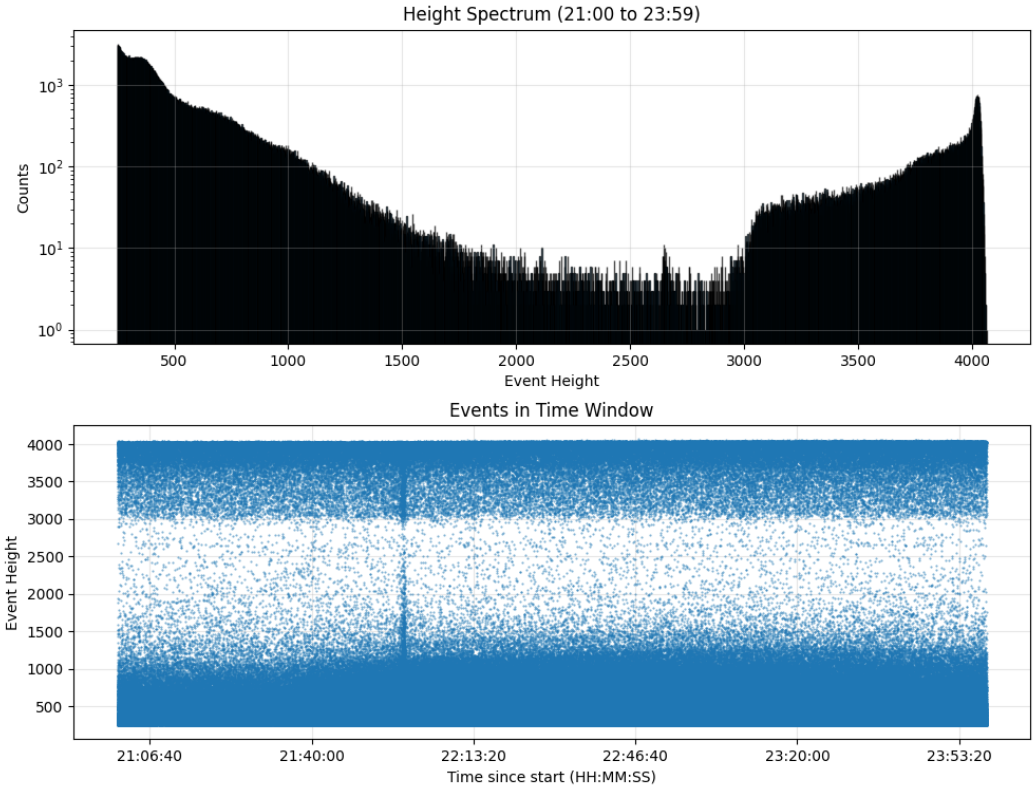

Figure 3.31: Time-resolved spectrum of *pizgamma1* detector. Specifically, a period of three hours was considered, which includes the second radon washout and the gamma-ray glow. In coincidence with the glow, channels above 5-10 MeV show a clear excess in the number of events detected.

for the first glow was carried out also for these other phenomena. Starting with the light curve, the one related to all the day of acquisition is shown in Fig. 3.32 only for *pizgamma1*, in which both gamma-ray glows can be observed. They both occurred during a radon washout as in the previous case and the second one has a larger count rate with respect to the first one. Both gamma-ray glows lasted for about two minutes, whereas, the radon washout was about seven hours. Moreover, two zoom-ins of the glows are represented in Fig. 3.33 to better visualize these phenomena alone.

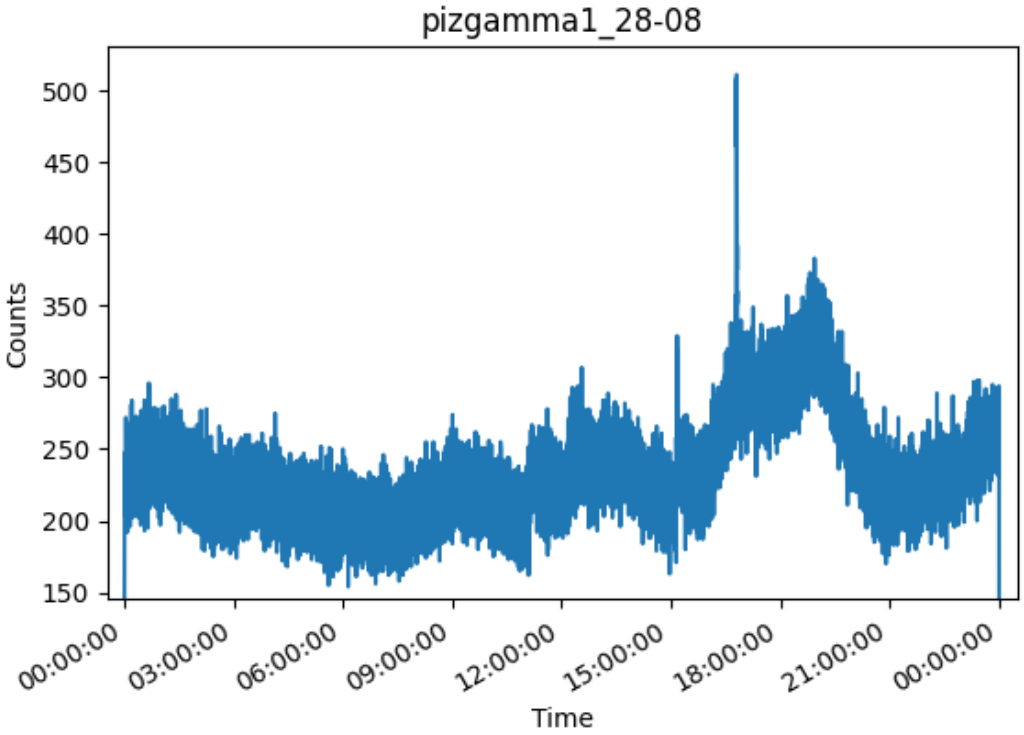

Figure 3.32: Energy-integrated light curve of *pizgamma1* detector with temporal bins of 5 s. Therefore, the counts per 5 s are plotted against the time at which the events occurred. It is related to August 28th 2025. Two gamma-ray glows can be identified because of their duration, both lasted for about two minutes.

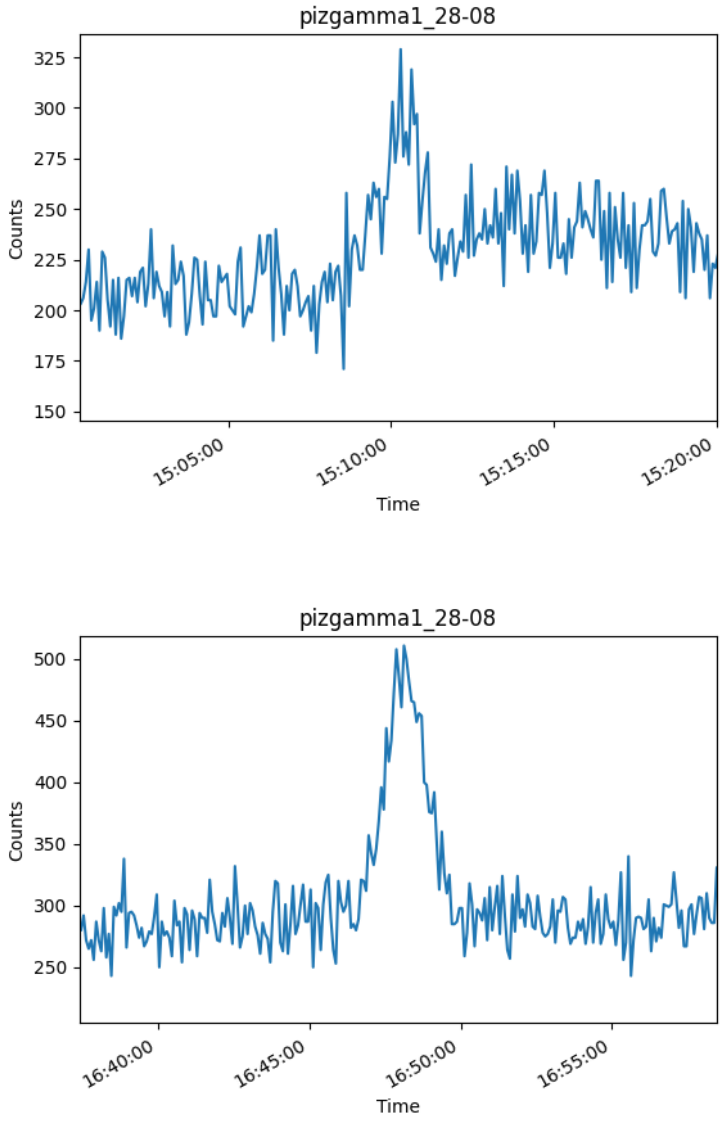

Figure 3.33: *Top image*: Zoom-in of the first gamma-ray glow of the energy-integrated light curve in Fig. 3.32, highlighting its duration of about two minutes. *Bottom image*: Zoom-in of the second gamma-ray glow of the energy-integrated light curve in Fig. 3.32, highlighting its duration of about two minutes.

A time-resolved one was considered and is shown in Fig. 3.34. Only the period associated to the radon washout and the gamma-ray glows was considered (7 hours). At the times of the two gamma-ray glows, a clear excess of events starts to be visible at energies above 5-10 MeV, confirming the high-energy origin of the phenomena as for the first glow analyzed above.

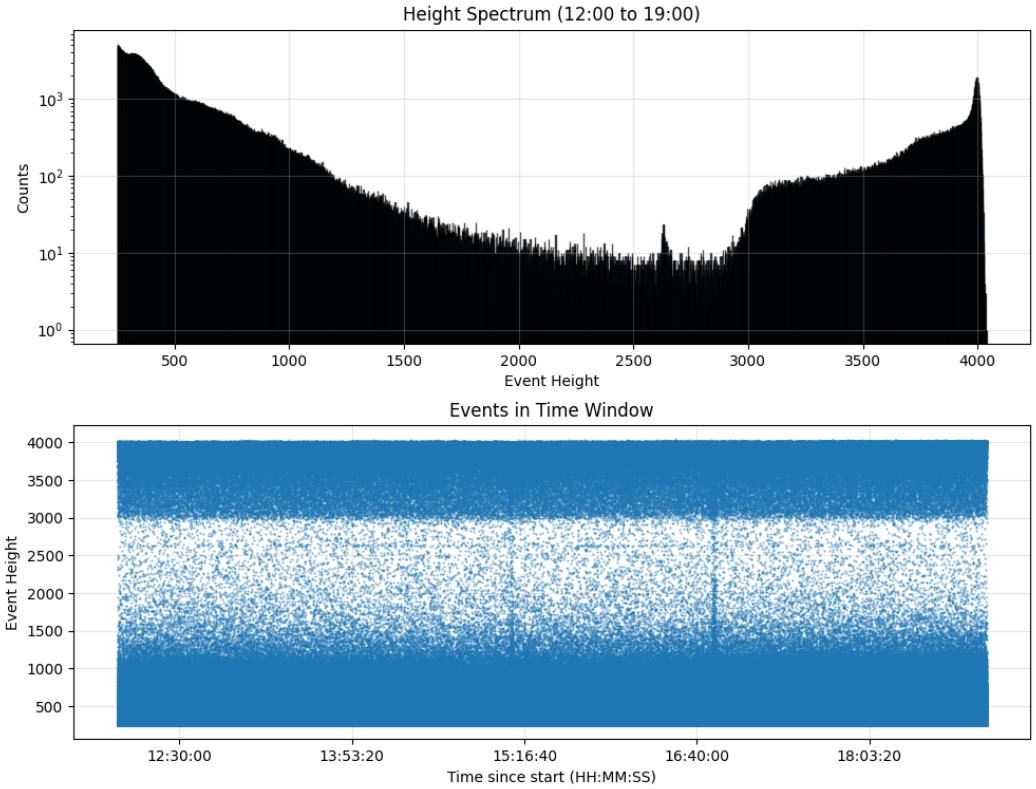

Figure 3.34: Time-resolved spectrum of *pizgamma1* detector. Specifically, a period of seven hours was considered, which includes the radon washout and both the gamma-ray glows. In coincidence with the glow, channels above 5-10 MeV show a clear excess in the number of events detected.

In the end, also the trigger detection mechanism was checked. The first gamma-ray glow, which presented a lower number of counts with respect to the second one, was not revealed by this mechanism. Instead, it worked correctly for the second gamma-ray glow revealing for *pizgamma1* an increase in the number of counts with respect to the background at times: 16:47:45, 16:47:55, 16:48:05, 16:48:15, 16:48:25 and 16:48:35. These results were obtained considering as reference background the first 20 s of data in the file, a temporal bin of 10 s and a threshold level of 5 sigma. Concluding in this way the analysis of these phenomena.

Considering these results obtained, it can be noticed that more high-energy atmospheric transient phenomena are detected in a shorter range of time by PIZ-Gamma detectors rather than Gamma-Flash ones. This could be due to the different site locations and the position of the instruments themselves. In the PIZ-Gamma case the setup is placed at a higher altitude with respect to the Gamma-Flash one, resulting in less atmospheric extinction that can affect data. Moreover, the two Mt. Piz Boè detectors have less shielding mass surrounding them, since they are placed outside the refuge as showed in Fig. 3.5 and in Fig. 3.8. Instead, the Mt. Cimone detectors are inside a dome and next to a building, resulting in a restriction of their field of view, as it can be seen in Fig. 3.6.

Chapter 4

8U CubeSat implementation

The results obtained in Sec. 3.6 from Gamma-Flash and PIZ-Gamma projects showed that detections of high-energy atmospheric transient phenomena from ground are not so common. Indeed, considering months of acquisition, only a few gamma-ray glows were detected, possibly due to the atmospheric extinction related to the altitude of the sites and the limited field of view of the setups. Therefore, a possible improvement of these projects was considered and is presented in this chapter. Specifically, considering as a starting point the GAmma-ray burst Localizing Instrument (GALI) presented in Saleh-Natur (2024) and described Sec. 4.1, a similar system was conceived with specific characteristics. This new design is more efficient than the ground-based projects analyzed in this work and can detect both high-energy atmospheric and astrophysical transient phenomena from space: it consists of a $20\times20\times20$ cm^3 8U CubeSat with instruments similar to those of the PIZ-Gamma setup. This system has 4π field of view in order to reveal both atmospheric and astrophysical phenomena. Its effective area and localization capability were tested and studied through Monte Carlo simulations performed with an open-source software toolkit called MEGAlib (Medium-Energy Gamma-ray Astronomy Library). In particular, in Sec. 4.1 the principal characteristics of the instrument that helped to develop the concept for the CubeSat are described. Afterwards, the structure chosen for this CubeSat is presented in Sec. 4.2, along with a general overview of MEGAlib and related parameters. In Sec. 4.3, the group of simulations carried out for the study of the detector effective area are reported with related outcomes. The models considered for the analysis of the localization capabilities are presented in Sec. 4.4, along with their results. Eventually, other possible future aspects and characteristics related to this system, which were not analyzed in this thesis, are considered.

4.1 GALI - GAmma-ray burst Localizing Instrument

A detector concept that helped develop the idea for the 8U CubeSat mentioned above is GALI, which enables accurate localization of GRBs. Its general characteristics are reported in the following, but its detailed description can be found in Saleh-Natur (2024). The structure of this system is composed of 362 CsI crystal scintillators (9×9×9 mm^3) coupled with SiPMs. Each one of these detectors is randomly coupled with a printed circuit board (PCB) and these random locations were selected following simulations to achieve the best angular localizing accuracy. Moreover, each SiPM is readout by one application-specific integrated circuit (ASIC) channel and an on-board data handling unit is connected to the ASIC to read all the data.

Monte Carlo simulations were performed in order to study the localization capabilities of GALI and were based on MEGAlib. In particular, the model of the detector included all the parts that can absorb and reflect gamma-rays and simulated a continuous background radiation. Moreover, high-count rate GRBs were considered on a sky grid to create a reference map of relative count rates on each scintillator as a function of the sky angle. Afterwards, the simulation generated several fainter GRBs arriving from random directions with a uniform photon flux of 10 photons cm^{-2} s^{-1} and a duration of 1 s, considering a power-law spectrum with specific characteristics ranging the energies between 10 and 1000 keV. At this stage, the number of counts in each individual scintillator was registered for each GRB and was compared with the ones of the reference map, in order to estimate the angle of arrival of the event. These burst localizations were used to produce a map of GALI's average estimated angle uncertainty, which is of a few degrees ($<2.3°$) over the entire sky. Furthermore, GALI has an effective area of 100 – 140 cm^2 that peaks in the direction of the corners of the cube-shaped detector. These are the main characteristics of GALI: some of them were the starting points for the development of the 8U CubeSat model.

4.2 8U CubeSat and MEGAlib overview

The possible improvement of Gamma-Flash and PIZ-Gamma projects was taken into consideration since from ground gamma-ray glows and TGFs detections over months of acquisition were not so common, as previously stated. Therefore, taking GALI as a reference model, a similar system capable of detecting both high-energy atmospheric and astrophysical phenomena was designed: an 8U CubeSat. Considering that 1U corresponds to a standardized unit of 10×10×10 cm^3, giving a total volume of 1000 cm^3, an 8U CubeSat is 8 times the volume of 1U (8000 cm^3). The payload consists of a number of sensitive volumes which are voxels (i.e. pixels in 3D), whose quantity and dimension can be changed. Each one of them is composed of a CsI crystal scintillator, which is coupled with a SiPM. The goal of this study is to explore the

parameters which drive the design of the 8U CubeSat.

This kind of system was studied performing simulations with MEGAlib, which is a set of software tools designed primarily to analyze data of Compton telescopes. It was decided to use it instead of Geant4, since is easier to use and has a specialized framework for gamma-ray and X-ray astronomy. Its library comprises all the data analysis procedure, starting with simulations and measurements to event and image reconstruction. In particular, Geomega and Cosima are two major MEGAlib components used for the simulations carried out. Geomega provides a uniform geometry and detector setup description. It allows to build and visualize the configuration of the system through the production of a geometry file, which includes the description of all the materials, volumes, detectors, trigger criteria etc. Cosima is a universal simulator that analyzes the interaction of high-energy photons with matter via different processes, such as photoelectric effect, Compton scattering and pair production. Therefore, it allows to define the sources for the simulations through specific related files, in which several information are contained such as the kind of particles, energies, fluxes etc. This file is used along with the geometry one in order to generate the final simulation files (sim-files), which are the output of Cosima. The parameters related to the geometry and source files are described in further details in the following, respectively, in Subsec. 4.2.1 and Subsec. 4.2.2.

4.2.1 Geometry file parameters

The geometry file has several parameters that can be chosen, and the ones used for the simulations are described in the following, according to Zoglauer A. (2020). In MEGAlib, the first step in defining a simulation geometry is the creation of the world volume, i.e., the outermost container that encloses the entire setup. After assigning a name to this world volume, its fundamental properties must be specified. The material is selected via the command *WorldVolumeName.Material*, followed by the chosen medium (e.g., *Germanium*, *Vacuum*, etc.). The geometrical shape of the world volume is then defined using *WorldVolumeName.Shape*; for instance, choosing *BOX* requires providing its three side lengths in centimeters. The spatial placement of the volume is set through *WorldVolumeName.Position*, where the three coordinates of its center must be given, also in centimeters. Finally, the command *WorldVolumeName.Mother* followed by 0 indicates that this volume is the top-level container, i.e., the mother volume for the entire geometry.

At this point, a surrounding sphere must be defined, a structure required when simulating sources located at infinity. In the far-field approximation implemented in MEGAlib, incoming particles are generated on a disk that is tangent to this sphere and oriented toward its center. The sphere must completely enclose the entire detector geometry to ensure that all incoming rays intersect the simulation setup correctly. The sphere is created using the command *SurroundingSphere*, followed by five values (in cm): the radius of the sphere, the three coordinates of its center, and the distance of

the particle-generation disk from the center (which typically equals the sphere radius). Finally, its visual display in the geometry viewer can be toggled through the command *ShowSurroundingSphere*, which accepts the Boolean values *true* or *false* to show or hide the sphere, respectively.

Afterwards, the focus is shifted to the detectors of the system. Starting with their materials, the related density is defined with *Material.Density* in g/cm^3. Afterwards, the components of the material can be declared too, considering that there can be a mixtures of different components. Each one of them is defined with *Material.Component* followed by the element and its related number of atoms. At this stage, after having defined the name of the specific detector, the position of its center is defined through *DetectorName.Position* with the three coordinates in cm. Regarding its dimensions, *DetectorName.Shape* allows to assess them: for example for the *BOX* case the three dimensions are specified in cm. Concerning the material of the detector is assigned via *DetectorName.Material* followed by the material previously defined. Afterwards, through *DetectorName.Mother* with *WorldVolumeName* is possible to specify that the detector is contained inside the world mother volume. Moreover, other characteristics and details of the detector are given. Considering *DetectorName_Detector.SensitiveVolume* followed by *DetectorName*, the volume in which the positions and energies of interactions are measured is defined. Then, *DetectorName_Detector.Offset* allows to specify the distance between the edge of the detector volume to the beginning of the first sensitive volume. Thus, the latter invocation need to be accompanied by x, y and z spacing in cm. Afterwards, to establish a trigger threshold and assume that a hit needs to deposit at least a certain energy to raise a trigger signal, *DetectorName_Detector.TriggerThreshold* is used followed by the related energy in keV. The energy resolution information are given by *DetectorName_Detector.EnergyResolution* and different parameters are needed depending on the case. For the *Gauss* case for example, different values (in keV) are needed: the input energy, the energy of the Gauss distribution peak and one sigma width of Gauss distribution. Moreover, it is possible to specify if detector is voxel or strip and how many of them make it up through *DetectorName_Detector.VoxelNumber* or *DetectorName_Detector.StripNumber* followed by the number of strips/voxels in each direction (x, y and z). These detector parameters just reported can be defined for each instrument of the system considered. Ultimately, some characteristics related to the triggers that can be related to all the instruments are reported. *TriggerName.Veto* determines if a trigger is real (acceptance) or a veto (rejection). It can be set as *true* or *false*, being false by default. Afterwards, it can be chosen if the triggering happens by channel with *TriggerName.TriggerByChannel* (channels are counted for the trigger) or by detector through *TriggerName.TriggerByDetector* (irrelevant how many channels in the detector have triggered, detectors are counted for the trigger). Ultimately, the type of detector is defined with *TriggerName.DetectorType* followed by the related detector name (e. g. *Voxel3D*, *Strip2D* etc.) and the number of hits required to raise the trigger or veto. All these parameters described are the ones used in the simulations carried

out and reported in Sec. 4.3 and Sec. 4.4.

4.2.2 Source file parameters

The source file has several parameters that can be modified, and the ones used for the simulations are described in the following, according to Zoglauer A. (2021).

At first, the name of the sim-file that is generated from that specific source needs to be defined through *MyRun.FileName* followed by the name. Afterwards, the simulation stop criterion is defined and can be fulfilled in three ways: when a given number of events is simulated (*MyRun.Events*), when a chosen number of triggers is achieved (*MyRun.Triggers*) and when a certain simulation time is passed (*MyRun.Time*). At this stage, after having defined the name of the source (*MyRun.Source* with related *SourceName*), all its related specific parameters are defined. Starting with the choice of the kind of particles with *SourceName.ParticleType*, followed by a certain number that is referred to a specific particle. Then, the beam type is chosen with *SourceName.Beam* and can be of different types. When a source from a finite point is considered, just the point coordinates, the source direction and the amplitude of the beam are needed. The surrounding sphere, which was introduced in Subsec. 4.2.1, is not required in this case. When a source at infinity is considered, instead, the particles chosen are started on a disk whose center sits on the surrounding sphere, and their direction is perpendicular with respect to the disk pointing to the center of the surrounding sphere. A couple of examples related to the beam type are reported: a point source on the sphere is represented with (*FarFieldPointSource* followed by the direction of the emission given by θ and ϕ, particles emitted isotropically from 4π are denoted with (*FarFieldIsotropic*) and many others can be selected. Afterwards, the spectral type of the source is defined with *SourceName.Spectrum* and is chosen among different kind of spectra, such as a monochromatic source with a certain energy, a power law with a specific relation, a black body etc. Ultimately, the absolute flux of the beam is given with *SourceName.Flux* followed by flux in particles cm^{-2} s^{-1} or particles s^{-1} depending on the type of beam. All these parameters described are the ones used in the simulations carried out and reported in Sec. 4.3 and Sec. 4.4.

4.3 Effective Area investigation

In this section, following the previous sections with the description of the CubeSat main characteristics and the overview of MEGAlib parameters employed in the simulations, the different groups of simulations are presented. In particular, a first group is analyzed in Subsec. 4.3.1, in which different CubeSat filling densities were studied. The related geometries chosen and the obtained results are reported. The second group of simulations, which was performed considering a fixed CubeSat density but different

detectors dimensions, is described in Subsec. 4.3.2, along with the geometries considered and the related outcomes. Ultimately, the results obtained from first and second group of simulations were applied to the third group of simulations, which is detailed in Subsec. 4.3.3. A certain CubeSat filling density and a specific detectors dimension were fixed and the system was studied considering different source directions.

4.3.1 CubeSat filling density optimization

The first group of simulations aims to study the effective area considering different CubeSat densities. In particular, five different values for the number of detectors contained in the 8U CubeSat were evaluated, thus obtaining different fractions of volume occupied. The procedure to build the geometry for these five simulations is described in the following. At first, the 8U CubeSat dimension was fixed to 20 cm, as previously stated. Then, it was decided to choose also a certain dimension for each small cubic detector (scintillation crystal) inside the system, which was of 10 mm. Specifically, a Python script was written that allowed to create a grid of coordinates (x, y and z) of cubes centers considering the CubeSat and the detectors dimensions previously stated. The coordinates were chosen to obtain a random 3D distribution of a certain number of cubic detectors. In particular, simulations were carried out using five different numbers of detectors: 500, 800, 1000, 2000, and 8000. By setting the parameters reported in Subsec. 4.2.1, different system and detectors characteristics were chosen, which are listed in the following. Furthermore, some of these geometries are shown in Fig. 4.1.

- The world mother volume was defined as a cube with a side length of 40 cm, since it should contain all the instruments and the surrounding sphere. Furthermore, it was centered on the origin of the system and filled with vacuum;
- the surrounding sphere was considered with a radius of 18 cm and centered in the origin of the system;
- the detectors material was CsI with 4.51 g cm^{-3} density and a composition of one Cs atom and one I atom. This material was chosen as the scintillation crystal because it is well suited for the detection of high-energy transient phenomena and is the same material used in the PIZ-Gamma project;
- the coordinates of each detector are the ones obtained from the Python script with the procedure previously described;
- the detectors shape was fixed as a cube with a side length of 10 mm;
- the volume of each detector was considered to be sensitive to positions and energies measurements;
- the trigger threshold was fixed to 50 keV for each detector;

- the calibration of the energy resolution of the detectors was performed considering two input energies (500 keV and 5000 keV) and fixing the related Gaussian peak energies (500 keV and 5000 keV) and sigmas (5 and 50);
- each cubic detector consists of a scintillation crystal coupled with a SiPM, even if the latter was not considered in the geometry modeling. Thus, it was suitable to consider each detector as a single voxel not further divided in channels;
- the number of hits required to raise a trigger was set to 1 for each voxel;
- the veto criteria were not included for the detectors.

After having defined all the parameters associated to the CubeSat geometry and having created the five geometries, the sources chosen for the five simulations are presented. Twenty monochromatic energies were fixed, starting from 100 keV to 2000 keV, with steps of 100 keV. These twenty source files were considered for each of the five simulations of this first group. The other parameters, which are in common for all these sources, are reported in the following.

- the stop criterion was set to be fulfilled when a certain number of events was simulated: 10^5;
- the particles considered were photons, thus the associated parameter was set to 1;
- the sources were at infinity and the direction of the emission was on-axis (θ=0° and ϕ=0°);
- the absolute flux of the beam particles was set to 10^6 photons cm^{-2} s^{-1}.

At this stage, after the description of both geometry and sources parameters, the effective area was calculated with the following formula:

$$A_{eff} = \frac{Interacted\ Photons}{Generated\ Photons} \cdot A_{beam} \tag{4.1}$$

where *Interacted Photons* is the number of photons that interacted with the CubeSat detectors and they were selected considering at least one interaction with a detector, no matter how much energy was absorbed by the voxel. The total number of photons generated during a simulation (10^5 for each simulation of this first group) is represented by *Generated Photons*. Instead, A_{beam} is the area of the photons beam, which is $\pi \cdot (18\ cm)^2$ (where 18 cm is the radius of the surrounding sphere). Considering this formula, it can be noticed that by increasing the beam area and having the number of generated photons fixed, the number of photons per unit area would decrease. Thus,

the number of photons interacting with the detectors would decrease with increasing beam area, resulting in an effective area that does not change.

Therefore, the outcomes of this first group of simulations are shown in Fig. 4.2. In the case in which all the volume is filled with detectors (8000 voxels), the effective area at each energy corresponds to one face (400 cm^2) of the CubeSat, as expected. Regarding the other curves (for 500, 800, 1000 and 2000 voxels) the behavior is always the same: the effective area has its maximum at lower energies and decreases towards higher energies. Indeed, photons with higher energies have a smaller probability to interact with matter and can escape the CubeSat, resulting in a lower value of *Interacted Photons* so in a smaller A_{eff}. Moreover, considering the case of 2000 voxels, the effective area at low energies (below 300 keV) is the same as the one of the configuration with 8000 voxels and at higher energies it has a decrease of the $\sim$ 25%, since the percentage of occupied volume decreases too. This 2000 detectors configuration was considered a good trade-off for the system geometry mainly for two reasons. The first was related to the number of voxels: when it is too high (8000 detectors) and the total system volume is occupied, the localization capability is limited since the inner part of the CubeSat would not be reached by the events and the system would not be exploited in a proper way. Furthermore, considering the full volume occupied by detectors, the system would be too complex to be implemented in real case study. Therefore, the complexity of the simulation would be too high in this case and it is better to consider less voxels for the aspects just explained. The second reason was related to the behavior of the effective area, which has the smaller decrease ($\sim$ 25% at high energies) for the 2000 detectors configuration with respect to the other curves. Therefore, because of these results and considering that 25% of CubeSat volume is occupied in the case of the 2000 voxels (10 mm dimension) configuration, it was decided to fix this percentage of occupied volume for the following simulations.

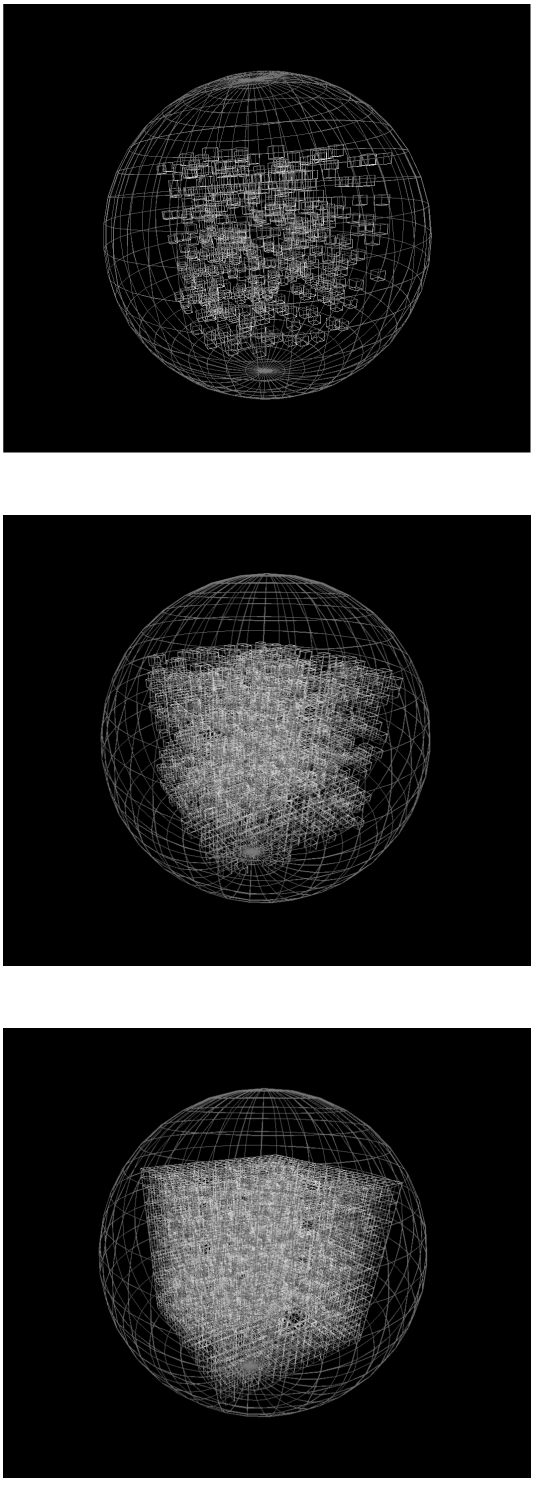

Figure 4.1: *From top to bottom*: 500 voxels, 2000 voxels and 8000 voxels geometry configurations of the first group of simulations.

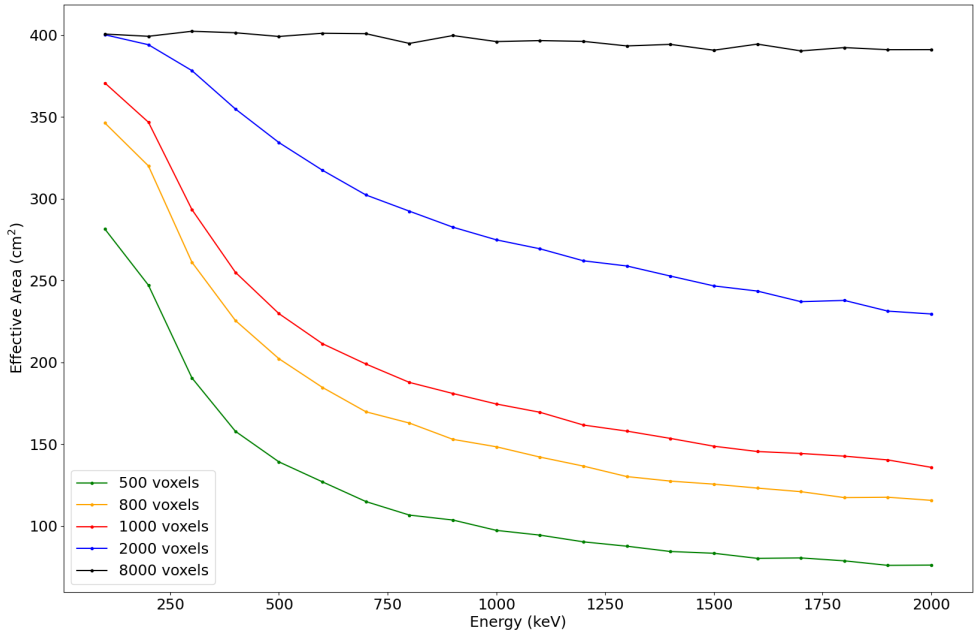

Figure 4.2: Outcomes of the first group of effective area simulations. It can be observed that when all CubeSat volume is filled with detectors (8000 voxels), the effective area is the maximum one and corresponds to the area of one face of the CubeSat (400 cm^2). For the other curves the general behaviour is always the same: effective area is larger at lower energies and decreases at higher energies, as explained in this section.

4.3.2 Voxels size optimization

The second group of simulations aims to study the effective area considering different voxels dimensions. In particular, five detector dimensions were evaluated, keeping the volume filling fraction always fixed to 25%. The general procedure to build the geometry for these five simulations was the same as the one described in Subsec. 4.3.1 and the same script was used. In particular, the number of coordinates randomly selected in this case was considered depending on the voxels dimensions. Considering the fixed percentage of occupied volume (25%) and the five voxels dimensions of 6 mm, 8 mm, 10 mm, 12 mm and 15 mm, the related number of detectors obtained for each configuration was, respectively, 9259, 3906, 2000, 1157 and 592. Regarding the parameters used for the geometry, they are the same as the ones listed in Subsec. 4.3.1. The only variable that changed was the one related to the detectors dimension, which was changed five times, with the values just reported. Three of these geometries (6 mm, 10 mm and 15 mm) are shown in Fig. 4.3.

After the creation of the five geometries for this second group of simulations, the focus was shifted to the source files. As in Subsec. 4.3.1, twenty monochromatic energies were fixed starting from 100 keV to 2000 keV, with steps of 100 keV. These twenty source files were considered for each of the five simulations of this second group. The other parameters used for these files are the same as those listed in Subsec. 4.3.1.

At this stage, after the description of both geometry and sources files, the effective area was obtained with the exact same procedure outlined in Subsec. 4.3.1. The outcomes of this second group of simulations are shown in Fig. 4.4. The effective area has a general behavior that is the same for each curve represented: it has higher values at lower energies and decreases towards higher energies. The reason for this behavior is the same as the one explained in Subsec. 4.3.1. It can be observed that for larger voxels dimensions the effective area values are smaller. In particular, considering the 12 mm and 15 mm dimension detectors, the effective area is reduced by $\sim$5% with respect to the other cases. Thus, it would be better to consider smaller voxels dimensions to obtain an higher effective area. At the same time, a high number of detectors can have the same effects already described in Subsec. 4.3.1. Specifically, in the case in which the dimensions are smaller, the number of voxels is higher, resulting in a more complex system. Therefore, the trade-off in order to have both higher effective areas and less complexity of the simulation is achieved with 10 mm voxels dimensions. For these reasons, it was decided to fix the detectors dimension in this way. Thus, for the last group of simulations for the effective area investigation the percentage of occupied volume was maintained set to 25% and the voxels dimensions was fixed to 10 mm.

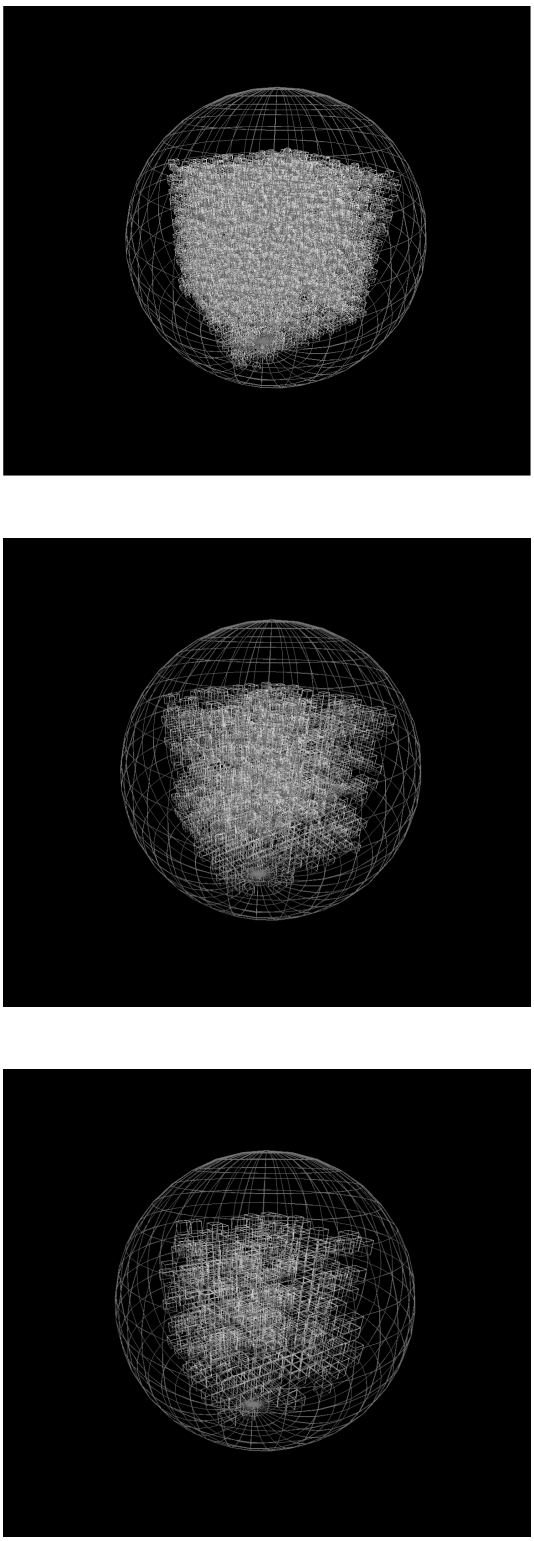

Figure 4.3: *From top to bottom*: 6×6×6 mm^3 voxels, 10×10×10 mm^3 voxels and 15 × 15 × 15 mm^3 voxels geometry configurations of the second group of simulations.

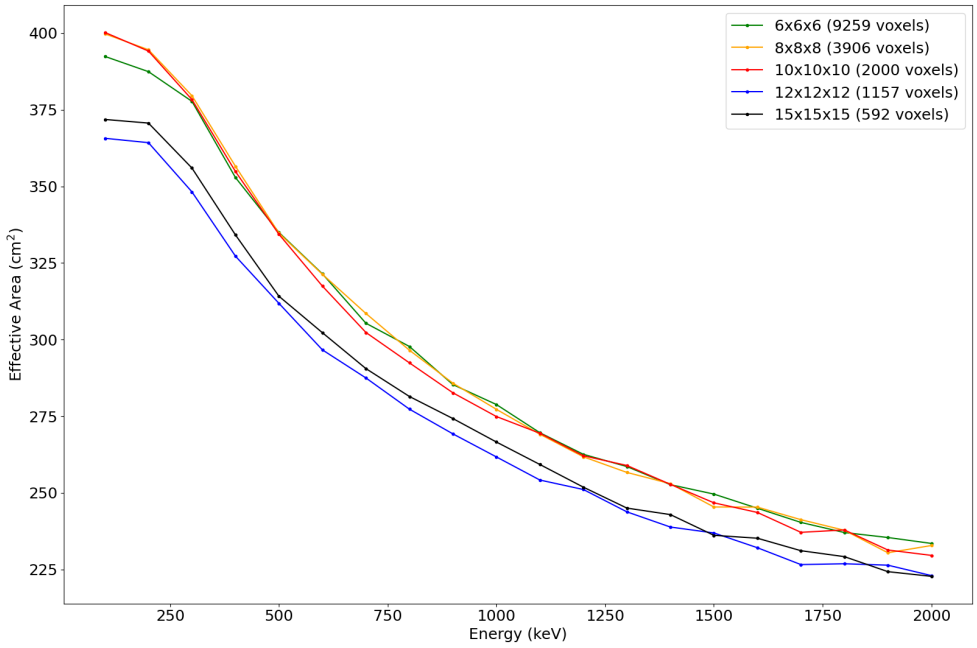

Figure 4.4: Outcomes of the second group of effective area simulations. It can be observed that the general effective area behaviour is the same for each curve: higher effective area values at lower energies and lower ones at higher energies, as explained in Subsec. 4.3.1. Furthermore, a decrease of ∼5% in the effective area values is shown for bigger voxels dimensions (12 mm and 15 mm).

4.3.3 Dependence of the effective area on the source direction

The third group of simulations aims to study the effective area considering off-axis sources. In Subsec. 4.3.1 and Subsec. 4.3.2, the sources were always considered on-axis (θ=0° and ϕ=0°) for each simulation performed, thus in this last group of effective area simulations different directions of the sources were explored. In particular, the percentage of occupied volume was set to 25%, the voxels dimensions was fixed to 10 mm and four pair of angles were chosen to simulate different directions of arrival of photons. Only one geometry, which is shown in Fig. 4.7, was built for this third group of simulations: the related procedure is the same as the one described in Subsec. 4.3.1 and the same script was used. In particular, the number of coordinates randomly selected in this case was fixed to 2000 (25% of occupied volume with 10 mm voxel dimension). Regarding the parameters used for the geometry, they are the same as the ones listed in Subsec. 4.3.1.

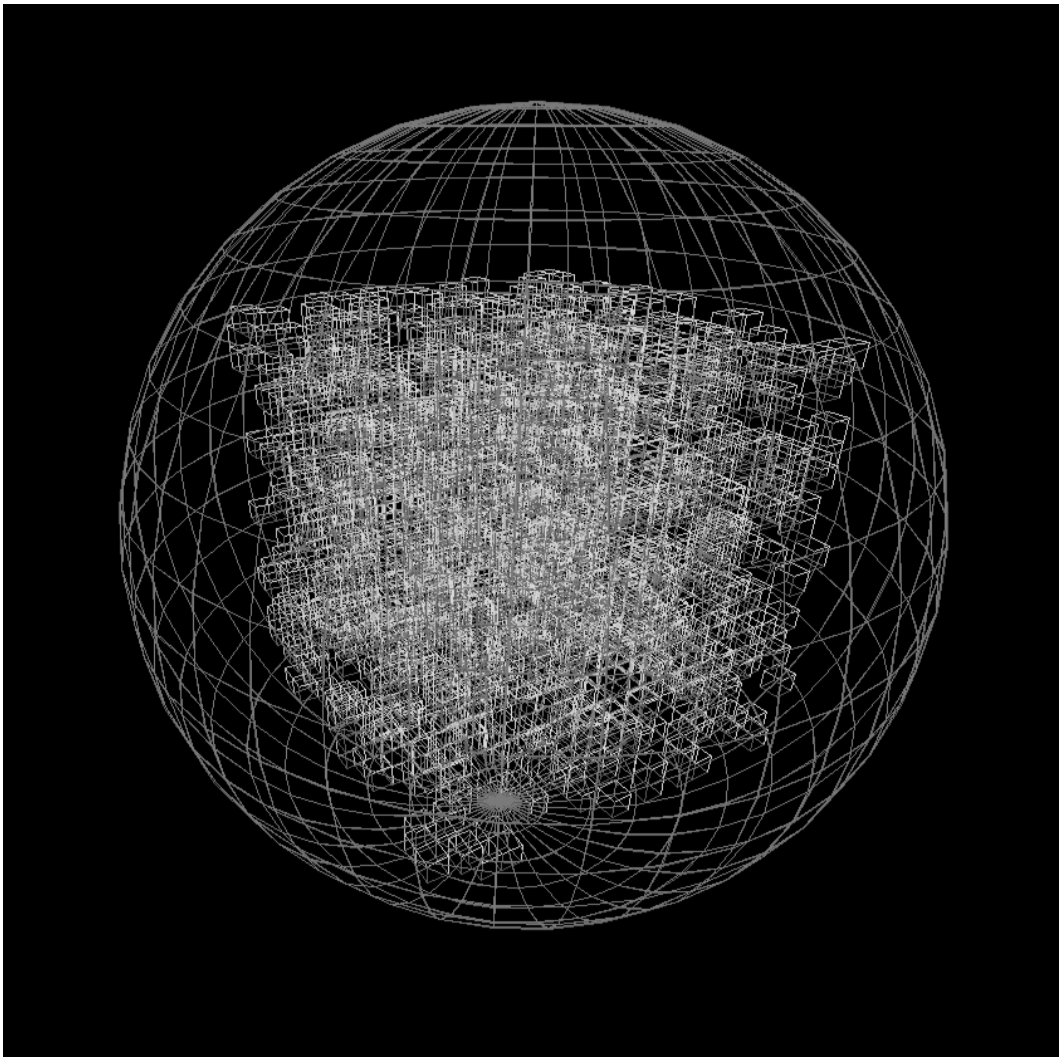

Figure 4.5: $10\times10\times10$ mm^3 voxels geometry configuration for the third group of simulations.

After the creation of one geometry for this third group of simulations, the focus was shifted to the source files. The sources parameters used are the same of the ones listed in Subsec. 4.3.1 except for the one related to the direction of the source. Indeed, in this case four different pair of angles were selected: θ=0° and ϕ=0°, θ=30° and ϕ=0°, θ=45° and ϕ=0° and θ=54.7° and ϕ=45°. The latter was chosen since it is along the diagonal of the CubeSat. For each direction, twenty monochromatic energies were fixed starting from 100 keV to 2000 keV, with steps of 100 keV, as in Subsec. 4.3.1. Moreover, a Python script was used to test and visualize a heat map of the 3D hits distribution within the CubeSat with the following directions: (θ=0° and ϕ=0°), (θ=40° and ϕ=0°) and (θ=90° and ϕ=0°), all at 100 keV. The related results are shown in Fig. 4.6.

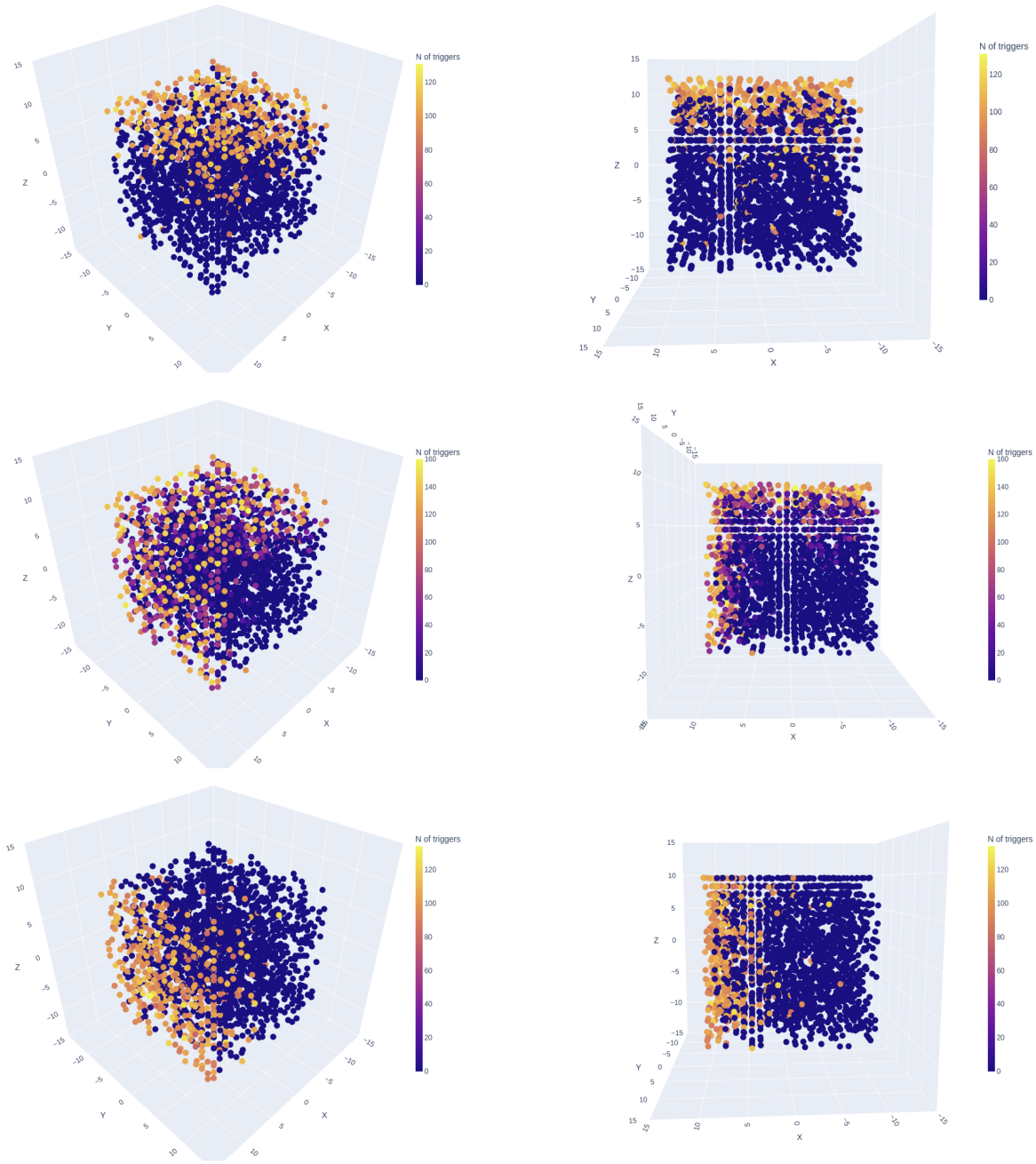

Figure 4.6: *From top to bottom*: 3D hits distribution within the CubeSat with (θ=0°, ϕ=0°), (θ=40°, ϕ=0°) and (θ=90°, ϕ=0°) source directions. The voxels illuminated are compatible with the three direfferent directions of the sources, since the yellow and orange ones are related to a higher number of triggers.

After the creation of both geometry and source files, the effective area was obtained

with the exact same procedure outlined in Subsec. 4.3.1.

Therefore, the outcomes of this third group of simulations are shown in Fig. 4.7. The effective area has a general behavior that is the same for each curve represented: it has higher values at lower energies and decreases towards higher energies. The reason for this behavior is the same as the one explained in Subsec. 4.3.1. It can be observed that the highest effective area is obtained when the direction of the source is along the CubeSat diagonal (θ=54.7° and ϕ=45°), as expected. Indeed, this result is reliable, as in this case the portion of the CubeSat area illuminated by the source is the largest among all configurations. In contrast, when the source is on-axis (θ=0° and ϕ=0°) the effective area has the smallest values, since the illuminated CubeSat area is the smallest one in this configuration. For the other two cases (θ=30° and ϕ=0°, θ=45° and ϕ=0°), the behavior is analogous with effective area values in a range between those of the on-axis direction and those obtained along the CubeSat diagonal. Therefore, the results of this third group of simulations are consistent with the expected effective area trend.

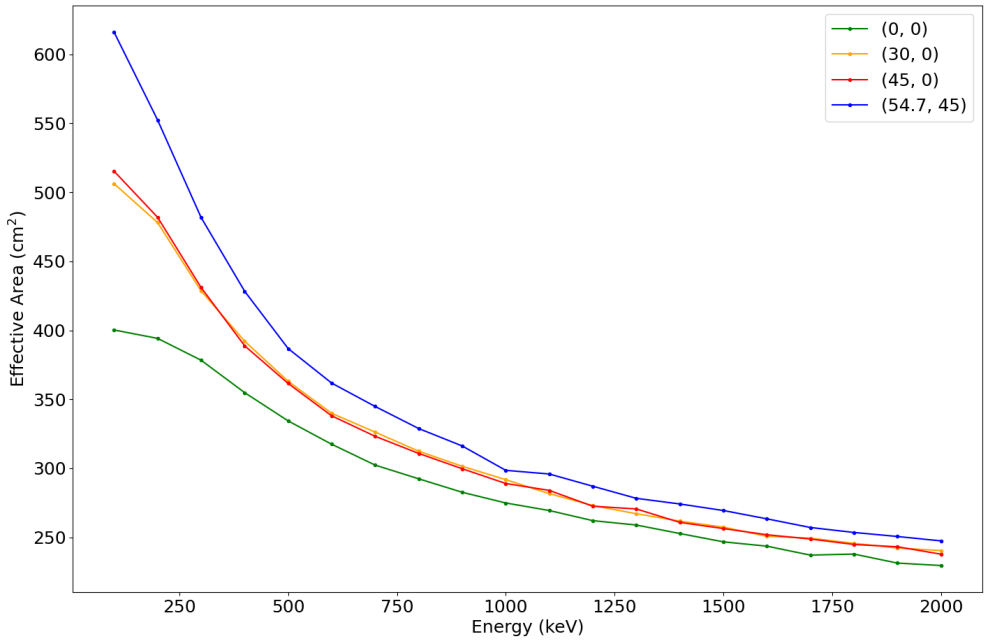

Figure 4.7: Outcomes of the third group of effective area simulations. The general effective area behavior is the same for each curve: higher effective area values at lower energies and lower ones at higher energies, as explained in Subsec. 4.3.1. Moreover, the effective area has the higher values when is off-axis rather than on-axis, since a larger portion of the CubeSat is illuminated.

4.4 Localization capability investigation

After completing the simulations related to the effective area investigation, the focus was shifted to the study of the CubeSat localization capabilities. The idea was to build a single geometry and create different source files with several directions (θ and ϕ) and run a simulation for each one of them. At this stage, for each direction a reference vector can be created with the number of hits per voxel obtained from simulations, thus generating a look-up-table. When considering an event with an unknown direction, its hits per voxel can be compared with the reference table to estimate its direction. Considering this procedure just outlined, which is further described below, different simulations were performed.

Only one geometry was considered for these simulations: the configuration with 25% occupied volume and voxel side lengths fixed at 10 mm, corresponding to a total of 2000 detectors. Thus, the geometry is exactly the one described in Subsec. 4.3.3 and shown in Fig. 4.5.

Regarding the sources, their parameters were the same as the ones listed in Subsec. 4.3.1 except for two. The first difference is related to the energies, as only a single monochromatic value of 100 keV was used. The second involves the source direction, for which several θ and ϕ were selected applying a specific approach. In particular, 5000 couples of angles were generated with a Python script applying the Fibonacci sequence (ExtremeLearning.com.au 2025) and mapping 1/2 of a sphere, resulting in a homogeneous distribution of directions. Only half of the sphere was modeled, and the simulations were performed on this half, as the other half is equivalent by symmetry. Thus, 5000 source files with related different source directions were obtained. A 3D visualization of these directions distribution is shown in Fig. 4.8.

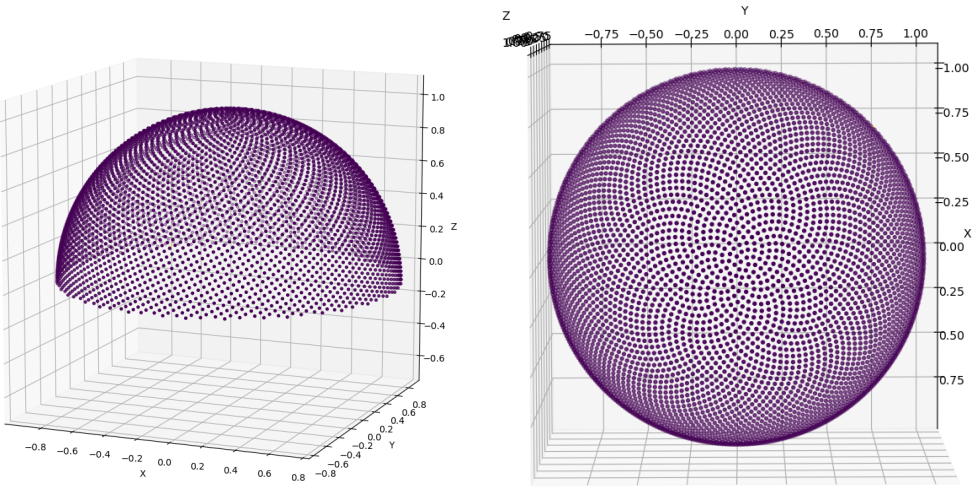

Figure 4.8: 3D visualization of 5000 source directions distribution (from two different perspectives), generated as discussed in the text.

At this stage, after describing both the geometry and the source files, the procedure used to obtain the look-up-table for the source directions is illustrated. Specifically, for each simulation corresponding to a given direction, the associated sim-file was analyzed. This analysis was performed using a Python script that extracts the number of hits per voxel for each simulation, and therefore for each direction. These results were then compiled into a look-up table consisting of a 5000-line text file, where each line represents a specific direction and contains the hit counts for each of the 2000 voxels.

After having generated the reference table, two distinct source directions were chosen and simulated. In particular, these directions were: (θ=12.5°, ϕ=67.3°) and (θ=41.7°, ϕ=51.3°) and a sketch representing the direction of the beam hitting the CubeSat is shown in Fig. 4.9 and Fig. 4.10, respectively. These two directions are referred to as unknown sources since the aim is to estimate them as if they were not known.

The text files related to these unknown sources contained the vector with the number of hits for each voxel related to that specific direction, in order to have the same structure of the reference table. Each of these files was compared with the look-up-table in order to obtain the direction that best approximates the unknown one. For every source direction contained in the look-up-table, the hits per voxel from the reference table file ($\text{Counts}_{\text{known}}[voxel_i]$) and those from the unknown source file ($\text{Counts}_{\text{unknown}}[voxel_i]$) were combined in three different ways. The first method used the standard χ^2 formula. The second employed the Minkowski distance (Şuhubi 2003), defined by the following formula:

$$\left(\sum_{i=1}^{VoxelsNumber} (\text{Counts}_{\text{known}}[voxel_i] - \text{Counts}_{\text{unknown}}[voxel_i])^p \right)^{1/p} \tag{4.2}$$

where p was considered to be 4 and 6 in two different cases. Thus, after applying the χ^2 and Eq. 4.2 formulas, each direction (i.e. pair of angles) was associated with a numerical value given by the corresponding formula. The script then evaluated all these values and identified, for each case, the minimum one, which corresponds to the best approximation of the unknown source direction. Tables reporting the estimated directions obtained with the procedure just explained for χ^2, p=4 and p=6 formulas and plots showing the 3D distribution of values obtained for each of the three formulas, are shown in Fig. 4.9 for (θ=12.5°, ϕ=67.3°) and in Fig. 4.10 for (θ=41.7°, ϕ=51.3°) and in Tab. 4.1. These tables and plots show, for both directions, that the best estimate of the unknown direction is the one obtained with p=4 and p=6 formulas: this is an expected result, since the Minkowski formula tends to enhance the presence of local minima around a small number of voxels, which is exactly what was tried to locate in this study.

Formula	$\boldsymbol{\theta}$	$\boldsymbol{\phi}$
χ^2	13.3°	66.0°
p=4	11.5°	70.8°
p=6	11.5°	70.8°

Formula	$\boldsymbol{\theta}$	$\boldsymbol{\phi}$
χ^2	40.9°	52.0°
p=4	42.5°	50.2°
p=6	42.5°	50.2°

Table 4.1: *Top table*: Estimated direction obtained for the unknown source (θ=12.5°, ϕ=67.3°). *Bottom table*: Estimated direction obtained for the unknown source (θ=41.7°, ϕ=51.3°). In general, they are all obtained with the minimum procedure explained in the text for χ^2, p=4 and p=6 formulas.

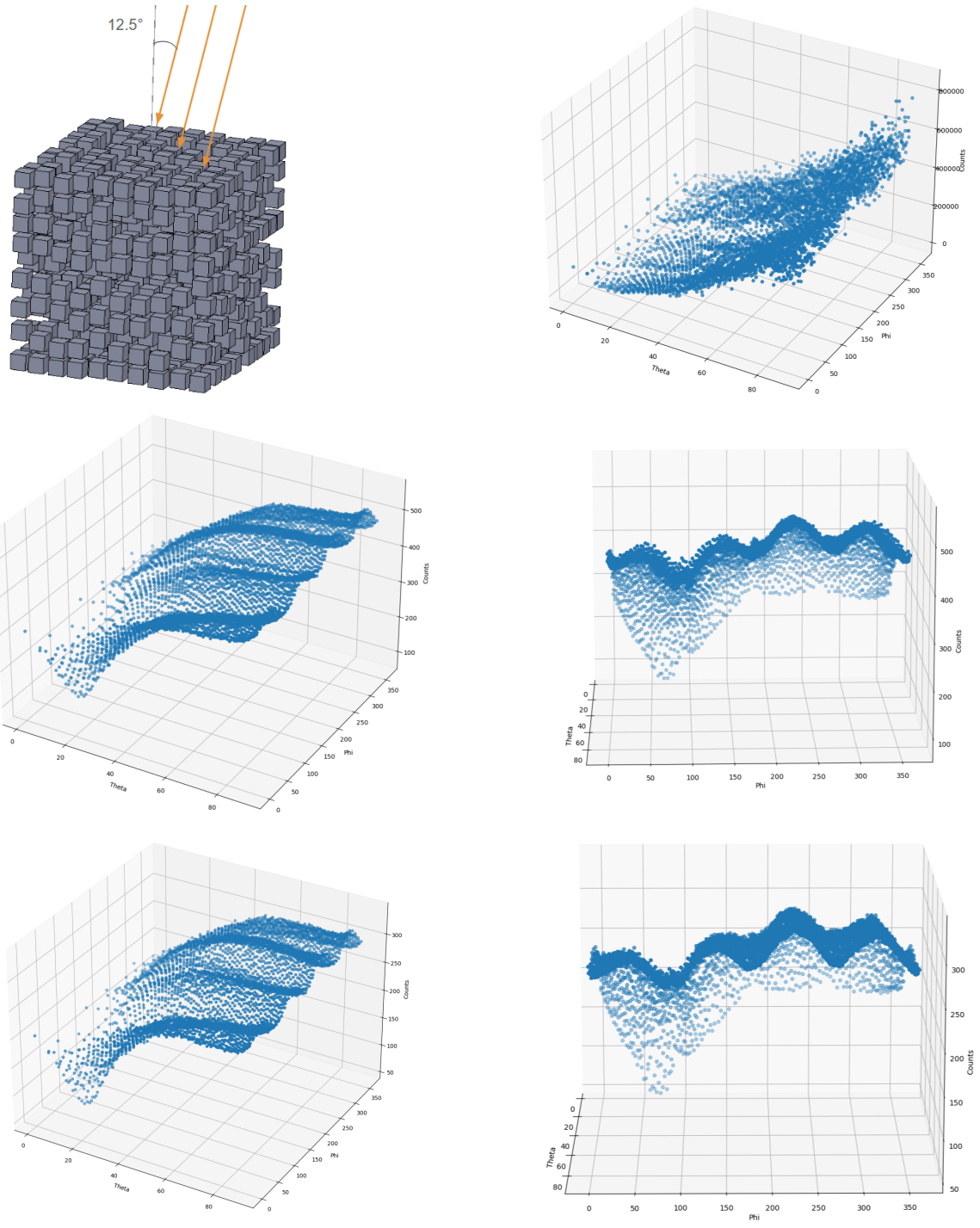

Figure 4.9: *From top to bottom*: A sketch showing θ=12.5° ϕ=67.3° beam hitting the CubeSat and 3D distributions obtained for the different pairs of angles using χ^2, p=4 (two viewing perspectives) and p=6 (two viewing perspectives) formulas. It can be observed that for p=4 and p=6 plots, the unknown source direction (θ=12.5°, ϕ=67.3°) is better identified.

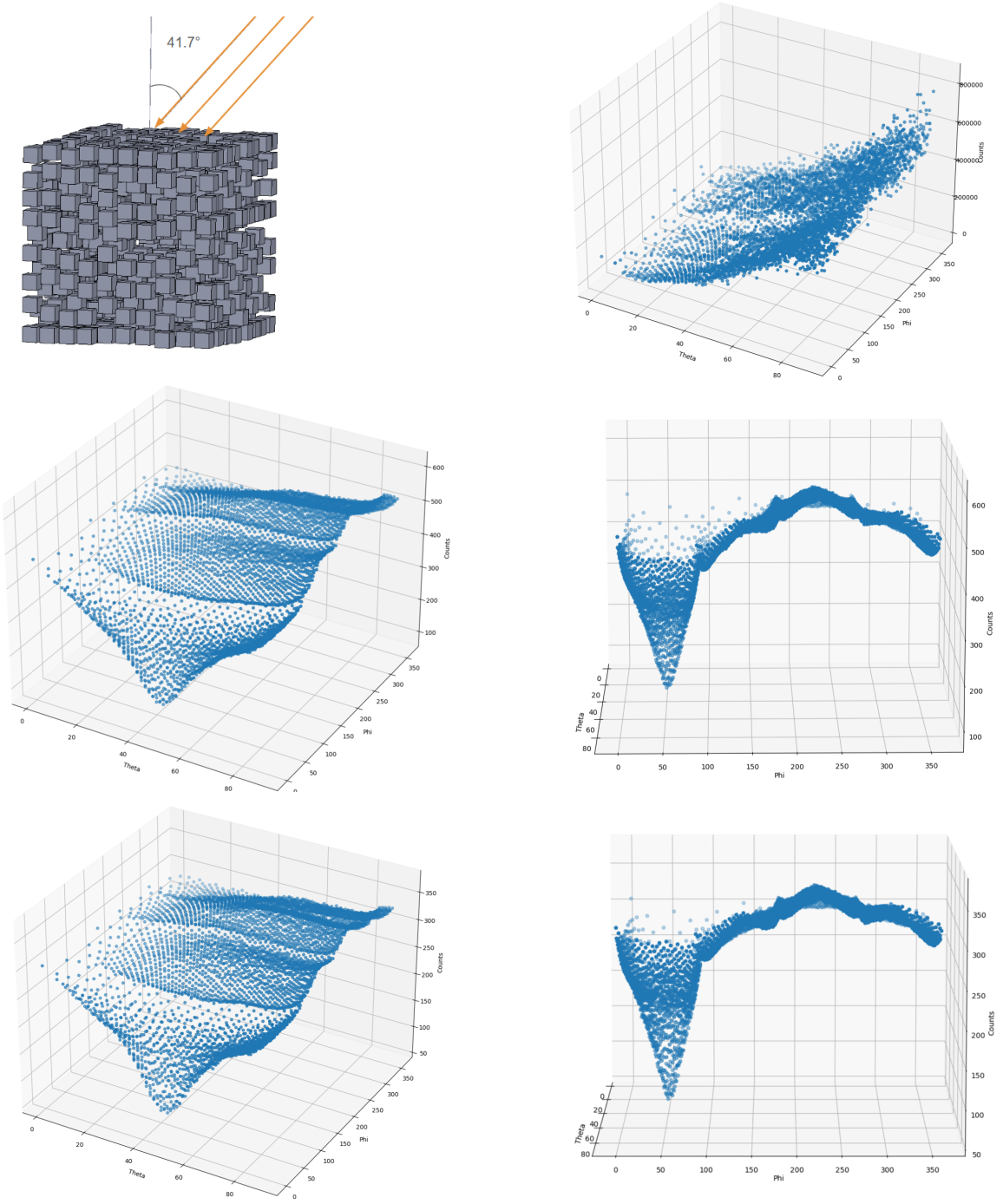

Figure 4.10: *From top to bottom*: A sketch showing θ=41.7° ϕ=51.3° beam hitting the CubeSat and 3D distributions obtained for the different pairs of angles for χ^2, p=4 (two viewing perspectives) and p=6 (two viewing perspectives) formulas. It can be observed that for p=4 and p=6 plots, the unknown source direction (θ=41.7°, ϕ=51.3°) is better identified.

Afterward, the analysis was focused on one of the two directions (θ=41.7°, ϕ=51.3°) for further studies. From Fig. 4.10, it can be observed that within the hemisphere analyzed, four distinct regions can be identified: ϕ=0°–90°, ϕ=90°–180°, ϕ=180°–270° and ϕ=270°–360° (θ is always between 0° and 90°). The evaluated direction is in the first of these four regions, so it was decided to filter the data considering only the θ=0°–90° ϕ=0°–90° region to better visualize the estimation of the unknown direction. The related plots obtained are shown in Fig. 4.11 for χ^2, p=4 and p=6 formulas. These plots provide a clearer visualization of the observations in Fig. 4.10: p=4 and p=6 formulas provide a better estimation of the unknown source direction.

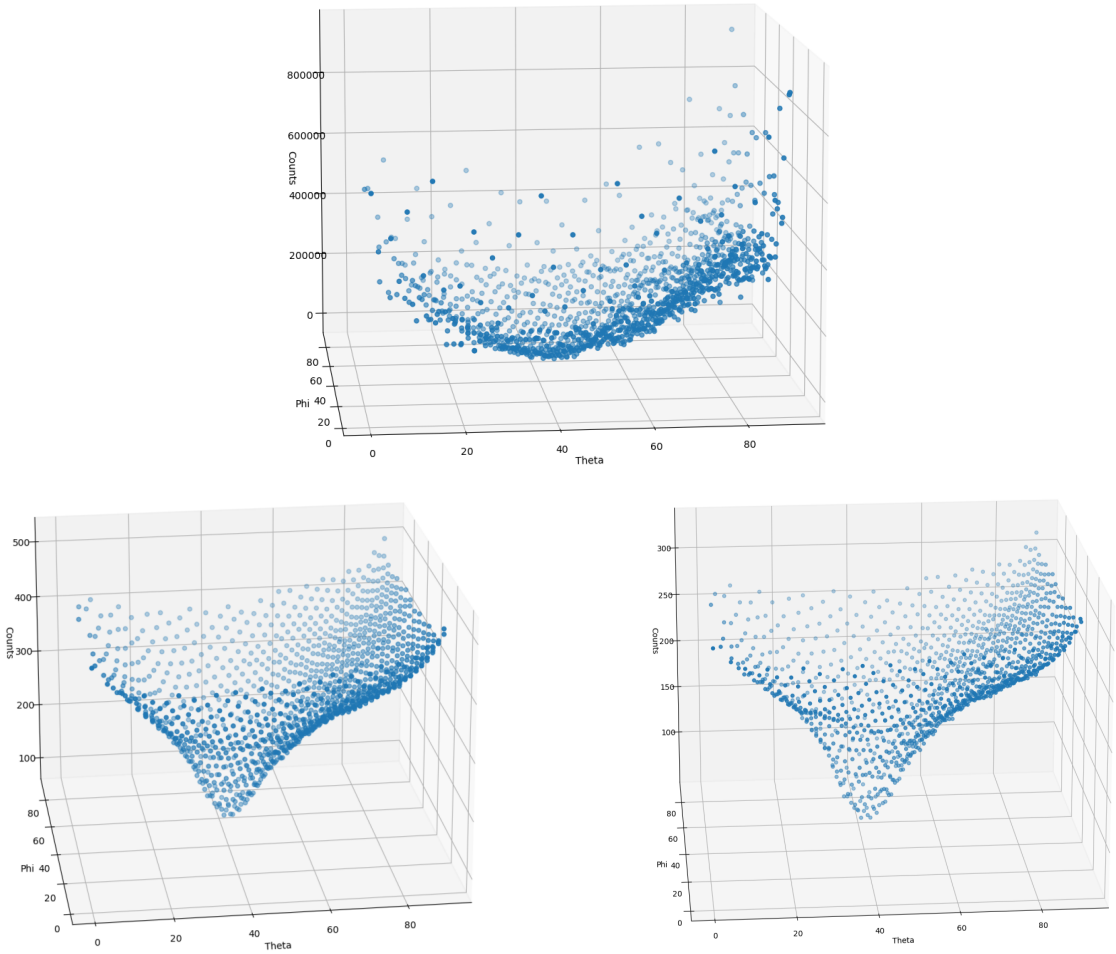

Figure 4.11: *From top to bottom*: Selection of data associated to *theta*=0°–90° ϕ=0°–90° region for (θ=41.7°, ϕ=51.3°) direction. The results are the ones previously obtained for χ^2, p=4 and p=6 formulas shown in Fig. 4.10.

Ultimately, it was decided to select a certain number of voxels from the text files of the look-up-table and of the unknown source direction (θ=41.7°, ϕ=51.3°) to check how the direction estimation changes by reducing the number of detectors and to study the localization capability. Different cases were considered by selecting the first 10, 50, 100, 500, 1000 and 2000 voxels from the text files, and only the p=6 formula was applied since it leads to a better direction estimation. For each of the six cases, the angular distance between the unknown direction and the evaluated one was calculated as well as the angular resolution. In particular, the angular distance, which can be considered as the uncertainty on the estimated direction, was calculated as

$$Angular\ Distance = ((\theta_{unknown} - \theta_{estimated})^2 \ + \ (\phi_{unknown} - \phi_{estimated})^2)^{1/2} \quad (4.3)$$

where ($\theta_{unknown}$, $\phi_{unknown}$) is the unknown source direction and ($\theta_{estimated}$, $\phi_{estimated}$) the estimated one. Regarding the angular resolution, it was estimated with the following procedure. First, taking into account that the unknown source direction is in θ=0°–90° ϕ=0°–90° region, the other three regions of the hemisphere mentioned previously were considered as background. The data in these three regions were then filtered, and the arithmetic mean of the related counts was performed to obtain an average of the background counts. At this stage, the minimum counts (associated to the evaluated chosen direction) and the background counts were used to determine the half-height level between these two values. More precisely, a range of count values around the half-height level was identified, defined as the half-height value ± 10 counts. All directions whose counts fell within this range were considered, and the angular distances between their corresponding angle pairs and the estimated direction were computed using Eq. 4.3.The average of these angular distances was taken as the angular resolution. The tables with the estimated directions, the angular distances and the angular resolutions for the different cases (10, 50, 100, 500, 1000 and 2000 voxels with p=6 formula) are shown in Tab. 4.2. The results are represented for visualization purposes in Fig. 4.12, only for the cases with 50, 500 and 2000. They show that the best source direction estimation is the one obtained in the case with 500 voxels. The procedure to obtain these results did not consider different new simulations with the reported number of voxels, but used the sim-file of one simulation selecting the first number of voxels from it, as previously stated. Therefore, these results should be verified by performing various distinct simulations.

Voxels Number	**Estimated Direction**	**Angular Distance**	**Angular Resolution**
2000	θ=42.5° ϕ=50.2°	1.4°	25.9°
1000	θ=42.5° ϕ=50.2°	1.4°	26.6°
500	θ=40.9° ϕ=52.0°	1.1°	25.4°
100	θ=42.5° ϕ=50.2°	1.4°	26.7°
50	θ=43.4° ϕ=53.1°	2.5°	27.0°
10	θ=37.7° ϕ=55.6°	5.9°	45.5°

Table 4.2: Estimated directions, angular distances (uncertainty for estimated direction) and angular resolutions for the unknown direction defined by θ=41.7°, ϕ=51.3° with 10, 50, 100, 500, 1000 and 2000 voxels, obtained with p=6 formula. In the case with 500 voxels, considering the estimated direction and the related uncertainty (angular distance), the best estimation of the unknown source direction is obtained.

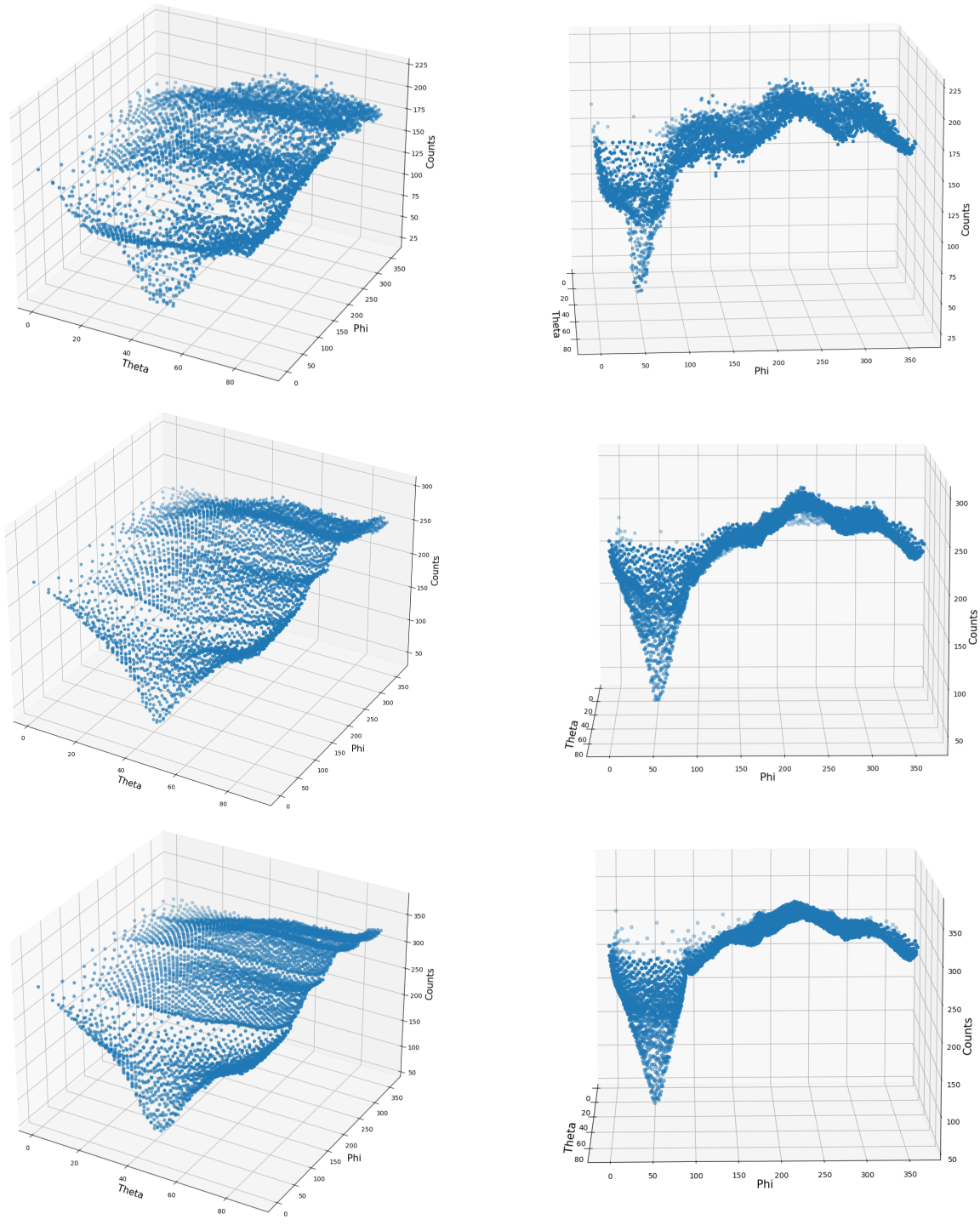

Figure 4.12: *From top to bottom*: 3D distributions obtained for the different pairs of angles for (θ=41.7°, ϕ=51.3°) unknown direction for 50, 500 and 2000 voxels, obtained with p=6 formula. It is possible to visualize what was shown by the values reported in Tab. 4.2: the case with 500 voxels is the one for which the best results are obtained.

4.5 Future prospects

All the activities previously described in Sec. 4.3 and Sec. 4.4 were aimed at investigating some of the main characteristics of the 8U CubeSat. In particular, tests performed through simulations enabled the study of some aspects associated to detector effective area and localization capability, but only under specific conditions. In this first analysis, several aspects were not included and can be taken into account for future work to further investigate the properties of this system. Some of these characteristics are reported in the following. In particular, the geometry optimization is addressed in Subsec. 4.5.1. The investigation of different scintillator materials is presented in Subsec. 4.5.2. The possibility to consider realistic GRB and TGF spectra and improve the statistics are assessed in Subsec. 4.5.3 and Subsec. 4.5.4, respectively. Ultimately, a full-sky localization mapping is considered in Subsec. 4.5.5.

4.5.1 Geometry optimization and voxels distribution

In this work, the geometry of the CubeSat consisted of a certain number of voxels with a chosen dimension, and they were randomly selected inside the CubeSat, considering the procedure described in Subsec. 4.3.1. However, an optimized geometry can be considered and studied in a future work, since it can improve the angular resolution of the system. In particular, a more regular non-random and symmetric geometry can be considered for future developments.

4.5.2 Investigation of different scintillator materials

The current simulations modeled each detector inside the CubeSat as a CsI scintillation crystal only. Nevertheless, it can be important to consider also the effects of SiPM for each crystal in order to make simulations more realistic and evaluate their impact on the system. Different type of scintillators, such as $LaBr_3$, $CeBr_3$, or NaI(Tl), can be considered with their related distinct properties (light yield, decay time, energy resolution). Moreover, a mechanical structure to support the voxels in the CubeSat can be considered to make the system even more realistic. Such a supporting structure would be transparent at high energies, while it would absorb part of the radiation at low energies.

4.5.3 Localization capability using realistic GRB and TGF spectra

The sources chosen in this work for the effective area simulations ranged between 100 keV and 2 MeV, but higher energies can be examined for further investigations. In particular, GRBs and TGFs typical spectra can be simulated to examine the angular

reconstruction considering more realistic photon energy distribution. For the localization capability study, only a fixed 100 keV monochromatic source was used for the simulations. Thus, expanding the energies values studied to higher ones can be a goal for future studies.

4.5.4 Improved statistics

The number of photons considered for each simulations performed in this work was 10^5. This led to a number of hits per voxel that was $\sim$100 even for the voxels that were most affected by events, so the statistics per voxel was limited. Therefore, generating a larger number of events per simulation can be taken into account to improve the statistics per voxel and obtain better localization performances in a follow-up analysis.

4.5.5 Full-sky localization mapping

A pair of specific directions were considered in the simulations for the study of the localization capability, but several other tests can be performed to study the properties of this system. In particular, multiple chosen source directions can be generated and a large number of simulations can be performed for each one. Thus, the error in the estimation of the chosen direction for each simulation can be evaluated. Several estimates for each chosen source direction can be obtained in such a way, so the related angular distances between the estimated value and the chosen direction can be calculated. Therefore, each direction presents a distribution of angular distances, obtaining in this way a localization capability that depends on each (θ, ϕ) direction. However, also other formulas and procedures can be applied to study the system in further details in the future.

Conclusions

This Thesis addressed the study of high-energy transient phenomena from atmospheric events such as TGFs and gamma-ray glows to astrophysical transients such as GRBs through an integrated ground-to-space strategy. Two complementary approaches were followed: the development and operation of dedicated ground-based detectors, and the design and preliminary simulation of a wide-field gamma-ray instrument onboard an 8U CubeSat.

From the ground-based perspective, the Gamma-Flash (Mt. Cimone, Sestola - Modena) and PIZ-Gamma (Mt. Piz Boè, Canazei - Trento) detectors were built, optimized, and operated to detect real atmospheric events. Their characterization included the study of acquisition parameters, trigger algorithms, environmental monitoring, and the creation of a dedicated data-analysis pipeline capable of producing light curves, spectra, and event classification. The first observational results obtained from these instruments confirmed their capability to detect atmospheric gamma-ray transients in real conditions: one glow observed at Mt. Cimone and three glows recently detected at Mt. Piz Boè. The comparison between the two sites highlights the strong dependence of detection efficiency on altitude, atmospheric extinction, and field-of-view constraints.

The second part of the Thesis extended the ground-based experience towards space by proposing an instrument concept for an 8U CubeSat equipped with a 4π CsI-based gamma-ray detector. The CubeSat geometry, detection volume, and effective area were modeled through Monte Carlo simulations performed with MEGAlib. First-order studies of effective area and source localization demonstrated that even a compact instrument can achieve significant sensitivity to gamma-ray events, enabling joint observations of TGFs and GRBs from orbit.

The work carried out in this second part of the Thesis represents only a first exploration of the performance of a 8U Cubesat based on a randomly distributed voxels geometry, which has a very high potential in terms of effective area and transient localization capability. Several important aspects remain open for future investigation. In particular, the following points should be addressed to better characterize and optimize the instrument.

- In this Thesis, the detectors (voxels) were randomly placed within the CubeSat volume, following the procedure described in Sec.4.3.1. Future developments should explore non-random, optimized distributions of voxels to improve the localization accuracy.

- Current simulations model each detector as a CsI scintillation crystal only, excluding other components such as SiPMs. A natural next step is to evaluate the impact of different scintillator materials (e.g., $LaBr_3$, $CeBr_3$, or NaI(Tl)) and to assess how their distinct properties influence the effective area, timing accuracy, and localization capability. The inclusion of SiPM contributions and also of a mechanical structure to support the randomly distributed voxels can make the overall system more realistic.

- Current localization study used only a monochromatic 100 keV source, providing a simplified, first-order evaluation. A more realistic assessment should simulate typical GRBs and TGFs spectra.

- Simulations in this work used a fixed number of 10^5 photons, resulting in limited statistics per voxel ($\sim$ 100 counts in the most illuminated pixels, depending on the direction of incidence of the photons). Increasing the number of simulated photons would reduce statistical uncertainties and yield more robust localization performance maps across the full sky.

- A complete localization-capability map can also be achieved generating large sets of simulations for several incident directions. For each direction, the distribution of the reconstructed angles can be used to build a full-sky localization capability map.

Overall, the results obtained in this Thesis demonstrate the feasibility and scientific value of an integrated ground-to-space approach to high-energy transient phenomena. Ground-based detectors proves to be effective in the detection of atmospheric gamma-ray events, while the CubeSat concept shows strong potential for future space-borne observations of both TGFs and GRBs. With the implementation of the future developments outlined above, particularly the optimization of detector geometry, the study of alternative scintillator materials, and the characterization of localization capabilities using realistic spectra, the proposed 8U CubeSat could be used as a powerful and promising tool for high-energy transient astrophysics.

Bibliography

Dwyer, J. R. et al. (2012). "High-Energy Atmospheric Physics: Terrestrial Gamma-Ray Flashes and Related Phenomena". In: *Space Science Review* 173, pp. 133–196.

Wilson, C. T. R. (1925). "The Acceleration of β-Particles in Strong Electric Fields such as those of Thunderclouds". In: *Mathematical Proceedings of the Cambridge Philosophical Society* 22.4, pp. 534–538.

Dwyer, J. R. (2003). "A Fundamental Limit on Electric Fields in Air". In: *Geophysical Research Letters* 30.20, p. 2055.

Dwyer, J. R. et al. (2008). "High-energy electron beams launched into space by thunderstorms". In: *Geophysical Research Letters* 35, p. L02815.

NASA/Goddard Space Flight Center and J. Dwyer and Florida Institute of Technology (2011). *Animation of Terrestrial Gamma-Ray Flash.* URL: `https://svs.gsfc.nasa.gov/10706` (visited on 08/01/2025).

Rutjes, C. et al. (2017). "TGF Afterglows: A New Radiation Mechanism From Thunderstorms". In: *Geophysical Research Letters* 44, pp. 10702–10712.

Enoto, T. et al. (2017). "Photonuclear reactions triggered by lightning discharge". In: *Nature* 551, pp. 481–484.

Fishman, G. J. et al. (1994). "Discovery of Intense Gammsa-Ray Flashes of Atmospheric Origin". In: *Science* 264, pp. 1313–1316.

Inan, U. S. et al. (1996). "On the association of terrestrial gamma-ray bursts with lightning and implications for sprites". In: *Geophysical Research Letters* 23, pp. 1017–1020.

Dwyer, J. R. et al. (2004). "Measurements of X-ray Emission from Rocket-Triggered Lightning". In: *Geophysical Research Letters* 31, p. L05118.

Smith, D. M. et al. (2011). "A terrestrial gamma ray flash observed from an aircraft". In: *Journal of Geophysical Research: Atmospheres* 116, p. D20124.

Neubert, T. et al. (2009). "ASIM – an Instrument Suite for the International Space Station". In: *AIP Conference Proceedings* 1118, pp. 8–12.

— (2020). "A terrestrial gamma-ray flash and ionospheric ultraviolet emissions powered by lightning". In: *Science* 367, pp. 183–186.

Wada, Y. et al. (2019). "Gamma-ray glow preceding downward terrestrial gamma-ray flash". In: *Communications Physics* 2, p. 67.

Hisadomi, S. et al. (2021). "Multiple Gamma-Ray Glows and a Downward TGF Observed From Nearby Thunderclouds". In: *Journal of Geophysical Research: Atmospheres* 126, e2021JD034543.

Tsuchiya, H. et al. (2011). "Long-duration gamma-ray emissions from 2007 and 2008 winter thunderstorms". In: *Journal of Geophysical Research: Atmospheres* 116, p. D09113.

Rakov, V. A. and Uman, M. A. (2003). *Lightning - Physics and Effects*. Cambridge University Press.

Pasko, V. P. (2003). "Electric jets". In: *Nature* 423, pp. 927–928.

Bambi, C. and Santangelo, A. (2024). *Handbook of X-ray and Gamma-ray Astrophysics*. Springer Nature Singapore.

D'Avanzo Paolo (INAF-OAB) (n.d.). *GRBs @ SOXS*. URL: https://indico.ict.inaf.it/event/2869/contributions/17991/attachments/8423/17371/D%27avanzo%20SOXSWG11_napoli_2024_pdavanzo.pdf.

Pe'er, A. (2015). "Physics of Gamma-Ray Bursts Prompt Emission". In: *Advances in Astronomy* 2015, Article ID 907321.

Zhang, B. et al. (2006). "Physical Processes Shaping Gamma-Ray Burst X-Ray Afterglow Light Curves: Theoretical Implications from the Swift X-Ray Telescope Observations". In: *The Astrophysical Journal* 642, pp. 354–370.

Klebesadel, R. W. et al. (1973). "Observations of Gamma-Ray Bursts of Cosmic Origin". In: *The Astrophysical Journal* 182, pp. L85–L88.

Kouveliotou, C. et al. (1993). "Identification of Two Classes of Gamma-Ray Bursts". In: *The Astrophysical Journal* 413, pp. L101–L104.

Metzger, M. R. et al. (1997). "Spectral constraints on the redshift of the optical counterpart to the γ-ray burst of 8 May 1997". In: *Nature* 387, pp. 878–880.

Eichler, D. et al. (1989). "Nucleosynthesis, neutrino bursts and γ-rays from coalescing neutron stars". In: *Nature* 340, pp. 126–128.

Woosley, S. E. et al. (1993). "Gamma-ray bursts from stellar mass accretion disks around black holes". In: *The Astrophysical Journal* 405, pp. 273–277.

Gehrels, Neil and the Swift Team (2005). "The Swift Gamma-Ray Burst Mission: First Results". In: *AIP Conference Proceedings: Coupling of Thunderstorms and Lightning Discharges to Near-Earth Space*.

Ursi, A. et al. (2022). "A Study on TGF Detectability at 2165 m Altitude: Estimates for the Mountain-Based Gamma-Flash Experiment". In: *Remote Sensing* 14, p. 3103.

Campana, Riccardo (2025). *Astronomical Instrumentation - High Energy Detectors*. Lecture notes, Alma Mater Studiorum Università di Bologna.

Calabretto, P. et al. (2025). "The Gamma-Flash Program: high-energy radiation and particles in thunderstorms, lightning, and terrestrial gamma-ray flashes". In: *Journal of Physics: Conference Series* 2985, p. 012015.

Saleh-Natur, J. et al. (2024). "SPIE Proceedings: GALI- A GAmma-ray burst Localizing Instrument: Results from Full Size Engineering Model". In: 13093.

Zoglauer A. (2020). *Geomega - Geometry for MEGAlib*.

— (2021). *Cosima - A Cosmic Simulator for MEGAlib based on Geant4*.

ExtremeLearning.com.au (2025). *How to evenly distribute points on a sphere – more effectively than the canonical Fibonacci lattice*. URL: https://extremelearning.com.au/how-to-evenly-distribute-points-on-a-sphere-more-effectively-than-the-canonical-fibonacci-lattice/ (visited on 11/27/2025).

Şuhubi, E. S. (2003). "Metric Spaces". In: *Functional Analysis*. Springer, pp. 261–356.